이학박사 학위논문

Development of Novel Super-resolution Nanoscopy and Spectroscopy Techniques by Using the Photophysical Characteristics of Fluorescent Dyes

형광 염료의 광물리적 특성을 이용한 새로운 초고분해능 현미경법 및 분광학법의 개발

2015 년 8 월

서울대학교 대학원
생물물리 및 화학생물학과 생물물리 및 화학생물학 전공
권 지 웅

Ph.D. Dissertation

Development of Novel Super-resolution Nanoscopy and Spectroscopy Techniques by Using the Photophysical Characteristics of Fluorescent Dyes

Jiwoong Kwon

Research Advisor **: Professor Seong Keun Kim**

Department of Biophysics and Chemical Biology

Seoul National University

Abstract

Development of Novel Super-resolution Nanoscopy and Spectroscopy Techniques by Using the Photophysical Characteristics of Fluorescent Dyes

Jiwoong Kwon
Major in Biophysics and Chemical Biology
Department of Biophysics and Chemical Biology
The Graduate School
Seoul National University

Fluorescence is a wonderful tool for investigation of the biomolecular structure and interactions as well as many of its non-biological applications, due to the noninvasive nature of light. Especially, the fluorescence microscope provides the ability to image the interior of living cells with molecular specificity. However, there exist a fatal disadvantage on the conventional fluorescence techniques called diffraction limit that restrict the spatial resolution of optical microscope to roughly half of wavelength (~250 nm for visible light), which is much larger than the size of biomolecules. Even in the diffusion-based single molecule spectroscopy, which can observe and analyze the individual molecules in ambient conditions to avoid the ensemble average, the diffraction limit harshly restricts the concentration of fluorescent molecules lower than 100 pM, where the biomolecular concentration in a living cell is usually much higher.

In order to overcome the diffraction limit, super-resolution techniques have been developed in recent 20 years, mainly focused on the microscope. Although their specific strategies are slightly different from each other, the super-resolution techniques share an identical core mechanism, the switching between on and off

states of target fluorophores. Nowadays, the super-resolution nanoscopy can image the three-dimensional structure of multiple components in living cells with < 20 nm spatial resolution, sometimes even with video-rate temporal resolution. However, the complex and expensive technical features hinder the common uses of super-resolution nanoscopy in wide range of applications. Hence we tried to improve and develop the super-resolution nanoscopy and spectroscopy techniques by utilizing the photophysics of fluorescent molecules.

Reversible saturable optical fluorescence transition (RESOLFT) nanoscopy is a powerful method for super-resolution imaging of living cells with low light intensity. But the useful applications of RESOLFT nanoscopy is only performed with the fluorescent proteins, whose photobleaching resistance against the photoswitching cycles are much better than the organic fluorophores. We demonstrated for the first time the implementation of RESOLFT nanoscopy for a biological system using organic fluorophores by precisely optimizing the imaging buffer and optical parameters to overcome the photobleaching problem. Using a covalently linked dye pair of Cy3 and Alexa647 labeled microtubules in a fixed HeLa cell, we achieved a spatial resolution of ~100 nm in the focal plane. This method provides a powerful alternative for biocompatible super-resolution imaging and also may open doors to optical writing and read-out with organic fluorophores.

We also introduced a new, easily implementable sub-diffraction limit microscopy technique utilizing the optical AND-gate property of fluorescent nanodiamond (FND). We demonstrate that when FND is illuminated by two spatially-offset lights of different wavelengths, emission comes only from the region of their overlap, which is used to reduce the effective point spread function form ~300 nm to ~130 nm in lateral plane, well below the diffraction limit. With this technique, sub-diffraction limit microscopy can be implemented in a quick, easy, convenient, and inexpensive way with no technical complexities often encountered in other methods. Furthermore, since FND is an ideal fluorescent

material with high photostability, this new method may find its use in dynamic imaging over a long duration of time.

To overcome the concentration limit in diffusion-based single molecule techniques, we tried to combine the stimulated emission depletion (STED) nanoscopy with them, especially the alternating laser excitation (ALEX) spectroscopy utilizing the fluorescence resonance energy transfer (FRET). By spatially overlapping additional doughnut-shaped depletion beam with a focused light, we successfully reduced the effective observation volume in ALEX-FRET measurement, resulted to the observation of the individual molecules in higher concentration. We demonstrated the feasibility of this new technique, named ALFRED, by using a dual labeled single stranded DNA, and observed the single diffusion DNA molecules at up to 5 nM concentration, which is 100 times higher than that of typical single molecule measurement. Since a number of biomolecules have the dissociation constant in nanomolar concentration range, the ALFRED can offer the novel way for the single molecule spectroscopy in living cells.

Keywords : Fluorescence / Photophysics / Fluorophore / Diffraction Limit / Super-resolution Nanoscopy / Single Molecule Spectroscopy
Student Number : 2009 – 23842

Contents

Chapter 1.

Fluorescence, Fluorophore, Photophysics and Related Techniques

1.1. Introduction

Fluorescence is one of the fundamental processes of molecules, which emits electromagnetic wave during the relaxation of a light-driven excited electron – thus the fluorescence is a form of luminescence. It enables to distinguish a target molecule in interest from the complex mixture of diverse substances. Because of the great sensitivity and specificity, the fluorescence has become a versatile tool in the fields of chemical, physical, biological, and medical sciences.

Although the first observation of the fluorescence was reported in 1500s, its drastic growth was begun from 1960s when a coherent light source – laser – was developed. In the late 1900s, introduction of extremely sensitive photodetectors such as photomultiplier tube (PMT), avalanche photodiode (APD) and electron multiplying charge-coupled device (EMCCD) has been further advanced the fluorescence. As a result, recently developed fluorescence techniques are able to detect and analyze the interesting subjects with single molecule sensitivity.

In biological science, the fluorescence plays much more crucial rules due to the non-invasive nature of light. Among the huge amount of analytic tools, optical microscope is one of the most effective methods for the monitoring of the inside of living samples. Thus the fluorescence microscope, a branch of the optical microscope, has a great advantage to image the interior of living cells with molecular specificity. Although the conventional optical microscope has a

resolution limit due to the diffraction of light, recently developed 'super-resolution nanoscopy' techniques provide nanometric spatial resolution for the biomolecular imaging.

Recent fluorescence techniques, which are mentioned above, including single molecule spectroscopy and super-resolution nanoscopy, are highly implemented in technology and are extending their field of applications. Nonetheless, even the most-recently developed techniques, they still have some weaknesses disturbing their extensive applications to the biological, medical and pharmaceutical sciences. Further improvements, both in terms of technology and methodology, are still required to offer new possibilities and extending the practical applicability of these techniques. This thesis is mainly focused on the works that contributes to such everlasting efforts. In this chapter, we will briefly overview about the fluorescence, fluorophore, photophysics and related techniques such as optical microscopy and spectroscopy, mainly focusing on features relevant for the following chapters.

1.2. Fluorescence

In terms of the emission of visible photons by excited species, fluorescence is a particular case of luminescence. Luminescence can be categorized in several different types by the mode of excitation: photoluminescence, radioluminescence, cathodoluminescence, electroluminescence, chemiluminescence, bioluminescence, sonoluminescence and so on (Fig. 1.1).[1] Fluorescence is belonged to the photoluminescence with phosphorescence, which is one of the possible physical effects resulting from interaction of light with matter, since an electron has to be excited by incident light for the fluorescence. However, contrary to phosphorescence, the electron transits from first singlet excited state (S_1) to singlet ground state (S_0) without any change in spin quantum number.

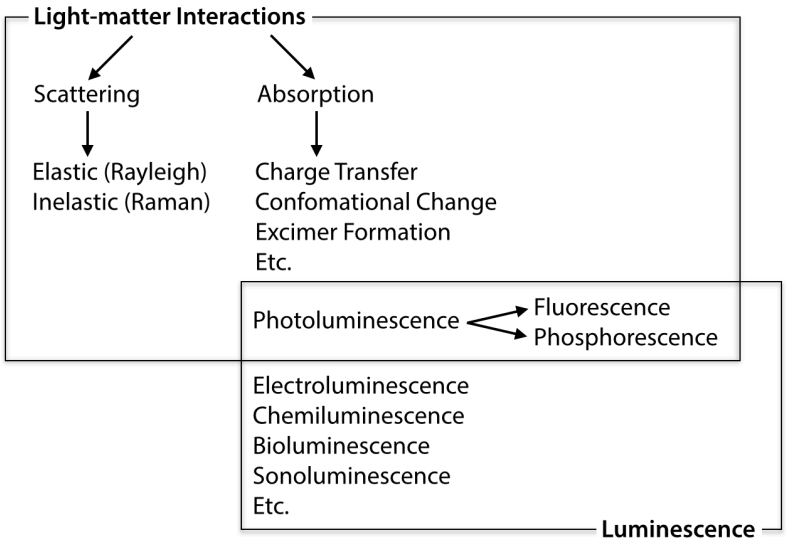

Fig. 1.1 The position of fluorescence in the categorized 'light-matter interactions' and 'luminescence'. Fluorescence is a part of photoluminescence, a radiative relaxation process of an excited electron by light absorption.

1.2.1. A Brief History of Fluorescence

The first observation of fluorescence is reported by the Spanish physician Nicolas Monardes in 1565.[2] He found an eccentric blue color of an infusion of a wood called *Lignum Nephriticum*. After ~300 years, in 1833, a Scottish preacher reported a red color of an alcoholic extract of leaves (chlorophyll) under white light illumination, and pointed out the similarity with the case of the fluorspar crystals.

The term "fluorescence" was introduced by Sir George Gabriel Stokes, a physicist and professor of mathematics at Cambridge in the mid-1800s. In 1853, he invented the term fluorescence from the name of the fluorspar, which was known to emit light under ultraviolet (UV) light irradiation. Before he established the concept of fluorescence, in 1852, he reported an emission of light by calcium sulfide upon excitation in the UV.[3] He found that the calcium sulfide glowed with a blue light only when it illuminated under UV portion of the solar spectrum generated by a prism. With this observation, Stokes said that the emitted light

always has longer wavelength than the excitation light, which is now known as Stokes' law.

Year	*Scientist*	*Observation or Achievement*
1905	E. L. Nichols	First fluorescence excitation spectrum of a dye
1907	E. L. Nichols	Mirror symmetry between absorption and fluorescence spectra
1918	J. Perrin	Photochemical theory of dye fluorescence
1920	F. Weigert	Discovery of the polarization of the fluorescence emitted by dye solution
1922	S. J. Vavilov	Excitation-wavelength independence of the fluorescence quantum yield
1926	E. Gaviola	First direct measurement of nanosecond lifetimes by phase fluorometry
1927	E. Gaviola	Demonstration of resonance energy transfer in solutions
1932	F. Perrin	Quantum mechanical theory of long-range energy transfer between atoms
1935	A. Jablonski	Jablonski's diagram
1944	Lewis and Kasha	Triplet state
1948	Th. Förster	Quantum Mechanical theory of dipole-dipole energy transfer

Table 1.1 Milestones in the history of fluorescence during the first half of the twentieth century.

In addition to these discoveries, further investigations to the details of fluorescence were progressed during the first half of 1900s. Some of the examples for the most important events are reported in Table 1.1.

1.2.2. Electronic States

When a molecule emits fluorescence under light illumination, it undergoes three distinct steps that occur in different timescales separated by several orders of magnitude. The first step is the excitation of the molecule, which occurs in femtoseconds (10^{-15} s), by absorption of an incident photon with suitable energy. The absorbed energy facilitates the transition of the valence electron from the highest occupied molecular orbital (HOMO) to the lowest unoccupied molecular orbital (LUMO). Because the electron has much lower mass than the nuclei (three orders of magnitude), the electronic transition time is too short for any significant movement of the nuclei. In other words, all the electronic transitions vertically

occur in the energy-coordinate diagram as described by the Franck-Condon principle (Fig. 1.2).[4,5] According to this principle, the electron in the lowest vibrational state of the S_0 state will be excited into a higher vibrational level of the S_1 state. It also can be applied to the reverse transition, the relaxation processes of the excited electron from the S_1 state to the S_0 state.

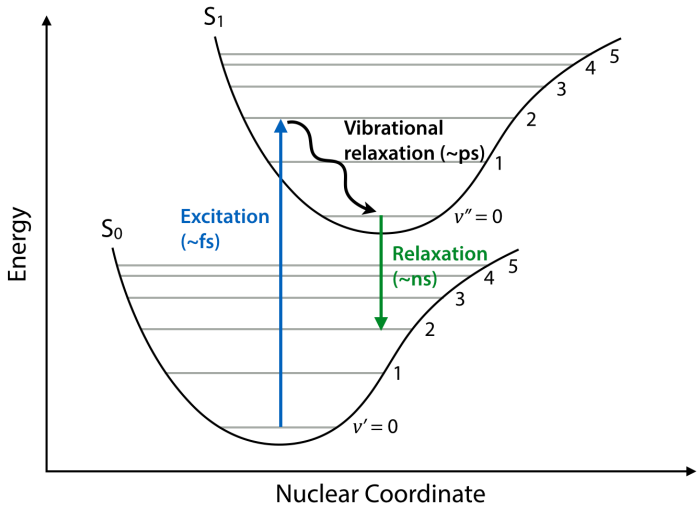

Fig. 1.2 Schematic illustration of the Franck-Condon principle and the Kasha's rule. Electronic transitions and the vibrational relaxation to the lowest vibrational state of the S_1 state are represented as the arrows with typical timescales.

After excitation, the electron undergoes a fast relaxation process to the lowest vibrational state of the S_1 state on the timescale of picosecond (10^{-12} s).[6] According to the Kasha's rule, even the electron excited into the higher excited states (S_n, n > 1) also undergoes the same relaxation process to the lowest vibrational state of the S_1 state.

Finally, the excited electron is relaxed to the S_0 state through both of radiative and non-radiative pathways in nanosecond (10^{-9} s) timescale. Fluorescence is one of the radiative relaxation pathway, thus it usually competes with other de-excitation processes if they take place on a comparable time scale.

These simple electronic states and excitation/de-excitation schemes can be demonstrated in several ways, most of which are presented on Jablonski diagram.[7]

In this diagram, the electronic states are vertically aligned by energy and grouped horizontally by spin multiplicity (i.e., singlet and triplet states). The vibrational ground states are represented with thick lines, whereas higher states have thinner lines. Figure 1.3 shows a simple Jablonski diagram for the electron states and the transition between the states.

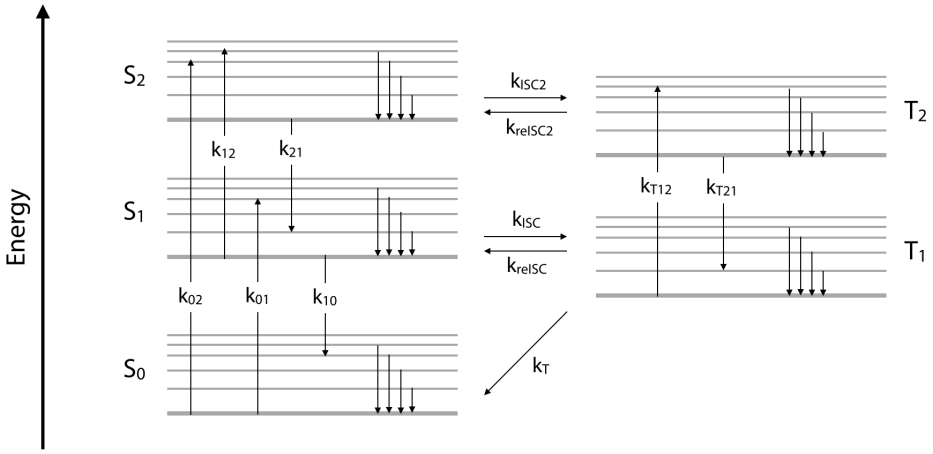

Fig. 1.3 A typical Jablonski diagram for the electron states and the transition between the states. Each transition is represented in the terms of kinetic constant. (k_{XY}; X to Y transitions; ISC: intersystem crossing; Subscribed '$_T$': triplet state; re: reverse process;)

In quantum chemistry, the lowest singlet ground state (S_0), which is the typical ground state of a fluorescent molecule, is that molecular orbital is occupied by two electrons with an opposite spin direction. The characteristic is can be quantified in terms of 'multiplicity', which is the amount of unpaired electron spun and is calculated as $2s+1$ where 's' is the number of singly occupied electrons multiplied by the electron spin projection quantum number $m_s = \pm 1/2$.[8] All of the electrons are paired in the singlet state and the multiplicity equals to 1, even when an electron is excited by light illumination. This arrangement is strictly required by the Pauli exclusion principle. The de-excitation process can be occurred in both of radiative and non-radiative pathways. The former is called 'fluorescence' accompanied by emission of a photon, and the latter is called internal conversion (IC) where the excess of energy is mainly released as heat. Adding to IC, there are

many of other non-radiative de-excitation pathways including intersystem crossing (ISC), intramolecular charge transfer, conformational change and others.[9]

1.2.3. Absorption and Emission Spectrum

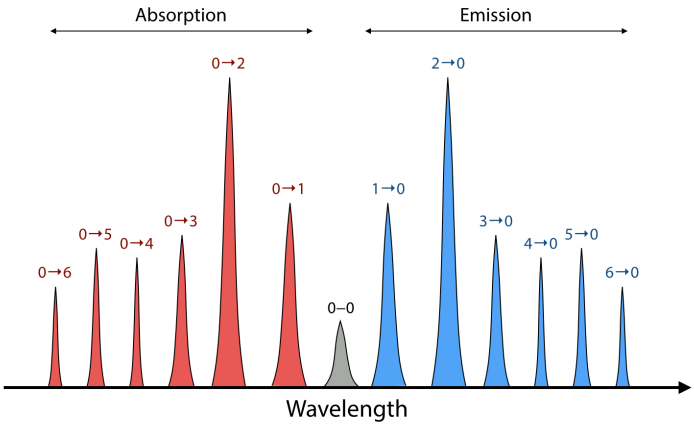

Fig. 1.4 Schematic representation of the absorption and emission spectrum. Without vibrations of the molecular skeleton, the spectrum appears a series of sharp lines with mirror symmetry.

The energy levels in an atom or a small molecule are discrete, thus the electronic transitions between the energy levels may appear as a series of sharp lines (Fig. 1.4). It is also easily expected that the absorption and emission spectrum have the mirror symmetry because the electronic transitions occur in the same structure of the electronic states. However, a fluorescent molecule generally has more than 50 atoms with at least 150 normal vibrations of the molecular skeleton. When such a molecule is excited, there is a change in bond length (typically 1~2 %) due to the change in electron density. The extended bond length instantly induces a new oscillation, and many of normal vibrations causing the broadening of spectrum are occurred in this manner in a general case of a large fluorescent molecule. In addition, molecular collisions and electrostatic perturbations due to the surrounding solvents as well as the rotational movements also contribute the spectral broadening. As a result, there is built a quasi-continuum of states superimposed on every electronic level, and the population of these levels in contact with

thermalized solvent molecules is determined by a Boltzmann distribution. Since the large molecules experience > 10^{12} collisions in a second with the solvents, the thermal equilibrium is reached in time on the order of one picosecond.[10]

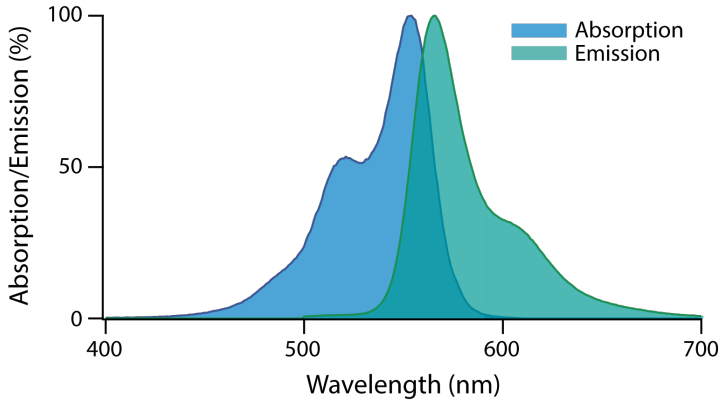

Fig. 1.5 Typical absorption and emission spectrums of a fluorescent molecule. The spectrums are normalized using their maximum values. A famous dye in the field of biophysics, Cy3, is used to the measurement.

Because of all of above reasons, the absorption and emission spectrum have the 'band' rather than the 'line' in symmetric manner (Fig. 1.5). Due to the vibrational relaxation, the emission spectrum appears in longer wavelength range (Stokes' shift). Furthermore, although the electron is excited to the higher excited states (S_2, S_3, …) due to the excess photon energy, the fast dissipation processes to the S_1 state via internal conversion make the emission spectrum independent to the excitation wavelength (Vavilov's rule).[11] Moreover, the polarity of a solvent and the local environment of the fluorescent molecule also can affect to the emission spectrum. The reason is that the fluorescence is occurred in nanosecond timescale, which is much longer than the timescale of molecular collision. On the other hand, the excitation is relatively fast (femtosecond) and the absorption spectrum is much less affected by the solvents. This dependence is well known as solvatochromism or perichromism, and the higher polarity of solvent shifts the emission spectrum to longer wavelength.[12]

1.2.4. Fluorescent Characteristics

• ***Extinction Coefficient (ε, $M^{-1}cm^{-1}$) and Absorption Cross Section (σ, cm^2)***

The extinction coefficient is a measurement of how strongly a chemical species absorbs light at a given wavelength. According to the Beer-Lambert law, the absorbance of a material depends on the pathlength and the concentration of the species, and thus is given by $A = \varepsilon cl$, where A, ε, c and l mean the absorbance, a proportional constant, concentration of the material and the pathlength, respectively.[13] It is an intrinsic property of the fluorescent molecules and is directly related to the absorption cross section, which is another quantity indicating the ability of a molecule to absorb the photons. The relationship between two quantities is given by $\sigma = \ln(10)\text{x}(1000\varepsilon/N_A)$, where N_A is the Avogadro constant.[12]

• ***Fluorescence Quantum Yield (Φ)***

The fluorescence quantum yield is the ratio of the number of photons emitted to the number absorbed. The populated excited state can be de-excited through both of radiative and non-radiative pathways. The fraction of fluorescent molecules that decay through emission, the quantum yield, is given by $\Phi = k_r / (k_r + k_{nr})$ where k_r and k_{nr} represent the rate for the radiative and non-radiative pathways, respectively.[12] The quantum yield can be close to unity if the k_{nr} is much less than the k_r. Since there always exists the Stokes loss, the quantum yield has to be less than unity.

• ***Fluorescence Lifetime (τ, ns)***

The fluorescence lifetime is defined by the average time, which the excited electron spends in the excited state before returning to the ground state. The lifetime generally given by $\tau = (k_r + k_{nr})^{-1}$, and typically it is on the range of nanosecond (1 ~ 10 ns).[12] Since the lifetime is an average value of the time spent in the excited state, just few molecules emit their photons at exact $t = \tau$. For a single exponential decay, ~63 % of the molecules decayed at $t < \tau$ and the rests decay at $t < \tau$. Since the measured fluorescence lifetime (i.e., time-correlated single photon

counting, TCSPC, measurement) is highly depends on the non-radiative rate, it is usually used as a marker to elucidate the environment around the fluorescent molecule.

1.3. Fluorophores

The 'fluorophore' is a generic term for the fluorescent molecules that can emit the photons upon light excitation. Generally, the researchers working with fluorescence are interested in transitions whose energy differences fall into the visible region of the electromagnetic spectrum (350~800 nm), thus the fluorophores have been developed with such emission properties. Since it is common that an interesting molecule does not emit the fluorescence, the fluorophores are widely used as a molecular probe to recognize the non-fluorescent interesting molecules. By using the fluorophores, we can investigate the molecular structure, movement, interaction, dynamics and kinetics of various samples with remarkable sensitivity.

1.3.1. Molecular Structure of Fluorophores

The general fluorescent molecules are unsaturated organic compounds consisting of hydrocarbons and their derivatives and containing more than one double or triple chemical bond. Without the unsaturated feature, the organic compounds usually absorb at wavelength below 160 nm, which is not visible and is also higher than dissociation energy of most chemical bonds. In order to absorb the visible light, chemically conjugated systems, which are effectively lower the energy gap between HOMO and LUMO, are required. For example, the carbon-carbon double bonds (−C=C−) absorb photons with wavelength of 170 nm, but if they were conjugated (−C=C−C=C−), the molecule can absorb at 220 nm.[14] Increasing the number of the conjugated bonds leads to the absorption and emission at longer

wavelength, thus the useful fluorophores have several conjugated double bonds in their chemical structure.

In conjugated systems, the π orbitals in double and triple bonds are extended over the whole molecule, and the electron can freely move around it. This is called the delocalization of electrons. A typical example for the delocalization of electrons is the benzene (C_6H_6, Fig. 1.6a). In benzene, the π orbitals are completely delocalized above and below of the plane of carbon. This feature allows the increased chemical stability and is called 'aromatic' due to historical reasons.[15]

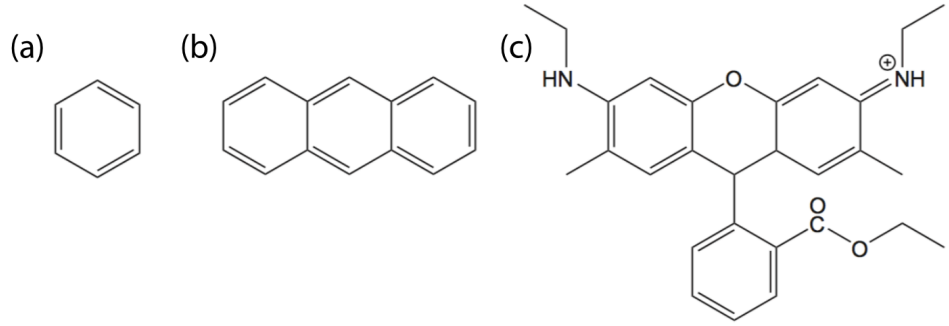

Fig. 1.6 Chemical structures of (a) benzene, (b) anthracene and (c) Rhodamine 6G. The fully conjugated π orbitals effectively delocalize the electrons and shift the absorption and emission bands to the visible region of spectrum.

Single aromatic ring strongly absorbs around 180 nm with weaker band at 200 nm. We can increase the conjugated system to shift the absorption bands to the visible region. The fully conjugated three aromatic rings, called anthracene (Fig. 1.6b), absorb light around 250 nm. Further modification that substitution of one of the central carbons in anthracene by oxygen makes xanthene, and shifts the absorption band to visible range. Xanthene derivatives are widely used as a fluorophore such as Fluorescein, Eosin and Rhodamine. They absorb in the blue to yellow region of the spectrum and emit from green to red region. In order to make better the chemical/photophysical properties and tune the absorption and emission bands, additional groups can be introduced and the famous example is the Rhodamine 6G (R6G, Fig. 1.6c) used in dye lasers.[16]

1.3.2. Examples of Frequently-used Fluorophores

• *Intrinsic Fluorophores*

In biological systems, there are naturally fluorescent molecules such as the indole group of tryptophan (Fig. 1.7a). Since the tryptophan is abundant in the protein, the fluorescence from indole used as the protein marker. Indole absorbs near 280 nm and emits near 340 nm, and the emission spectrum is highly sensitive to the solvent polarity. As well as indole group, a great variety of other substances in biological molecules display significant fluorescence: reduced nicotinamide adenine dinucleotide (NADH, Fig. 1.7b), oxidized flavin adenine dinucleotide (FAD, Fig. 1.7c) or mononucleotide (FMN), pyridoxyl phosphate, chlorophyll (Fig. 1.7d) and so on.[12]

• *Synthetic Fluorophores*

Although there exist the intrinsic fluorophores, a huge number of molecules in interest are not fluorescent. In order to observe and analyze these non-fluorescent targets, we used chemically synthesized organic fluorophores. Structurally, all of them have largely delocalized electron cloud to absorb or emit the photon in visible range, and many of them are based on the anthracene or cyanine derivatives. The most three famous families are named as Fluorescein, Rhodamine and Cyanine, and each family shares the core structure represented in Figure 1.7.

Fluorescein (Fig. 1.7e) is a dark red powder slightly soluble water and alcohol. It has the maximum absorption peak at 494 nm and emission peak at 521 nm. Interestingly, Fluorescein can be protonated or deprotonated in solutions with different pH and the absorption, emission and lifetime depend on the pH over the range of 5 to 9. Besides its use of fluorescent probe, Fluorescein is also used as a gain medium of dye laser. It has a famous derivative, fluorescein isothiocyanate (FITC), functionalized with an isothiocyanate group (−N=C=S), replacing a hydrogen atom on the bottom ring of the structure (Fig. 1.7f). The FITC is reactive toward primary amine group of biologically relevant compound including

intracellular proteins. Other derivatives of Fluorescein are also focused on the enhancement of its reactivity or photostability, and they commonly absorb the blue light and emit the fluorescence from 500 to 550 nm.

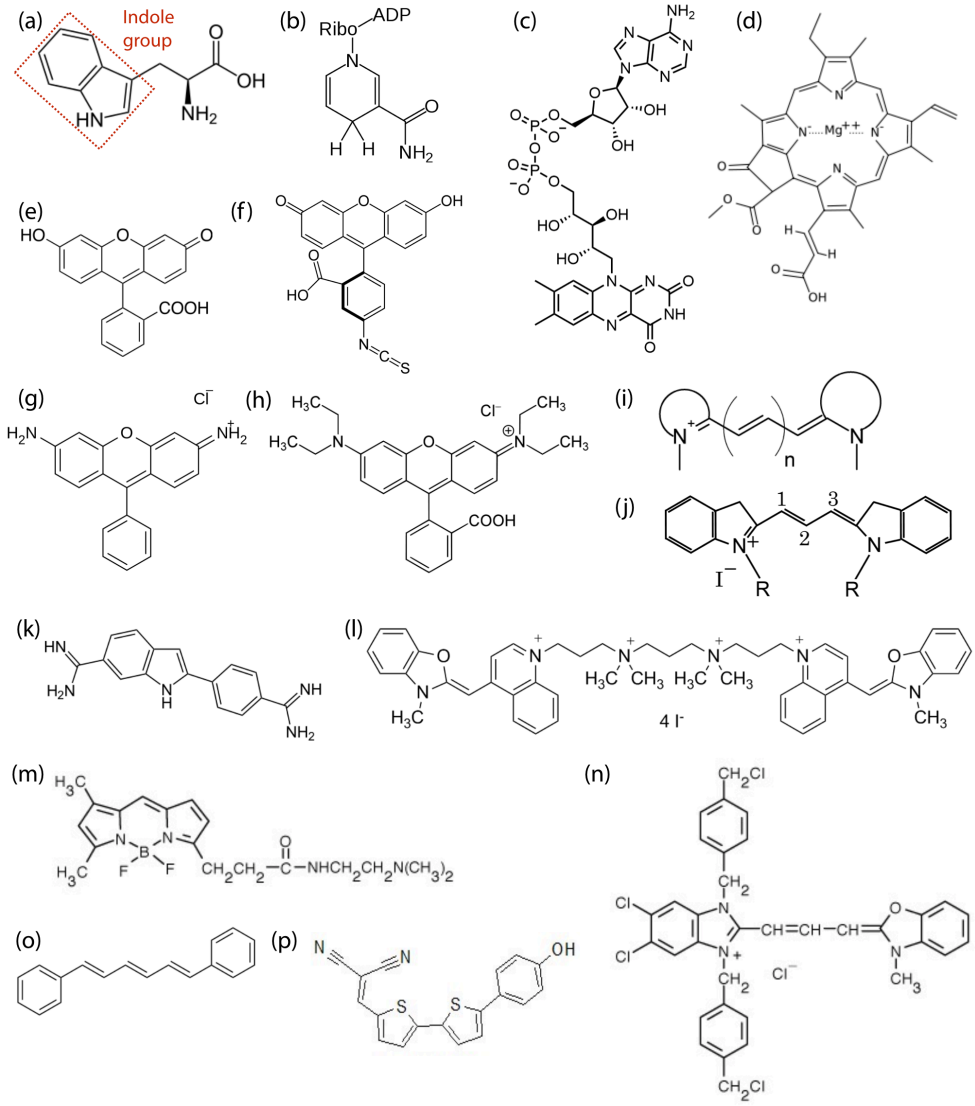

Fig. 1.7 Chemical structures of synthetic fluorophores. (a) Tryptophan, an amino acid, containing fluorescent indole group (red dotted square). (b)Nicotinamide adenine dinucleotide (NADH). (c) Flavin adenine dinucleotide (FAD). (d) Chlorophyll. (e) Core structure of Fluorescein. (f) Fluorescein isothiocyanate, FITC. (g) Core structure of Rhodamine. (h) Rhodamine 6G, R6G. (i) Core structure of cyanine. (j) Cy3, which has three carbons between two indole groups. (k) 4′,6-diamidino-2-phenylindole, DAPI. (l) YOYO fluorophore which belongs to monomethine cyanine family. (m) LysoTracker. (n) MitoTracker. (o) Diphenylhexatriene, DPH. (p) NIAD-4, which can bind to specific structured proteins, especially the amyloid proteins.

Rhodamine has two primary amine groups on the external aromatic rings of anthracene in symmetric manner (Fig. 1.7g). It does not used as the pure form itself, but has many of useful derivatives such as Rhodamine B (Fig. 1.7h), Rhodamine 6G (R6G), Rhodamine 123, Rhodamine RED, tetramethylrhodamine (TMR), carboxytetramethylrhodamine (TAMRA), and so on. By inserting additional functional group to the benzene rings of Rhodamine core structure, the emitting wavelength of the Rhodamine dyes is tunable from 500 to 750 nm, which covers almost of green-to-red range of visible spectrum. R6G is the most famous and widely used form of Rhodamine, which shows remarkable photostability and brightness (ε = 116,000 $M^{-1}cm^{-1}$, Φ = 0.95, Fig. 1.6c). The maximum absorption/emission peaks of R6G are located on 530/550 nm. Since it can be easily synthesized with low cost, it is commonly used as the gain medium in dye laser with lasing range from 555 to 585 nm, as well as the fluorescent marker or tracer dye.

Cyanine is a non-systematic name of a synthetic dye family, which has a polymethine chain between two functional groups (Fig. 1.7i). Typically, indole groups are linked by the polymethine chain to fluoresce in visible range. Depending on their structure, they cover the spectrum form infrared (IR) to ultraviolet (UV), as well as visible. Cyanine dyes are usually synthesized from 2, 3, 5 or 7 methine structures with reactive groups on either one or both of the nitrogen side chains so that they can be chemically linked to nucleic acids or protein molecules. Their fluorescent range is tuned by adjusting the length of polymethine linker or by slightly modifying the minor structures. Especially, Cy3 (Fig. 1.7j) and Cy5 are intensively used in the biological study to investigate the biomolecular structures and interactions by using the resonance energy transfer (RET).

Based on the three core structures, a numerous kinds of synthetic fluorophores have been developed. In the field of biology, the bright and photostable fluorophores such as Cy-, Alexa-, DY- and Atto- are the favorite species. Recently developed Star- fluorophores are specialized to the super-resolution imaging.

Although most of synthetic fluorophores have additional functional groups to target the molecules in interest, some fluorophores are able to directly bind on target structures. For example, we can use 4'6-diamino-2-phenylindole (DAPI, Fig. 1.7k) or YOYO fluorophores (Fig. 1.7l) to visualize the nucleic acids in cells. Since these fluorophores can transmit the cellular membrane, they also used to image the live cells. For cellular organelles, LysoTrackers (Fig. 1.7m) and Mitotrackers (Fig 1.7n) can be introduced to visualize them. Diphynylhexatriene (DPH, Fig. 1.7o) is efficiently intercalated to the cellular membrane and NIAD-4 (Fig. 1.7p) can bind to specific folding structure of proteins found in amyloid proteins. This kind of fluorophores usually transmit the cellular membrane, thus they are the excellent choice for living cell imaging. Some of the fluorophores, such as YOYO and NIAD-4, have an interesting feature that the fluorescence quantum yield greatly increased when such a fluorophore binds to target structure. This feature assures more diverse applications of the fluorophores in super-resolution imaging.

• ***Functional Groups***

For a biological application, the synthetic fluorophores have to be labeled on the target species. There also exist a number of functional groups, but the *N*-hydroxysuccinimide ester (NHS ester) and maleimide are the most used functional groups (Fig. 1.8). The NHS ester has a good leaving group, NHS, and it react with primary amines, which are easily attachable to the nucleic acids and are abundant in the proteins. Maleimide has a reactive double bond, which can make a covalent bond with thiols found on cysteine in proteins. It also reacts with hydroxyl and amine groups thus can be used to label various biomolecules. In addition to these two groups, numerous reactive functional groups are commercially available to label target molecules, including amine, hydrazide, azide, alkyne, carboxylic acid, and so on.

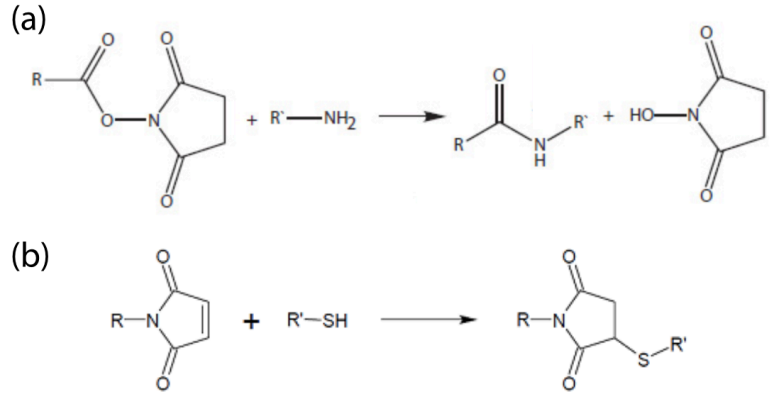

Fig. 1.8 Chemical reaction between the famous reactive functional groups and its target. (a) NHS ester functional group can react with primary amine to make amide bond. (b) Maleimide functional group reacts with primary thiol abundant in the proteins.

- ***Fluorescent Proteins***

Fluorescent proteins (FPs), as indicated by its name, are naturally being proteins that emit fluorescence under light illumination. The first observation of the fluorescent protein reported in 1962 by Osamu Shimomura et al., who found the 'green fluorescent protein (GFP)' in *Aequorea Victoria*.[17] GFP has 238 amino acids (26.9 kDa) folded in barrel shape made of 11 β-sheets linking with loop structure, and contains a chromophore that consist of three amino acids, Ser65-Tyr66-Gly67, which has the major absorption peak at 395 nm and emit the fluorescence with 509 nm maximum peak.[18] Since the proteins are easily expressed in living cells via genetic mutations, the fluorescent proteins have been grow a promising tool for bioimaging. Point mutation of the GFP varies the photophysical properties of the protein including absorption/emission bands, extinction coefficient and quantum yield. Nowadays, more than 50 kinds of FPs are available and they cover whole visible range of light spectrum.

- ***Fluorescent Nanoparticles***

As the nanotechnology has been rapidly grown in 21st century, fluorescent nanoparticles have also been developed and applied to the imaging and spectroscopy. A representative example is the quantum dots, which are tiny

particles (< 10 nm in size) consisting of semiconductors. In the small volume of quantum dots, there exist relatively low numbers of molecules and their electronic states are clearly discrete like as the electronic states in small molecules (c.f., band structure in bulk semiconductors). In this case, the electron in quantum dot can transit to the excited states under light illumination and emit the photons having energy comparable to the transition between electronic states, fluorescence. Since their energy gap depends on the size of the particle (i.e., the number of atoms in the particle), the absorption and emission wavelengths are easily tunable. Sometimes, there exist some surface defects that can induce the photoblinking of the fluorescence by trapping the electron, and core-shell structures are introduced to prevent the harmful photophysical phenomenon.

Another example of fluorescent nanoparticle is the fluorescent nanodiamonds (FNDs) containing the negatively nitrogen-vacancy (NV^-) color center.[19] The NV^- center is one of the defects found in bulk diamonds (which paint the diamonds with variety colors) and has optical absorption centered at 560 nm with following emission from 600 to 850 nm. Interestingly, the NV^- center shows non-blinking and non-bleaching properties due to the rigid structure of diamonds.

We can also use the fluorescent silica beads when we needed a robust fluorophore. Since the fluorescent silica beads contain a huge number of organic fluorophores, it is extremely brighter that any other fluorophores and never blinks in single particle level although it slowly bleaches under strong illumination.

All of these fluorescent nanoparticles need additional surface treatment to label something with them. Also, since the nanoparticles are more reactive due to their small size and consist of inorganic compounds, the cytotoxicity problem always arises in their biological applications. Nevertheless, their extraordinary photophysical properties are great advantages for fluorescent technique, thus researches for the advanced, nontoxic and functionalized fluorescent nanoparticles are continuously progressed.

1.4. Photophysics

The excited electron generated by light absorption of a molecule has enough internal energy to induce the diverse chemical and physical processes including the emission of the photon during de-excitation, fluorescence. Since the whole processes starts from the absorption, one of the light-matter interaction, these are generally called 'photophysics'.

1.4.1. Triplet States

Intersystem crossing (ISC) is one of the general relaxation pathways that every excited electron can experience stochastically. It is a non-radiative transition between two iso-energetic vibration sublevels belonging to electronic states of different multiplicities. The triplet state has a lower energy level than the excited singlet state, according to Hund's rule, due to the higher multiplicity.[8] In the view of energetics, the ISC is a dissipative process and is favorable. However, a spin flip is accompanied with ISC and classically these transitions are forbidden by quantum mechanics. The spin-orbit coupling, which is a coupling process between the orbital and spin magnetic moments, actually allows these forbidden transitions by mixing the vibrational sublevels of singlet and triplet states (Fig. 1.9). The heavy atoms (i.e., Br, I and Pb) and paramagnetic species (including oxygen) significantly influence to the spin-orbit coupling efficiency, thus change the rate of ISC.[20,21]

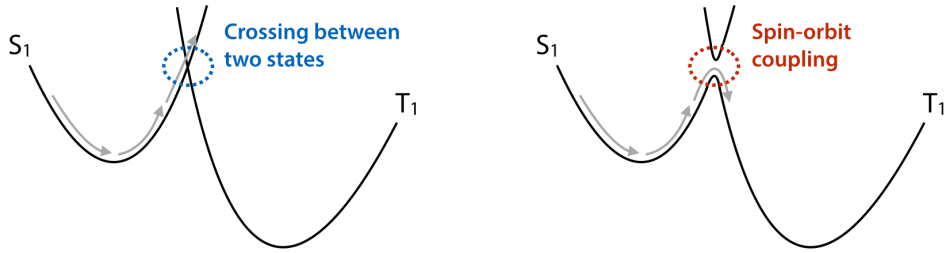

Fig. 1.9 Schematic energy diagram for the intersystem crossing (ISC). (left) The ISC is strictly forbidden for lowest vibrational singlet and triplet state. (right) The spin-orbit coupling partially allows the ISC near the crossing point of the energy curves.

After ISC process and following vibrational relaxation, the electron in the triplet state cannot easily return to the singlet state neither excited state nor ground state because the reverse transitions also require another forbidden spin flip. Since the excited singlet state has higher energy than the triplet state, the reverse ISC is more rarely observed, and it usually occurs between higher excited singlet and triplet states. In this reason, the triplet state generally has long lifetime in microsecond (μs) to millisecond (ms) range. Although the transition from the triplet state to the ground singlet state is unfavorable, finally it eventually occurs to dissipate the excess energy. The relaxation process can be either radiative (phosphorescence) or non-radiative (dissipation by heat or energy transfer to another molecule in triplet state, i.e., oxygen).

1.4.2. Isomerized States

When a fluorophore contains a double bond between carbon atoms, the cis/trans isomerization of the molecule should occur under light illumination (photoisomerization).[22] This is one of the relaxation process to dissipate the excess energy and results a new entity with different physical properties. Absorption and emission spectrums of cis- and trans- isomers are usually shifted in relation to each other, with cis- isomer being shifted more to the red region of visible spectrum.[22] On the other hand, the fluorescence brightness is significantly different between two isomers, where the cis- isomer is usually less brighter than trans- isomer due to

the large flexibility of the conjugated chain that makes non-radiative internal conversion to be the predominant pathways of relaxation process. Furthermore, the cis- isomer also generally unstable in terms of energetics since the straighter shape of the trans- isomer leads to hydrogen intermolecular forces that make the isomer more stable.

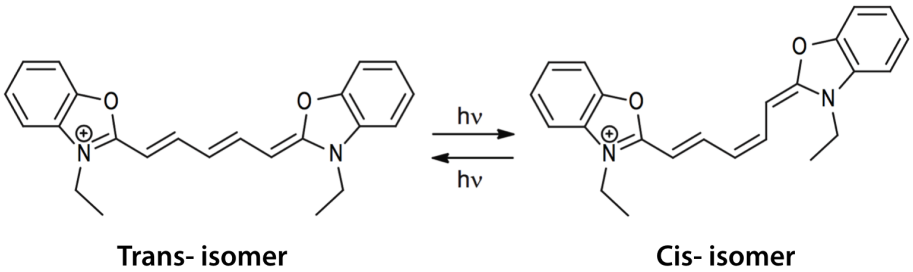

Fig. 2.10 Trans- and cis- isomers of Cy5. Under continuous light illumination with single wavelength, the photoinduced isomerization can take place in both directions and the population of both isomers reaches the chemical equilibrium.

Structurally, the cyanine dyes can undergo the photoisomerization upon excitation as a relaxation process. Since their polymethine chains consist of the single and double bonds in alternative manner, one of them can be rotated during the relaxation process of the excited electron (Fig. 1.10). Since the isomerization is induced by light illumination and shifts the absorption spectrum, the cis- and trans- isomers have different excitation rate for a single wavelength. Under continuous illumination of single wavelength, the populations of two isomerized states goes to the equilibrium, which is about 50 % in each state for Cy5 at excitation with 633 nm light.

Different environmental factors, such as viscosity, temperature, solvent polarity and steric hindrances, can influence the rate of isomerization. With the isomerized states, the triplet kinetics is rather inefficient due to the competition with effective relaxation via photoisomerization.

1.4.3. Fluorescence Quenching and Fluorescence Resonance Energy Transfer (FRET)

Sometimes, the fluorophores suffer from decrement of the fluorescence due to the excited state reactions, energy transfer, complex-formation, molecular collision and many other reasons.[12] All of such processes that suppress the fluorescence called as 'fluorescence quenching'. Since the quenching processes reduce the fluorescence output, generally they are perceived as undesirable processes. However, the molecular interactions that hard to be observed can be investigated indirectly by using the fluorescence quenching, another molecular interaction between the fluorophore and the quencher. A number of protein structures and dynamics, as well as protein-nucleotide interactions, are uncovered by using the quenching processes.[23-27]

• ***Quenching Mechanisms***

A famous example of the fluorescence quenching is that the fluorescence is quenched by certain anions.[28] The quenching ability is strongly depends on the chemical nature of the anion, where the iodide (I^-) and bromide (Br^-) show stronger quenching effect than the chloride (Cl^-). Although this anion-induced fluorescence quenching is well known, the exact mechanism still remains unclear. As one of the possibility, a charge transfer reaction is suggested in 1990.[29]

The electrons in triplet state cannot fluoresce, thus the ISC can be considered as a quenching process. Both of internal and external heavy atoms strikingly increase the rate of ISC, where the heavy atoms decrease the energy difference between singlet and triplet states due to the spin-orbit coupling.

When there are highly concentrated fluorophores in the solvent consists of small, highly polar molecules (i.e., water), their fluorescence can be quenched due to aggregation of fluorescent molecules.[30] In the polar solvents, the large and hydrophobic fluorophores tend to bring them together due to the dispersive forces and hydrophobic interactions. If the fluorophores are charged, the repulsive

Coulomb forces slightly counteracted. The aggregated fluorophores normally show weaker fluorescence intensity with distorted absorption spectrum.

Excited state reactions also induce the fluorescence quenching.[31] An excellent example is the R6G in ethanol which shows unchanged absorption spectrum even at higher concentration that 10 mM, meaning that the R6G does not aggregate in this condition. However, the fluorescence intensity is strongly reduced due to the collisions of the excited state molecules with those in the ground state.[32]

• ***Fluorescence Resonance Energy Transfer (FRET)***

The energy of excited electron can be transferred to another molecule through non-radiative dipole-dipole interaction. This fluorescence quenching by resonance energy transfer (RET) was suggested by Förster in 1948,[33] and now it is well known as fluorescence or Förster resonance energy transfer, FRET. The efficiency of energy transfer is strongly dependent on the distance between two molecules, thus it often used to measure the intermolecular distance less than 10 nm.

In order to easily measure the FRET experimentally, FRET between two fluorophores are commonly used, where the transferred energy also cause the fluorescence (Fig. 1.11a). In this case, the first excited fluorophore called as 'donor', and the other one called as 'acceptor'. An essential prerequisite for the FRET is that there has to be an spectral overlap between the emission spectrum of the donor and the absorption spectrum of the acceptor ($J(\nu)$), meaning the excited electron of the donor has enough energy to excite the acceptor molecule (Fig. 1.11b). The rate of energy transfer between donor and acceptor (k_T) depends on several factors, including the orientation factor, κ. Since the resonance energy transfer is resulted from the dipole-dipole interaction, the orientation of two fluorophores is closely related to the transfer efficiency. The fluorescence lifetime (τ_D) and quantum yield (Φ_D) of donor molecule affect to the efficiency because the RET only occurs when the electron exists in singlet excited state. All of these factors can be constant for a fixed FRET pair, thus we can introduce a new

parameter to simplify the expression for the k_T., and it is given by following equation.

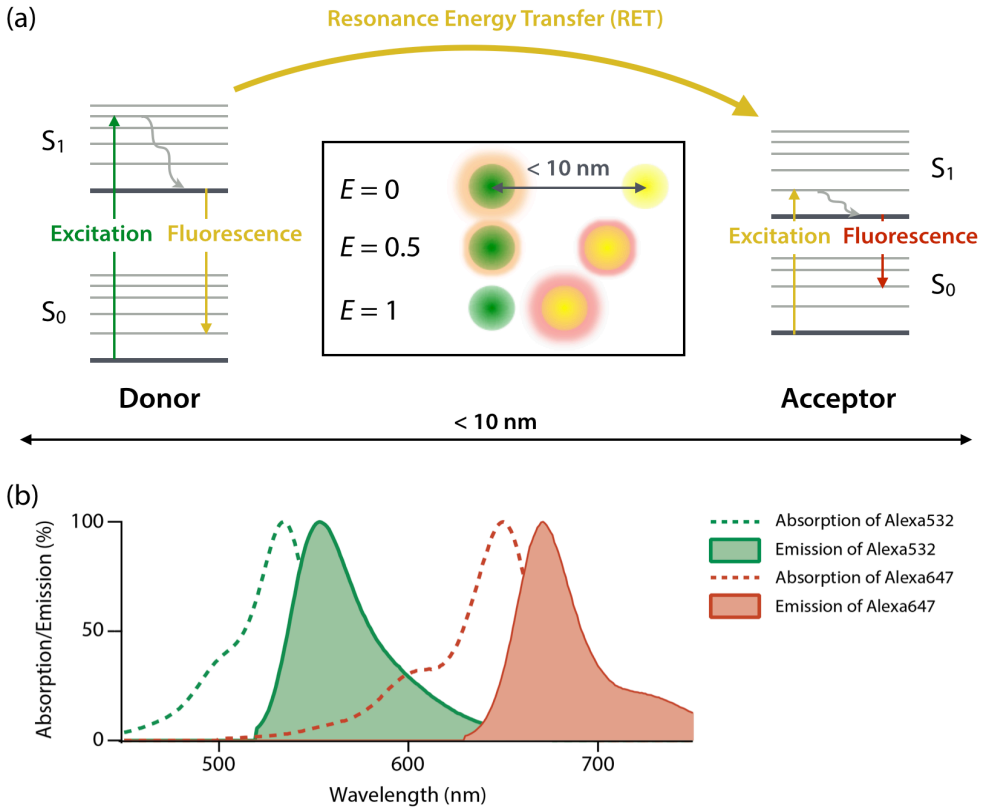

Fig. 1.11 (a) Schematic illustration for fluorescence resonance energy transfer (FRET) between two fluorophores. The excited electron of donor can undergo both of fluorescence or resonance energy transfer pathways. The transferred energy excites the acceptor molecule, resulting the emission of acceptor. The efficiency of FRET (*E*) strongly depends on the distance between two fluorophores. (b) Normalized absorption and emission spectrums of a famous FRET pair, Alexa532 (donor) and Alexa647 (acceptor). There is significant spectral overlap between the emission of donor and the absorption of acceptor.

$$k_T = \frac{9(\ln 10)\Phi_D \kappa^2 J(\upsilon)}{128\pi^5 N_A n^4 \tau_D R^6} = k_D \left[\frac{R_0}{R}\right]^6$$

Here, k_D is the rate of fluorescence and equals to $(\tau_D)^{-1}$ and R_0 is defined as $(8.785\text{x}10\text{-}25)\Phi_D\kappa^2 n^{-4} J(\nu)$ cm^6, and means the characteristic distance of the FRET pair where the half of energy of donor transferred to acceptor, and R is the actual distance between two fluorophores. Now we can consider about the ratio of transferred energy to absorbed photon energy, thus the FRET efficiency (E), as followed form.

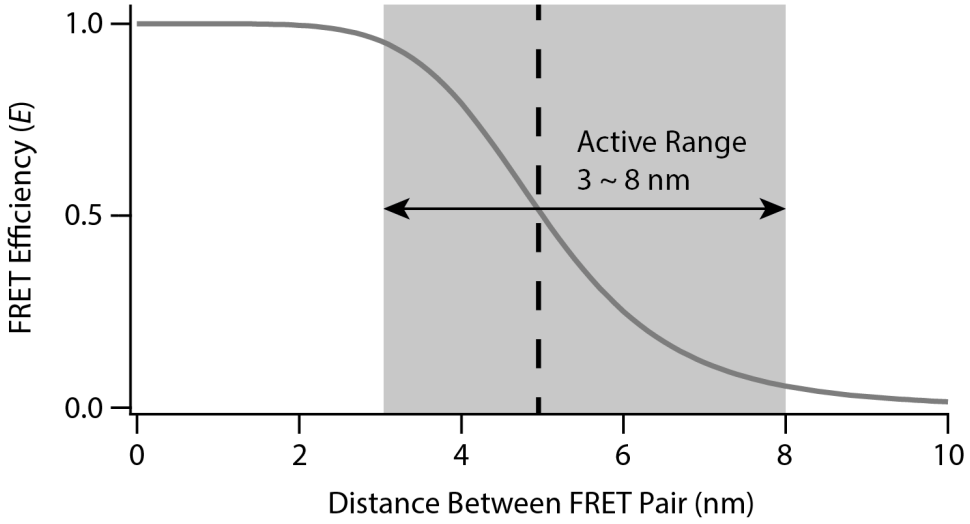

Fig. 1.12 Simulated FRET efficiency (*E*) of a FRET pair with R_0 = 5 nm. The *E* value highly depends on the distance at the range of 3 ~ 8 nm.

$$E = \frac{k_T}{k_D + k_T} = \frac{1}{1+(R/R_0)^6}$$

From this equation, we can notice that the *E* value is in inverse proportional to R^6, which shows a sensitive dependence to the intermolecular distance range with a center of R_0 (Fig. 1.12). General FRET pairs have R0 values in the range of < 10 nm, thus the FRET usually measures the intermolecular distance from 0 to 10 nm effectively. Since the size of the biomolecules and the distance range of their interaction are located in this range, the FRET is a very powerful tool for the biological sciences as a 'spectroscopic ruler'.[34]

1.4.4. Photoblinking

As we can see the 'blinking' in its name, the photoblinking means all the photophysical processes inducing temporal suppression of the fluorescence, including triplet, isomerized and quenched states discussed previously. Since the fluorescence generally acts as the meaningful signals for a measurement, the photoblinking is a reluctant process.

An electron in fluorophore visits the triplet state approximately once every 1,000 excitations. The lifetime of the triplet state is typically a few microseconds in aqueous solution with oxygen, because the oxygen effectively quenches the triplet state. When we remove the oxygen, however, the lifetime of triplet state increases to milliseconds.[35] Populated triplet state results averaged lower intensity in measurement with > 10 ms binning time, or more seriously induces rapid fluctuation between normal signal and zero levels.

Occasionally, photoinduced electron transfer can be occurred on the fluorophore resulting the radical ions. Both of oxidation and reduction are possibly occurs for excited electrons when a fluorophore collides with electron donors or acceptors. Resulted radical cations and anions typically do not fluoresce and have longer lifetime than milliseconds, thus, induces the photoblinking.[36]

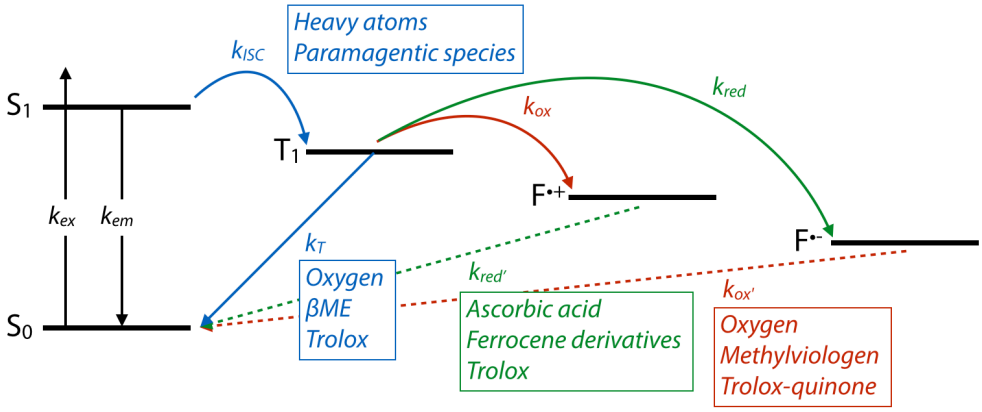

Fig. 1.13 Simplified Jablonski diagram with accessible states under different conditions. The excited electron in single state can be transferred to the triplet states or oxidized/reduced radical states whose lifetime has longer than a few milliseconds, thus inducing the photoblinking. Triplet quenchers and both of oxidant and reductant can effectively suppress the photoblinking process by quickly return the electron to the singlet ground state.

Figure 1.13 summarizes the typical photoblinking states in simplified Jablonski diagram. In order to avoid the undesirable photoblinking process, we can employ additional chemical reagents that reduce the lifetime of the triplet state and oxidized/reduced radical ion states. Especially, the trolox, a vitamin E analog, can

act as both of triplet quencher or oxidation/reduction reagents, and the trolox can powerfully suppress the photoblinking.

1.4.5. Photochromism and Photoswitching

Photochromism is a reversible transformation of a chemical species between two forms under light illumination, where the two forms show different absorption spectrum.[37] If a photochromic molecule can fluoresce in only one form, thus the fluorescence is switched by light illumination, we can call the fluorophore as a 'photoswitch'.

Photochromic properties are observed for single FPs[38] as well as organic molecules, including spiropyrans, prirooxazines, diarylethenes, azobenzenes and quinones. Such photochromic molecules can be paired with a proper fluorophore that can transfer the energy to only one form of photochromic molecule via RET to make the photoswitchable system. Generally, the intramolecular cyclization or cis/trans isomerization induce the photochromic properties. The photochromism also can serve as a source of the photoblinking, however, it is quite useful when the forward and reverse photochromic reactions occur in different wavelength so it is controllable. Some of cyanine dyes and the NV^- center in diamonds are also photoswitchable, and we will discuss about them later.

1.4.6. Photobleaching

The photobleaching is usually defined as the irreversible reactions to non-fluorescent forms of the fluorescent molecules in the excited state, mainly due to their interaction with molecular oxygen. The average number of fluorescent cycles before photobleaching depends on the molecular structure of fluorophore and the local environment.

Several mechanisms have been suggested to explain the photobleaching of a fluorophore, and it is generally accepted that the triplet and radical states are involved in the photobleaching mechanism. Relatively longer lifetime of these

states allows more chances for the interaction between the fluorophore and the environment. Two unpaired electrons in the triplet state, as well as in the radical states, are easily react with oxygen, impurities, solvents or other molecules to yield various non-fluorescent products. In order to observe the fluorophore for a long time, removing the molecular oxygen is essential to minimize the undesirable photobleaching process, although the molecular oxygen restores the triplet electron to the ground singlet state. In recent fluorescence technique, it is common to use the enzymatic oxygen scavenging systems such as GluOxy (glucose, glucose oxidase and catalase)[39] and PCA/PCD (protocatechuic acid and protocatechuate-3,4-dioxygenase)[40] to efficiently remove the oxygen in buffers.

1.5. Fluorescence Techniques

A great advantage of the fluorescence in the uses of its molecular probe is the remarkable sensitivity. Common organic, inorganic and biological molecules do not emit the fluorescence under light illumination, thus the fluorescence intrinsically provides an excellent signal-to-background (S/B) ratio. The development of improved photodetectors, which can sense even single photons with ultimately low noise, also allows the high signal-to-noise (S/N) ratio in the fluorescence techniques.

1.5.1. Fluorescence Microscopy and Nanoscopy

The most popular application of fluorescence is in optical microscope. Since the light can penetrate the biological samples and shows relatively lower toxicity than other microscopy techniques (i.e., electron microscope or scanning probe microscope), optical microscope has been grown as a fundamental tool for biological imaging. Thus the fluorescence microscope, which can see only the

molecules in interest with great sensitivity, is also widely used in biology as a vital tool to image the interior of living cells with molecular specificity.[41]

One critical weak point of the fluorescence microscope is the spatial resolution, which is physically limited by the diffraction of light.[42] In order to overcome this resolution limit, some researchers had investigated the new methods for super-resolved imaging in recent 20 years. As a result, a number of microscope techniques that break the diffraction limit were developed, improving the spatial resolution less than 10 nm, thus called 'nanoscopy'.[43]

The fluorescence microscope can be categorized in two groups by the way it works. The first one, 'scanning optical microscope', uses tightly focused light to illuminate the sample in tiny area and scans the sample with piezo-assisted stage to construct the final image. Another one, 'wide-field microscope', illuminates the sample on wide range and detects the signals from whole area with pixelated photodetectors based on the charge-coupled device (CCD).

• ***Confocal Microscopy***

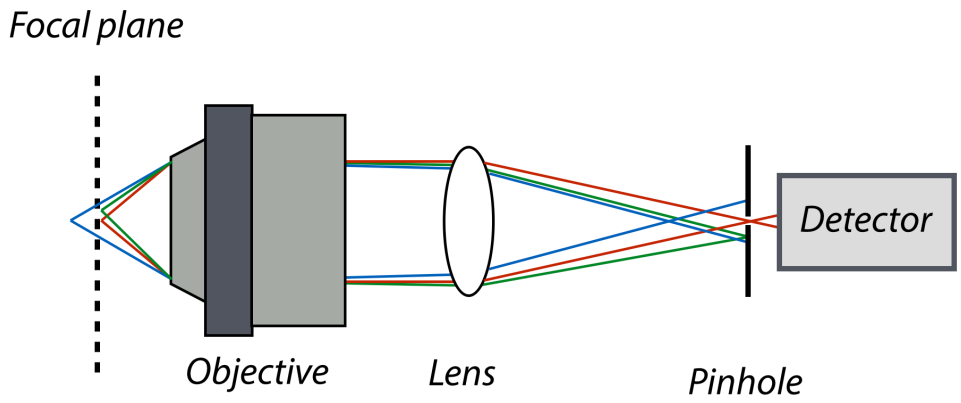

Fig. 1.14 Schematic illustration for the concept of the confocal microscopy. Tightly focused illumination light (not shown) selectively excites the fluorophore at the focus. Fluorescence from the focus is collected by the objective and is re-focused by a detection lens to pass through a pinhole put on the image plane (red line). However, the emitted light from out of the focus does not properly re-focused at the center of the pinhole where most of them are physically blocked by the pinhole (blue and green lines).

The confocal microscope belongs to the first group, and it introduces a pinhole in the light detection pathway to reduce out-of-focus signals (Fig. 1.14). With this

strategy, we can powerfully reduce the background signals from out of interesting region twice. First, in the excitation step, the tightly focused illumination light selectively excites the fluorophores in the focal volume. Second, a pinhole putting on the image plane by generated a detection lens physically blocks the fluorescence signals emitted from outside of the focus. As a result, the confocal microscope provides exceptionally great S/B ratio for a single image plane, and enables the three-dimensional (3D) sectioning of target specimen.

• ***Total Internal Reflection (TIR) Microscopy***

Total internal reflection (TIR) is a physical phenomenon that occurs at the interface between two mediums with different refractive indices (n_1, n_2). According to Snell's law, when a light is passing through the interface with incident angle θ_1 from the medium having refractive index n_1, the ray should be refracted at the interface with angle θ_2. In this case, the relationship between θ_1 and θ_2 is simply represented by $n_1(\sin\theta_1) = n_2(\sin\theta_2)$ (Fig. 1.15). If a light is travelling the interface satisfying $n_1 > n_2$, the total amount light can be reflected when the incident angle is larger than a certain angle (critical angle, $\theta_c = \sin^{-1}(n_2/n_1)$), thus called as 'total internal reflection (TIR)'.

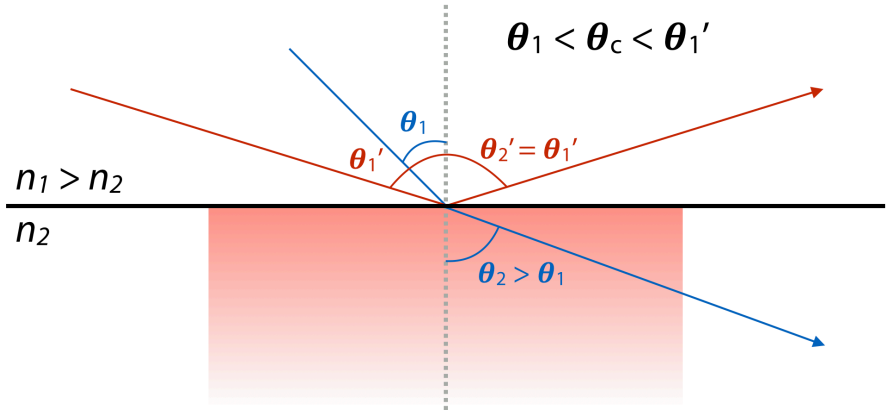

Fig. 1.15 Light refraction at the interface between two mediums with different refractive indices. When the incident angle is larger than the critical angle, the whole light energy are totally reflected at the interface. However, even there is no propagating ray in the second medium, the evanescent wave is generated for a few hundred nanometers in depth.

An interesting feature caused by TIR is the evanescent wave, whose intensity is exponentially decays along the axial direction. Even though the light no longer propagates into the second medium with TIR, there is a small amount of penetration of light across the interface, which then propagates parallel to the surface, creating an electromagnetic field in the second medium immediately adjacent to the interface.[44] By solving the Maxwell equations for this case, we can elicit that the z component of the wave vector for the refracted beam becomes imaginary. Thus the intensity of the light inside the medium with refractive index n_2 is not zero but decays exponentially with the distance, z, to the interface.

$$I(z) = I(0)\exp\left(-\frac{z}{d}\right) \qquad d = \frac{\lambda_0}{4\pi}(n_1^2 sin^2\theta - n_2^2)^{-1/2}$$

Here, d and λ_0 refer the penetration depth and the wavelength of incident light in vacuum, respectively. Notably, the penetration depth is related with the incident angle, as well as the refractive indices of two mediums and the wavelength of the incident light.

Typical penetration depth of the evanescent wave is less than few hundred nanometers, which is also much less than the axial length of tightly focused excitation volume. Therefore, we can selectively observe the fluorophore located on the surface with remarkably reduced backgrounds. This feature enables the single molecule detection, which requires extremely sensitive detection methods measurable the fluorescence from single molecule.

• ***Diffraction Limit in Optical Microscopy***

In optical microscope, the illumination light or the fluorescence has to be focused by illumination/detection lenses to effectively illuminate the sample or form the images. However, there must be the interference due to the diffraction of light between coherent photons during the focusing process, and the resulting focal volume cannot be smaller than a certain size, diffraction limit. The German physicist E. K. Abbe, who developed many important concepts, intensively studies

this phenomenon (thus the resolution limit often referred as Abbe's resolution limit).[42]

The optical resolution is defined by the ability of an imaging system to resolve details in the object. The point spread function (PSF), which is the response of an imaging system to a point source, mainly serves to the resolution limit. With an imaging system consists of perfect lenses, the infinitely small light source should be imaged as the diffraction limited focal volume. Ideal PSF of the point source should appear as the Airy disk, which can be successfully approximated with the Gaussian function. Especially, in the case of confocal microscope, the PSF will be squared because the diffraction of illumination source will be combined with the diffraction of the pinhole in the image plane. According to the empirical diffraction limit known as a Rayleigh criterion,[45] two point sources can be resolved when they are separated larger than the half of inter-first minima distance of the Airy disk.[46] Finally, we can mathematically describe the resolution limit of wide-field and confocal microscope as below.

$$\Delta r_{wide-field} = {}^{0.61\lambda}/_{NA} \qquad \Delta r_{confocal} = {}^{0.44\lambda}/_{NA}$$

$$\Delta z_{wide-field} = {}^{2n\lambda}/_{NA^2} \qquad \Delta z_{confocal} = {}^{1.41n\lambda}/_{NA^2}$$

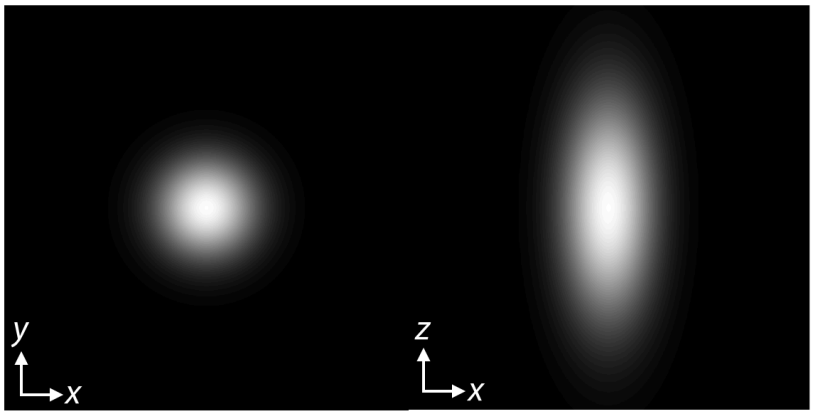

Fig. 1.16 Diffraction limited PSF of an optical microscope. When a light is focused by an imaging system, the focused light has to be larger than a certain size, even when the light is emitted from a point source. Since the size limit is due to the diffraction of light, the axial length of the PSF is larger than that of in lateral direction.

Here, the Δr and Δz refer the diffraction limit of lateral and axial planes (λ: wavelength of light; n: refractive index of medium; NA: numerical aperture that equals to $n\sin\theta$; θ: half-focusing angle of the lens;). Figure 1.16 shows the Gaussian-approximated PSF of an optical system.

In more general cases, with some aberrations in the optical system, the diffraction limit of an imaging system usually can be approximated as ~λ/2. Thus, we cannot clearly distinguish two object closer than ~250 nm with visible light in lateral plane.

• ***Fluorescence Nanoscopy***

The diffraction limit is a fatal disadvantage of the fluorescence microscope in their biological application, since the biomolecules are generally smaller than 100 nm. The first idea to break the diffraction limit is suggested by C. Cremer in 1978, where the axial resolution and the field of depth can be improved by using two opposite lenses (4π microscopy).[47] However, since the concept requires a complex optical system with precise alignment, sensitive photodetector, accurate scanning system and effective illumination source, its first experimental demonstration was barely achieved in 1994 by the German physician S. W. Hell.[48] After then, the super-resolution nanoscopy techniques have been intensively investigated and now they achieved a remarkable spatial resolution less than 20 nm in lateral plane and 50 nm in axial plane.

Although a number of fluorescence nanoscopy techniques working in individual way have been developed, all the nanoscopy use a salient process, the switching between fluorescent and non-fluorescent states of the fluorophores.[49] We can categorize the nanoscopy techniques into two groups by whether the switching occurs randomly or not.

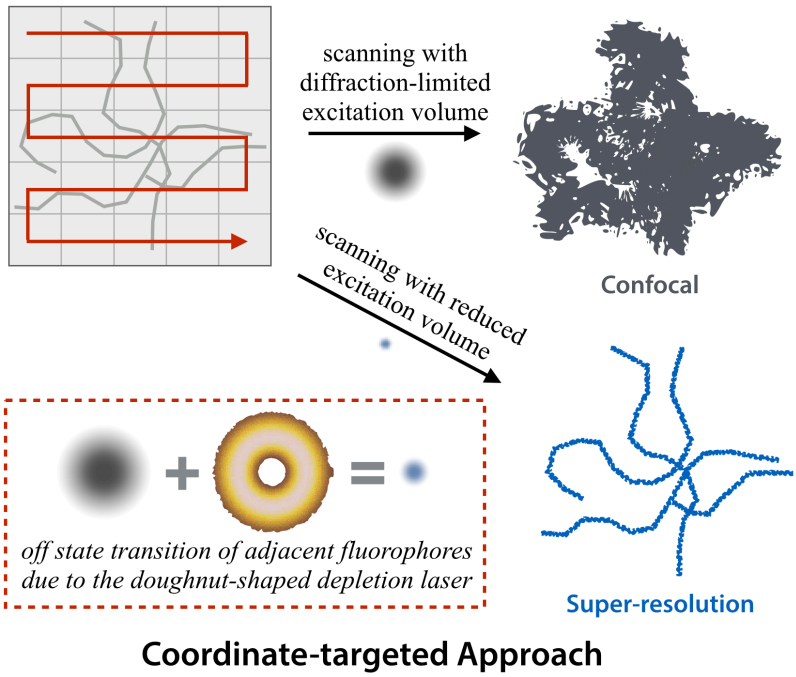

Fig. 1.17 Coordinate-targeted approach is based on the confocal microscope. Additional doughnut-shaped illumination pattern is introduced to turn-off the fluorophore at the specific position. Resulting reduced excitation volume leads to the super-resolved image.

The first group is called as 'coordinate-targeted approaches', realized in a stimulated emission depletion (STED),[50] ground state depletion (GSD)[51] or reversible saturable optical linear fluorescence transition (RESOLFT)[52] nanoscope, reversibly inhibits the occupation of the bright state everywhere but at specific points in space such that a detected signal is only allowed in coordinate regions of sub-diffraction limited size. For this purpose, an additional intensity distribution is introduced, which features at least on intensity zero to transiently confine the occupation of usually the fluorescent state to sub-diffraction limit sized area or volumes. Scanning of these points is required to completely construct the super-resolved image to the sample (Fig. 1.17). In this approach, the spatial resolution in lateral plane depends on the intensity of additional turn-off laser, as given by the full width at half maximum (FWHM) of the observaion area $d \approx \lambda/[NA(1+I/I_s)^{-1}]$.

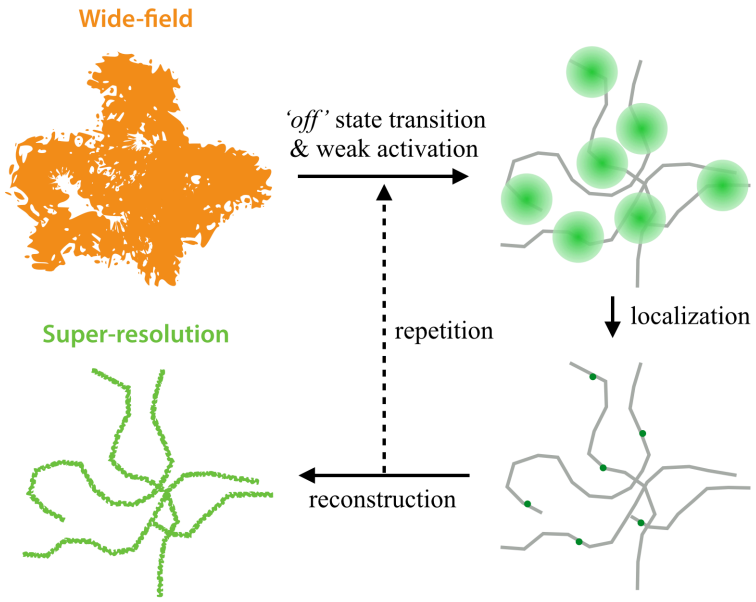

Fig. 1.18 In the coordinate-stochastic approaches, the fluorophores are stochastically switched at the random positions. Their population equilibrium assures that the fluorophore in the fluorescent state can be isolated individually to localize their center positions with nanometer accuracy. A reconstruction process is required to complete the super-resolution imaging.

The second group is 'coordinate-stochastic approach' such as fluorescence photoactivation localization microscopy ((f)PALM)[53,54] or stochastic optical reconstruction microscopy (STORM),[55] which inhibits the population of the fluorescent state everywhere but from single molecules per region of diffraction, whose spatial position can be exactly determined with nanometric precision. Subsequent stochastic state transitions of all individual molecules and the determinatino of their positions allow the reconstruction of a super-resolved image (Fig. 1.18). It is well known that the emitted fluorescence pattern of the indivisual fluorophores can be approximated to a Gaussian function and following localization of it can estimate the center position with one nanometer accuracy.[56] Repetative stochastic switching on/off enables the localization of the fluorophore in whole imaging area.

Nowadays. These fluorescence nanoscopy techniques provide < 20 nm spatial resolution for the multi-color 3D imaging of the biological samples, sometimes even with video-rate temporal resolution. It is becoming obvious that the fluorescence nanoscopy opens up unprecedented possibilities for biophysical and medical research. Widespread availability of instrumentation and expertise and the targeted application to important problems will enable the full impact of the nanoscopy to be realized, with many answers to ling-standing scientific quests.

1.5.2. Fluorescence Correlation Spectroscopy (FCS)

FCS is a diffusion-based pseudo-single molecule spectroscopic technique, which has interest in the analysis of the fluctuation of fluorescence time profile. FCS has many applications because a wide variety of processes can result in intensity fluctuations, such as translational/rotational diffusion, ICS, intermolecular binding/dissociation, excited reactions any formation process of dark state.[12] FCS is now being commonly used to biochemical analysis, especially to the dynamics of membrane proteins.

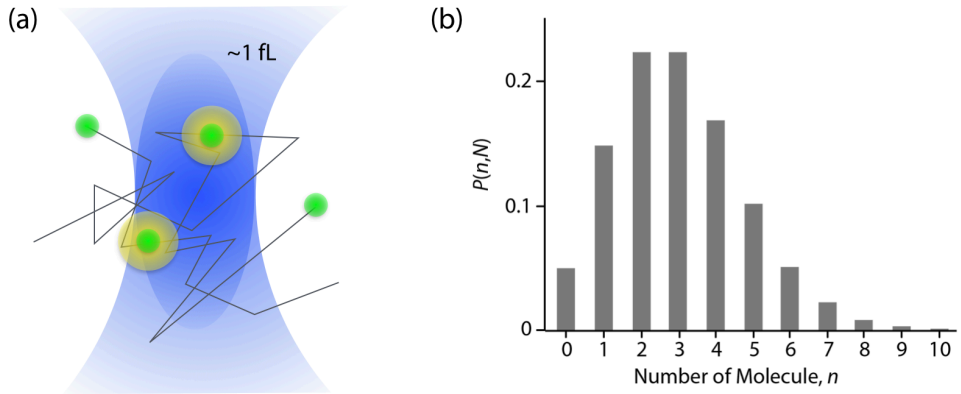

Fig. 1.19 (a) Effective detection volume in confocal microscope. The detection volume is about 1 fL and only the molecules in this volume can be detected. (b) Probability histogram for the number of fluorophores in the 1 fL detection volume at 5 nM concentrations. There are just few molecules in the volume.

The measurement of FCS is performed by using a confocal microscope, which provides both of high S/N and S/B ratios. Typically, the detection volume of

confocal microscope generated by the pinhole is ~1 femtoliter (fL, Fig. 1.19a). We can only detect the fluorescence in this volume, and the probability density to the number of fluorescent molecules in confocal area can be determined by the Poisson distribution.[57]

$$P(n,N) = \frac{N^n}{n!}e^{-N}$$

Here, $P(n,N)$ is the probability of n fluorophores being present in the volume when the average number of molecules in the volume is N. Since the fluorescent molecules continuously diffuse, the number of fluorophores in the volume at certain time is not a constant, so there has to be the fluctuation in fluorescence time trace. General concentration range of the fluorescent molecules for FCS is 1 to 10 nM where there are only a few molecules in the detection volume (Fig. 1.19b).

Resulting fluorescence time trace shows averaged fluorescence intensity with stochastic fluctuations. These fluctuations is analyzed by the autocorrelation function, given by the product of the intensity at time t, $F(t)$, with the intensity after a delay time τ, $F(t+\tau)$. With normalization by average intensity squared, the autocorrelation function, $G(\tau)$, is given by,

$$G(\tau) = \frac{<F(t)F(t+\tau)>}{<F><F>} = \frac{<\delta F(t)\delta F(\tau)>}{<F>^2}$$

, where $\delta F(t) = <F> - F(t)$. The fluorescence intensity at time t is related several factors including the brightness of fluorophore ($B = q\sigma\Phi$), collection efficiency ($CEF(r)$), excitation intensity distribution ($I(r)$) and concentration distribution at certain time t ($C(r,t)$).[12] The brightness factor is determined by the quantum yield, absorption cross section and the quantum efficiency of detector (q), thus it has to be a constant for all time and space.

$$F(t) = B \int CEF(r)I(r)C(r,t)dV$$

The product of CEF(r) and I(r) means the molecular detection efficiency, and we can describe that in mathematical way by approximating the detection volume as a 3D Gaussian shape with radial (s) and axial (u) $1/e^2$ radii.

$$CEF(r)I(r) = p(r) = I_0 \exp\left[-\frac{2(x^2+y^2)}{s^2}\right] \exp\left(-\frac{2z^2}{u^2}\right)$$

$$G(\tau) = \frac{B^2 \iint p(r)p(r') < \delta C(r,t)\delta C(r',\tau) > dV dV'}{[BC \int p(r) dV]^2}$$

Now we can consider the (perhaps) most common application of FCS, the measurement of translational diffusion. In this case, we will assume that the distribution of fluorophore, $C(r,t)$ depends on the diffusion only, and is described as below.

$$< \delta C(r,t)\delta C(r',\tau) > = \bar{C}(4\pi D\tau)^{3/2} \exp\left[-\frac{|r-r'|^2}{4D\tau}\right]$$

$$G_D(\tau) = \frac{1}{N}\left(1+\frac{\tau}{\tau_D}\right)^{-1}\left(1+\frac{\tau}{k^2\tau_D}\right)^{-\frac{1}{2}}$$

Here, $G_D(\tau)$, N, τ_D, k and D are the autocorrelation function for the translational diffusion, average number of the fluorophore, diffusion time, the aspect ratio of the focal volume (u/s) and the diffusion coefficient of fluorophore, respectively. Thus we can measure the diffusion coefficient of a fluorescent target molecule by using the relationship $\tau_D = s^2/4D$ (Fig. 1.20). Furthermore, additional information related to the translational diffusion such as molecular weigh and solvent viscosity can also be derived from the FCS measurement.

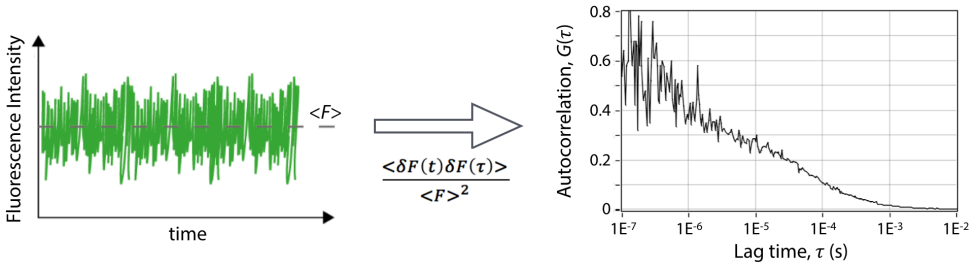

Fig. 1.20 Autocorrelation of the fluorescence intensity profile results a decay curve, which shows rapid slope in the time scale of photophysics influencing the fluorescence fluctuation. By fitting the $G(\tau)$ with physically derived equation, we can determine the characteristic coefficients related to the physical events.

Common fluorescent probes have the first excited triplet state as a dark state, which causes the intensity fluctuations. With enough excitation intensity, this triplet state can be significantly populated and appears in the autocorrelation

function at the short lag time regions. This additional photophysical flickering can be expressed another exponential term involving two parameters, fraction of the molecules in the triplet state F_T and the triplet relaxation time τ_T, in the autocorrelation function.

$$G_T(\tau) = 1 + \frac{F_T}{1-F_T} exp\left(-\frac{\tau}{\tau_T}\right)$$

$$G(\tau) = \frac{1}{N}\left(1 + \frac{\tau}{\tau_D}\right)^{-1}\left(1 + \frac{\tau}{k^2\tau_D}\right)^{-\frac{1}{2}}\left[1 + \frac{F_T}{1-F_T} exp\left(-\frac{\tau}{\tau_T}\right)\right]$$

Since the triplet dynamics is affected by several photophysical parameters, we can determine all of these parameters with FCS by using above equation, including absorption cross section, rate of ISC, lifetime of triplet state and the photobleaching quantum yield.[58,59]

In the same way, we can determine all of the photophysical parameters of a fluorescent molecule, which are affected to the fluorescence fluctuation with FCS, by precisely derive the proper function to the physical phenomenon. Moreover, the interactions between molecules or the diffusion dynamics can also be monitored by this technique. It can cover the whole time range of the photophysics from the excitation of the electron to the photobleaching (Fig. 1.21).

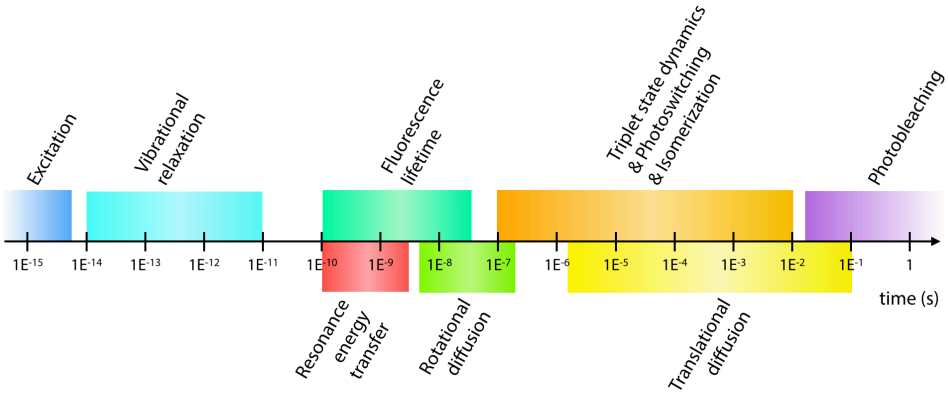

Fig. 1.21 Overall time scale of the photophysical processes. Since the photophysical processes usually affect to the fluorescence intensity, FCS can measure the photophysical parameters related to them. (FCS can analyze all of the represented events, only except the vibrational relaxation that does not affect to the fluorescence intensity.)

1.5.3. Single Molecule Techniques Utilizing FRET

As a powerful tool to investigate the molecular dynamics and interactions of biomolecules, the single molecule spectroscopy has been grown up as a vital tool for the biological researches since the single molecule was firstly detected in ambient conditions.[60] It has a great advantage to avoid the ensemble average, which leads to misunderstanding of target systems. Moreover, its ability to observe the individual molecule more than ~100 seconds enables the direct observation of molecular dynamics. For the efficient biological applications, single molecule techniques are often utilizing FRET, which can precisely measure the inter-fluorophore distance in the range of 3 ~ 8 nm, comparable with the size of biomolecules and the distance between biomolecular interactions.

A major factor that enables the single molecule detection is the efficient removal of background signal to achieve high S/N ratio even with single molecule fluorescence. Two technical approaches are widely used to reduce the background signal such as Raman scattering of solvents and fluorescence from impurities – confocal detection and TIR excitation. As we seen in previous sections, these two techniques provide high S/N ratio by using the pinhole (for confocal detection) or evanescent wave (for TIR excitation).

Typically, the confocal-based single molecule techniques observe the diffused molecule since they excite the tiny focal volume. To detect the individual diffusing molecule, the average concentration should be lower than ~100 pM, according to Poisson distribution, where the focal volume is mainly filled up with no molecule but occasionally a single molecule is passing through the volume. For the conventional fluorophores, the diffusion time is less than ~100 μs for the molecule itself due to their small size, and less than ~1 ms even when they are labeled on biomolecule such as nucleic acid or proteins. Thus the observation time of single molecule detection in the confocal mode is typically too short to investigate the molecular dynamics. However, it can count lots of single molecule events for a

long time, and gives plenty of samples enough to be used for kinetic information by statistic analysis.

In the case of using TIR excitation to observe single molecules, the fluorophore should be tethered on the surface of glass coverslip because the evanescent wave propagates only few hundred nanometers along *z*-axis. With a proper imaging condition (i.e., containing the oxygen scavenger and the triplet quencher), we can see the immobilized single molecule even longer than 10 minutes without undesirable photoblinking. In other words, we can directly observe the dynamics of biomolecules at single molecule level. Since ~100 molecules in the field of view simultaneously excited and detected by the evanescent wave and EMCCD in a single measurement, the kinetic information is also easily figured out as well as the dynamics.

FRET can provide a number of valuable information about the biomolecules by measuring the intermolecular distance in single molecule experiments. For the FRET measurements, the target molecules should be labeled with two fluorophores, donor and acceptor, and the fluorescence from each fluorophore is also detected distinctly. Experimentally, the FRET efficiency can be measured by comparing the detected fluorescence of donor and acceptor.

$$E = \frac{1}{1+(R/R_0)^6} = \frac{F_D^A}{F_D^A+\gamma F_D^D}$$

Here, the notation F_X^Y is used to indicate the detected fluorescence of *Y* molecule under *X*-absorbable light illumination, and *D* and *A* mark the donor and acceptor, respectively. γ (called as 'gamma factor') is a normalizing factor for the difference of detection efficiency from quantum yields of two fluorophores and instrumentation, equals to $(\Phi_A\eta_A)(\Phi_D\eta_D)^{-1}$ (Φ_X: quantum yield of *X* molecule; η_X: detection efficiency for the fluorescence from *X* molecule;).

Single molecule techniques are still evolving and branching out in many research fields. However, it still has some agendas, such as more accessible *in vivo* and *in situ* measurement, combination with multiple techniques, better

spatial/temporal resolutions and the enhanced fluorophores, to be able to take its place in the arsenal of general biology tools.

1.6. References

1. B. Valeur, *Molecular Fluorescence: Principles and Applications*, Wiley-VCH (2002).
2. D. Brewster, *Trans. Roy. Soc. Edinburgh* **12**, 538 (1833).
3. G. G. Stokes, *Phil. Trans. R. Soc. Lond.* **142**, 463 (1852).
4. J. Franck and E. G. Dymond, *Trans. Faraday Soc.* **21**, 536 (1926).
5. E. Condon, *Phys. Rev.* **28**, 1182 (1926).
6. M. Kasha, *Discuss. Faraday Soc.* **9**, 14 (1950).
7. A. Jablonski, *Z. Phys. A-Hadron. Nucl.* **94**, 38 (1935).
8. C. N. Banwell and E. M. McCash, *Fundamentals of Molecular Spectroscopy*, London, McGraw-Hill (1994).
9. N. J. Turro, V. Ramamurthy and J. C. Scaiano, *Principles of Molecular Photochemistry: An Introduction*, Sausalito, California, University Science Books (2009).
10. F. P. Schäfer, *Principles of Dye Laser Operation. Dye Lasers*, Berlin, Springer-Verlag (1990).
11. S. J. Wawilow, *Phys. A-Hadron Nucl.* **42**, 311 (1927).
12. J. R. Lakowicz, *Principles of Fluorescence Spectroscopy*, New York, Springer (2006).
13. J. D. J. Ingle and S. R. Crouch, *Spectrochemical Analysis*, New Jersey, Prentice Hall (1988).
14. L. D. S. Yadav, *Organic Spectroscopy*, Dodrecht, Springer Netherlands (2004).
15. J. B. Birks, *Photophysics of Aromatic Molecules*, London, John Wiley & Sons Ltd. (1970).

16. F. J. Duarte and L. W. Hillman, *Dye Laser Principles, with Applications*, Academic Press (1990).
17. O. Shimomura et al., *J. Cell Comp. Physiol.* **59**, 223 (1962).
18. D. M. Chudakov et al., *Physiol. Rev.* **90**, 1103 (2010).
19. F. Jelezko and J. Wrachtrup, *Phys. Stat. Sol. A* **203**, 3207 (2006).
20. S. Sp. McGlynn et al., *Molecular Spectroscopy of the Triplet State*, Englewood Cliffs, New Jersey, Prentice-Hall (1969).
21. G. J. Hoijtink, *Mol. Phys.* **3**, 67 (1960).
22. P. J. McCartin, *J. Chem. Phys.* **42**, 2980 (1965).
23. M. R. Eftink and C. A. Ghiron, *Anal. Biochem.* **114**, 199 (1981).
24. C. A. M. Seidel et al., *J. Phys. Chem.* **100**, 5541 (1996).
25. G. Bonnet et al., *Proc. Natl. Acad. Sci.* **95**, 8602 (1998).
26. X. Zhuang et al., *Proc. Natl. Acad. Sci.* **97**, 14241 (2000).
27. D. Nettels et al., *Proc. Natl. Acad. Sci.* **104**, 2655 (2007).
28. P. Pringsheim, *Fluorescence & Phosphorescence*, New York, Wiley InterScience (1949).
29. K. -H. Drexhage, *Structure and Properties of Laser Dyes, Dye Lasers*, F. P. Schäfer, Berlin, Springer-Verlag (1990).
30. V. I. Yuzhakov, *Russ. Chem. Rev.*, **61**, 613 (1992).
31. V. Tomin, *Opt. Spectrosc.* **105**, 496 (2008).
32. E. G. Baranova, *Opt. Spectrosc.* **18**, 230 (1965).
33. T. Förster, *Annalen der Physik* **437**, 55 (1948).
34. P. R. Selven, *Nat. Struc. Biol.* **7**, 730 (2000).
35. T. Basche et al., *Nature* **373**, 132 (1995).
36. T. Ha and P. Tinnefeld, *Annu. Rev. Phys. Chem.* **63**, 595 (2012).
37. M. Irie, *Chem. Rev.* **100**, 683 (2000).
38. R. M. Dickson et al., *Nature* **388**, 355 (1997).
39. Y. Harada et al., *J. Mol. Biol.* **216**, 49 (1990).
40. C. E. Aitken et al., *Biophys. J.* **94**, 1826 (2008).

41. B. Huang et al., *Nat. Methods* **5**, 1047 (2008).
42. E. Abbe, *Arch. Mikrosk. Anat.* **9**, 413 (1873).
43. C. Eggeling et al., *Q. Rev. BIophys.* **48**, 178 (2015).
44. E. Hecht, *Optics*, Addison Wesley (2001).
45. F. R. S. Rayleigh, *Philos. Mag.* **8**, 261 (1879).
46. G. B. Airy, *Trans. Cambridge Philos. Soc.* **5**, 283 (1835).
47. C. Cremer and T. Cremer, *Microsc. Acta.* **81**, 31 (1978).
48. S. W. Hell et al., *Opt. Lett.* **19**, 222 (1994).
49. S. W. Hell, *Nat. Methods* **6**, 24 (2009).
50. S. W. Hell and J. Wichmann, *Opt. Lett.* **19**, 780 (1994).
51. S. W. Hell and M. Kroug, *Appl. Phys. B* **60**, 495 (1996).
52. S. W. Hell et al., *Appl. Phys. A* **77**, 859 (2003).
53. E. Betzig et al., *Science* **313**, 1642 (2006).
54. S. Hess et al., *Biophys. J.* **91**, 4258 (2006).
55. M. Rust et al., *Nat. Methods* **3**, 793 (2006).
56. A. Yildiz et al., *Science* **300**, 2061 (2003).
57. S. D. Poisson, *Research on the Probability of Judgments in Criminal and Civil Matters*, Paris, Bachelier (1837).
58. J. Widengren et al., *J. Phys. Chem.* **99**, 13368 (1995).
59. J. Widengren and R. Rigler, *Bioimaging* **4**, 149 (1996).
60. J. K. Trautman et al., *Nature* **369**, 40 (1994).

Chapter 2.

RESOLFT Nanoscopy with Photoswitchable Organic Fluorophores

2.1. Introduction

Since 1994, a number of far-field optical microscopy techniques have been proposed to overcome the optical diffraction limit.[1-3] Although each of these fluorescence nanoscopy ("super-resolution imaging") techniques uses distinct strategy, all of them share an identical core mechanism, i.e., switching between a 'bright' (fluorescent, "ON") state and a 'dark' (non-fluorescent, "OFF") state.[4] In contrast to the single-molecule based localization techniques (PALM/STORM/GSDIM),[5-8] the coordinate-targeted microscopy techniques such as stimulated emission depletion (STED) or ground state depletion (GSD) generally use the reduction of the effective focal volume. This is done by concentrically overlaying a circular excitation beam with a donut-shaped depletion beam, leading to the pre-emptive decay of off-center fluorophores to a dark state.[9,10] The singlet ground state often acts as the dark state in STED while the first triplet excited state plays the same role in GSD.

There is yet another approach, simply called RESOLFT (reversible saturable optical fluorescence transition), which usually exploits reversibly photoswitchable fluorescent proteins (rsFPs).[11-13] Due to the efficient transitions of rsFPs between the bright and dark states, it requires much smaller laser intensity than STED and GSD microscopy. Since the photoinduced dark state is often thermally stable,[14] the residual fluorescence tends to be low in RESOLFT. Because rsFPs can be easily

expressed in living cells via genetic engineering, RESOLFT nanoscopy is viewed as a promising tool for biological applications.[15-17] For example, thanks to the low operating laser intensity, even a living brain tissue was visualized with nanometric resolution for a long observation time with negligible photodamage.[18] Recently developed RESOLFT technique enables an efficient dual-color imaging of spectrally undistinguishable fluorescent proteins by using the difference of fluorescent kinetics.[19] Furthermore, this feature also allows parallelized RESOLFT nanoscopy with > 20,000 doughnut-like intensity minima, which greatly reduces the acquisition time.[20]

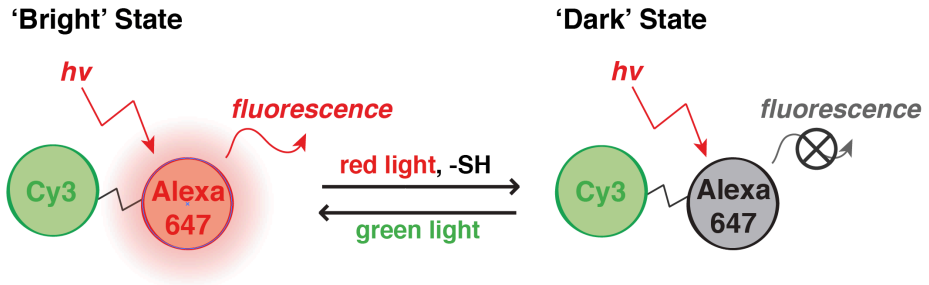

Fig. 2.1 Photoswitching of cyanine dye. A photoswitchable fluorophore, Alexa647, can be turned off when we applied a red light with primary thiols. The dark state of Alexa647 is an adduct of thiol embedded to the polymethine chain. Green light can restore the Alexa647 to the bright state, where the efficiency is greatly increased with neighboring Cy3, a green absorption dye.

Compared to fluorescent proteins, however, we note that organic fluorophores are much smaller in size, more versatile, and usually of better photophysical characteristics.[22-23] Organic dyes have never been used in RESOLFT nanoscopy for a biological system although there is a report for the demonstration of RESOLFT with an organic dye.[24] We here adopt the most widely-used cyanine dyes to implement organic dye-based RESOLFT nanoscopy. When a cyanine dye is excited in a buffer solution containing a small primary thiol, it forms a long-lived non-fluorescent state as a result of the thiol addition to the polymethine chain of the cyanine dye.[25-27] Illumination with a light of a wavelength shorter than 550 nm restores the photoproduct to the original fluorescent form.[25,26] Since it is well

known that a neighboring fluorophore that absorbs the restoring light can greatly enhance the restoring efficiency,[25,28] we attempted to maximize the photoswitching and labeling efficiencies by covalently linking the 'activator' and 'reporter' dye pair, Cy3-Alexa647, into a 'heterodimer' (Fig. 2.1).[28,29] We performed a series of pump-probe experiments to examine the photoswitching characteristics of this heterodimer under RESOLFT imaging conditions, and successfully obtained the RESOLFT images of cellular cytoskeleton using organic fluorophores.

2.2. Methods

2.2.1. Experimental Setup

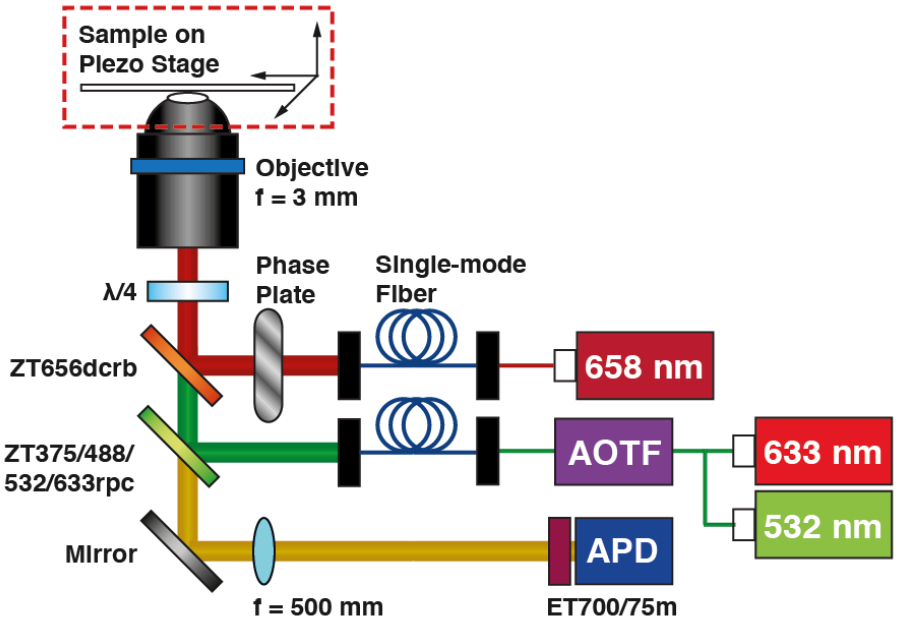

Fig. 2.2 A home-built confocal microscopy setup for the pump-probe experiment and RESOLFT imaging. In each pixel, a sequence of pulses is applied to the sample to achieve the sub-diffraction limit resolution.

A home-built fluorescence confocal microscope was used to examine photoswitching characteristics of Cy3-Alexa647 in various conditions and in RSOLFT imaging (Fig. 2.2).

Three continuous-wave lasers (532 nm: Samba^{TM} 532, *Cobolt*; 633 nm: 25-LHP-928-230, *CVI Melles-Griot*; 658 nm: TECRL-50GC-658-TTL-A, *World Star Tech*) were employed to generate the activation, probe, and depletion beams, respectively. The outputs of the 532-nm and 633-nm lasers were combined by using a dichroic filter (ZT532rdc, *Chroma*) and passed through an acousto-optic tunable filter (AOTFnC-VIS-TN, *AA Optoelectronic*) that performs active modulation of the millisecond beams. On the other hand, the 658-nm laser was modulated by external TTL scheme. All three laser beams were spatially filtered with single-mode fibers (Φ = 4.2 μm, P1-630PM-FC, *Thorlabs*) and finally combined in the same beam path using two dichroic filters (ZT656dcrb and ZT375/488/532/633rpc, *Chroma*).

The combined beams were sent through an oil-immersion objective (UIS2 series, PlanApo N, NA1.4, 100x, *Olympus*). In RESOLFT imaging, a vortex phase plate (VPP-1, *RPC Photonics*) was inserted in the beam path of the 658 nm laser. Achromatic $\lambda/4$ and $\lambda/2$ retarders (RAC 3.4.15, RAC 3.2.15 and RAC 4.2.15, *Bernhard Halle Nachfl.*) were used to make circularly polarized lights to generate minimum intensity at the center of the donut beam. The sample was placed on a piezo-stage (Nanomax Max311, *Thorlabs*) that can be scanned with < 5-nm accuracy.

All electrical input signals were generated by two analog output boards (PCI-6731 and PCI-6713, *National Instruments*) to control the 658-nm laser, AOTF and piezo-stage. The fluorescence signal was filtered through an emission filter (ET700/75m, *Chroma*) and fed into a multi-mode fiber (Φ = 62.5 μm, M31L02, *Thorlabs*) that works as a pinhole. The fluorescence signal was collected by an avalanche photodiode (SPCM-AQR-14FC, *Perkin Elmer*) and processed by a multi-channel scaler (P7882, *Fast ComTech*) that converted the analog signal to photon counts, which were finally visualized by an imaging program, Imspector.

2.2.2. Pump-probe Analysis

In order to successfully implement organic fluorophores in RESOLFT nanoscopy, the experimental conditions need to be optimized to improve the spatial resolution while avoiding photobleaching at the same time. The spatial resolution of RESOLFT nanoscopy is critically governed by the transition efficiency that is determined by two factors, the cross section of the optical transition and the photon flux of the depletion laser.[11] The former is highly affected by the chemical composition of the imaging buffer and the photophysical properties of the 'reporter' dye, whereas the latter is controlled by the irradiation intensity and the duration of the depletion laser. On the other hand, for fluorescence recovery, the cross section for photoactivation and the photon flux of the activation laser are the key factors.

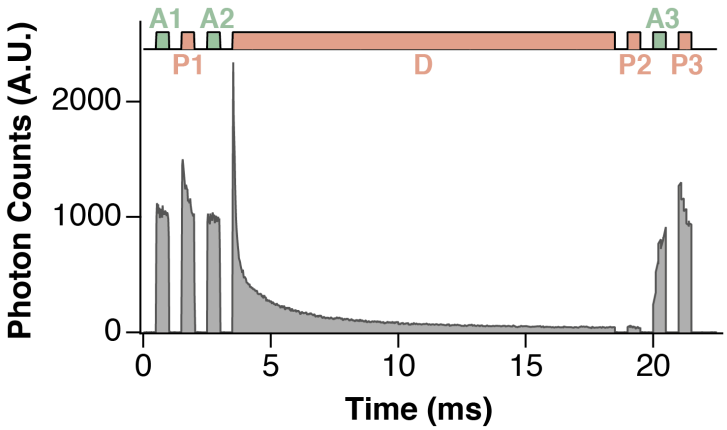

Fig. 2.3 Pulse train sequence for the pump-probe experiment. One sequence of pulses is applied to each pixel during sample scanning.

We performed pump-probe experiments in the millisecond range to analyze the photoswitching characteristics of the heterodimer in various conditions with a home-built microscope (Fig. 2.3). A series of pulses was repeatedly applied to a tightly focused region of the sample while it was being scanned. We combined seven pulses in a period, which consists of three activation pulses (532 nm; *A1*, *A2*, and *A3*), one depletion pulse (658 nm; *D*), and three probe pulses (633 nm; *P1*, *P2*, and *P3*). Pulses *A1*, *A2*, and *A3* are applied when the sample is needed to be activated, pulse *D* actually depletes the fluorophore to the dark state, and pulses *P1*,

P2, and *P3* read out the fluorescence after depletion (*P2*) and activation (*P3*) and also from reference state (*P1*).

The switching efficiency was analyzed by calculating the residual fluorescence level, F_D = 100x[(*P2*-F_{bg})/(*P1*-F_{bg})], and the recovered fluorescence level, F_R = 100x[(*P3*-*P2*)/(*P1*-*P2*)], where F_{bg} represents the background signal from the intervals with laser turned off. In order to obtain correct information about photoswitching, it is essential to prevent photobleaching and run many switching cycles to maximize the signal-to-noise (S/N) ratio. In order to satisfy these conditions, we scanned the immobilized heterodimers on a 8 x 8 μm^2 area with sufficiently large pixel size of ~600 nm, which is certainly larger than the diffraction limit. Each pixel has 1024 bins and a binning time of 22 μs (i.e., ~22.5 ms for a sweep), thus the pulse sequence was applied only once to a pixel to ensure minimal photobleaching. All of the pump-probe measurements were carried out 5 times in separate regions and their values were averaged.

2.2.3. RESOLFT Imaging

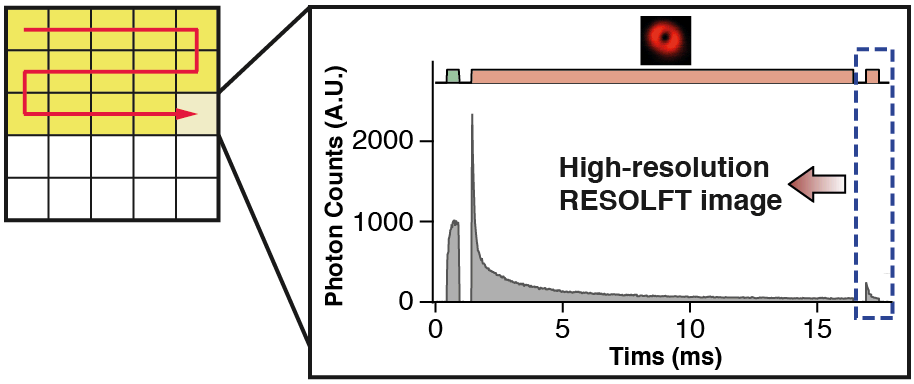

Fig. 2.4 Experimental scheme for RESOLFT imaging. Simpler pulse sequence was applied to each pixel during the scanning process. To make the reduced excitation volume, a doughnut-shaped depletion pulse was used.

In order to acquire the super-resolved image with RESOLFT scheme, we composed three pulses, which are corresponded *A2*, *D*, *P2* in pump-probe measurement. These activation, depletion and probe pulses are applied to the

scanned pixels in a pump-probe manner with the probe pulse used to visualize the RESOLFT image (Fig. 2.4). Here, the depletion beam was doughnut-shaped while the other two beams are of the circular type.

2.3. Sample Preparation

2.3.1. Synthesis of Cy3-Alexa647 Heterodimer

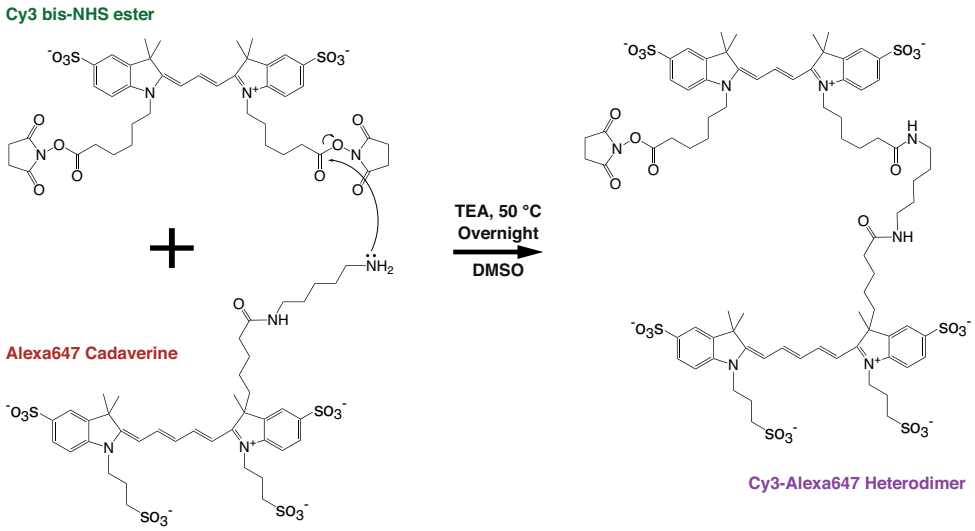

Fig. 2.5 Scheme for the synthesis of covalently-linked Cy3-Alexa647 heterodimer through a click reaction between one of the NHS ester groups of Cy3 and the amine group of Alexa647. Overall reaction was carried out in anhydrous DMSO to prevent hydrolysis of the NHS ester group. The other remaining NHS ester group can be used for further labeling processes.

The Cy3-Alexa647 heterodimer was synthesized by covalently linking the Cy3 bis-NHS ester (PA23000, *GE Healthcare*) and the Alexa647 cadaverine (MOP-A-30679, *Invitrogen*) in anhydrous dimethyl sulfoxide (276855, *Sigma Aldrich*) with 8 mM triethylamine (T0886, *Sigma Aldrich*)[28,29] (Fig. 2.5). The molar ratio of the reactants was Cy3 : Alexa647 = 3 : 1 (6 mM : 2 mM) to avoid the common, dually labeled product Cy3 bis-Alexa647. After 5 hours of incubation at 50 °C, we purified the Cy3-Alexa647 heterodimer by high performance liquid chromatography (1100 series, *Agilent Technologies*) using the C18 reverse phase

column (RPC C2/C18 ST 4.6/100, *GE Healthcare*) with a polarity gradient by controlling the solvent ratio between acetonitrile (9017-03, *J. T. Baker*) and 5% v/v acetonitrile + 50 mM triethylammonium acetate (60-4110-57, *Glen Research*) solution. We used freeze-drying (FD8508, *iLShinBioBase*) to remove the buffer and obtain the heterodimer in a solid form. Additional optical properties of the heterodimer were analyzed by absorption spectrometer (Lambda25, *Perkin Elmer*) and fluorescence spectrometer (Quantamaster, *Photon Technology International*) (Fig. 2.6).

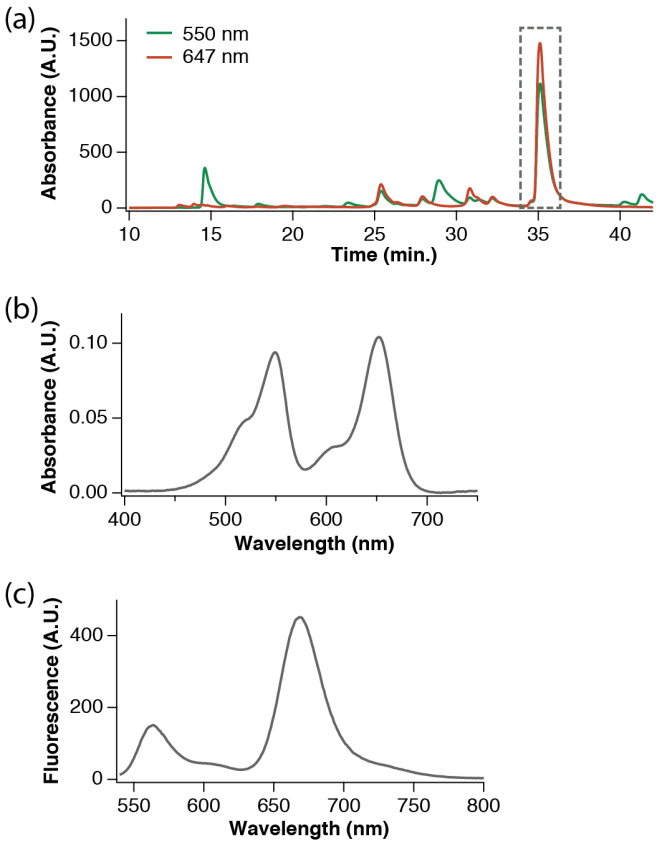

Fig. 2.6 (a) HPLC data for purification of Cy3-Alexa647 heterodimer. The heterodimer peak (in dashed-line box) shows strong absorption at both 550 nm and 647 nm. We collected this fraction and confirmed its absorption and emission characteristics. (b) Absorption spectrum of Cy3-Alexa647 heterodimer. Both species show their own absorption spectra but there is a slight change in the extinction coefficient due to the covalent bond formation. (c) Fluorescence emission spectrum of Cy3-Alexa647 heterodimer excited at 532 nm, showing emission from both fluorophores including FRET emission.

2.3.2. Labeling of Secondary Antibody with Heterodimer

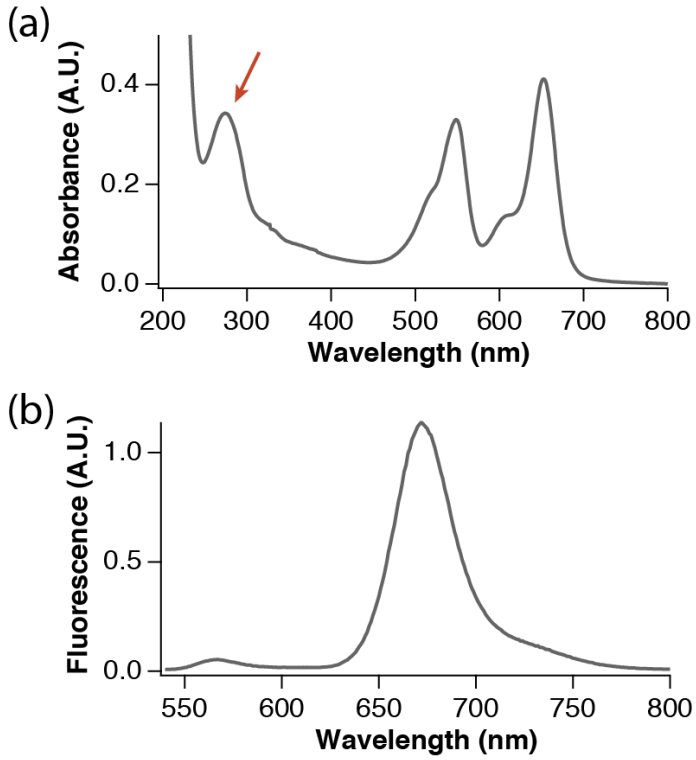

Fig. 2.7 (a) Absorption spectrum of Cy3-Alexa647 labeled secondary antibody. The strong absorption bands in the UV region (< 300 nm) are due to the secondary antibody. The ratio between the three peaks at 280 nm (red arrow, antibody protein), 540 nm (Cy3), and 640 nm (Alexa647) was used to choose the correct fraction in the purification process. (b) Fluorescence emission spectrum of Cy3-Alexa647 labeled secondary antibody excited at 532 nm. Two emission bands are still clearly visible although there is some enhancement in FRET efficiency due to the neighboring protein.

Labeling was carried out by reacting the Cy3-Alexa647 heterodimer with a secondary antibody (anti-mouse IgG produced in goat, F5262, *Sigma Aldrich*) in sodium borate buffer (0.1 M, pH = 8.5, 71999, *Sigma Aldrich*). The final concentrations of the reagents were roughly 200 μM and 4 μM for the heterodimer and secondary antibody, respectively. The remaining NHS-ester functional group of the heterodimer should nonspecifically react with the amines of the secondary antibody. The reaction was kept on for more than 12 hours at 4 °C, after which the product was purified by a size-exclusive desalting column (PD-10, *GE Healthcare*)

with phosphate buffered silane (PBS, 1x). We took the fraction that shows three absorption peaks (protein, Cy3 and Alexa647) simultaneously in the UV-VIS absorption spectrum. By measuring the absorption and emission spectra, we confirmed that the optical properties of the heterodimer were well preserved after labeling (Fig. 2.7).

2.3.3. Staining of Microtubules in a Fixed HeLa Cell

HeLa cells were cultured on a microscope cover glass in a six-well plate. We grew them in Dulbecco's modified Eagle's medium (LM001-79, *Welgene*) containing 10% v/v fetal bovine serum (16000-044, *Gibco*) and 1% v/v penicillin streptomycin (15140-122, *Gibco*) until their population was appropriate. We fixed the cells by using methanol (A452-4, *Fisher*) at –20 °C for 15 minutes and incubated them at 4 °C for 30 minutes with staining buffer containing 1% v/v bovine serum albumin (0332, *Amresco*) and 0.1% v/v triton X-100 (T8787, *Sigma Aldrich*) in PBS buffer.

After this, the primary antibody (monoclonal anti-β-tubulin antibody produced in mouse, T4026, *Sigma Aldrich*) was applied to the staining buffer with 1% v/v concentration, and the cells were incubated at 4 °C for 5 hours. The prepared secondary antibody was diluted about 30 times using staining buffer, applied to cells, and we incubated them in the same condition with the primary antibody. In each step, we washed the sample with 1x PBS buffer rigorously. Finally, we exchanged the buffer to a solution with 10 mM Tris pH 8.0 (AM9855G, *Ambion*), 50 mM NaCl (S3014, *Sigma Aldrich*), an oxygen scavenger system made of 10% w/v β-D-glucose (G0047, *TCI America*), 50 μg/mL glucose oxidase (G2133, *Sigma Aldrich*), 10 μg/mL catalase (C30, *Sigma Aldrich*), and proper concentrations of primary thiols (β-mercaptoethanol, βME, M6250, *Sigma Aldrich*; β-mercaptoethylamine, MEA, M6500, *Sigma Aldrich*; L-cysteine methyl ester, L-cys-ME, 30160, *Fluka*) and KI for further experiments. We tested the activity of our heterodimer-labeled antibody by confirming the co-localization with

commercially available FITC-labeled secondary antibody (F5262, *Sigma Aldrich*) (Fig. 2.8).

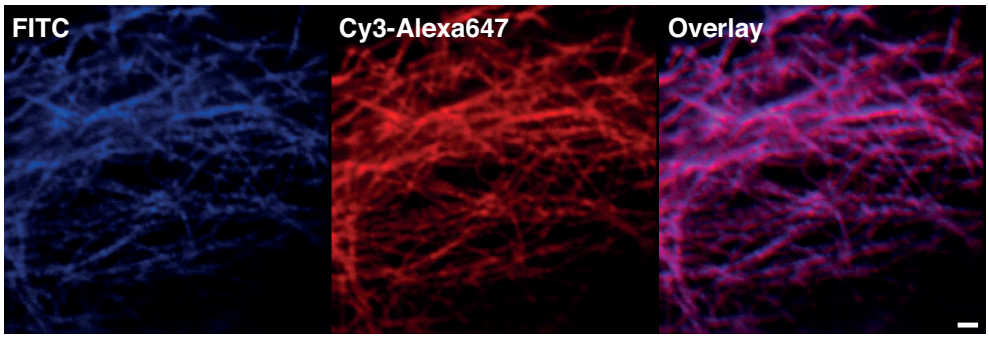

Fig. 2.8 Verification of the activity of the Cy3-Alexa647 labeled secondary antibody by confocal microscopy. A commercially available secondary antibody, FITC (F5262, *Sigma Aldrich*), was used as the reference. The color pattern of the overlay image confirms that both signals from FITC and Cy3-Alexa647 are identically located, indicating that the labeling process of Cy3-Alexa647 on the secondary antibody does not affect the activity of the latter. Scale bar: 1 μm.

2.4. Result and Discussion

2.4.1. Switching Properties of Cy3-Alexa647 Heterodimer

In order to see if organic fluorophores can be used in RESOLFT nanoscopy, we examined the photoswitching capability of the Cy3-Alexa647 heterodimer under imaging conditions over many repeated cycles (Fig. 2.9). The fluorescence intensity of the heterodimer was measured while repetitively irradiating red and green lasers at the focal volume. A corresponding fluorescence on/off signal was obtained for more than dozens of times with a minor degree of photobleaching (Fig. 2.9a). More than 80% of the Cy3-Alexa647 heterodimers survive after ~30 switching cycles and thus appear to be far more fatigue-resistant against photobleaching than Atto532 that has been widely used in GSD microscopy (Fig. 2.9b). The durability of the Cy3-Alexa647 photoswitching may likely ensure its wide range of applications in the RESOLFT scheme.

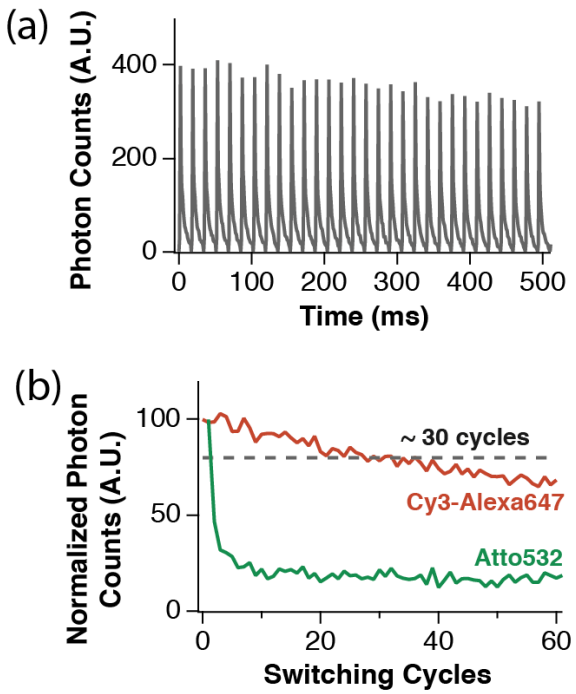

Fig. 2.9 (a) Fluorescence emission showing the on/off cycles upon repetitive ms-pulsed irradiation. (b) Photobleaching behavior of Cy3-Alexa647 vs. Atto532 against the number of switching cycles.

2.4.2. Optimization of Imaging Buffer

Increasing the transition cross section was achieved by optimizing the imaging buffer. First, we investigated the switching efficiency of three primary thiols: βME, MEA and L-cys-ME. Since the thiols show a saturation behavior in the concentration range of > 100 mM to form the dark state,[30] we used 143 mM of thiols that corresponds to 1% v/v of βME. Figure 2.10a compares the F_D and F_R values of our fluorophore in the presence of individual thiol species and oxygen scavenger with 50 mM KI. It is obvious that MEA gives the best results for both switching directions, and we thus used MEA in all pump-probe measurements and RESOLFT imaging.

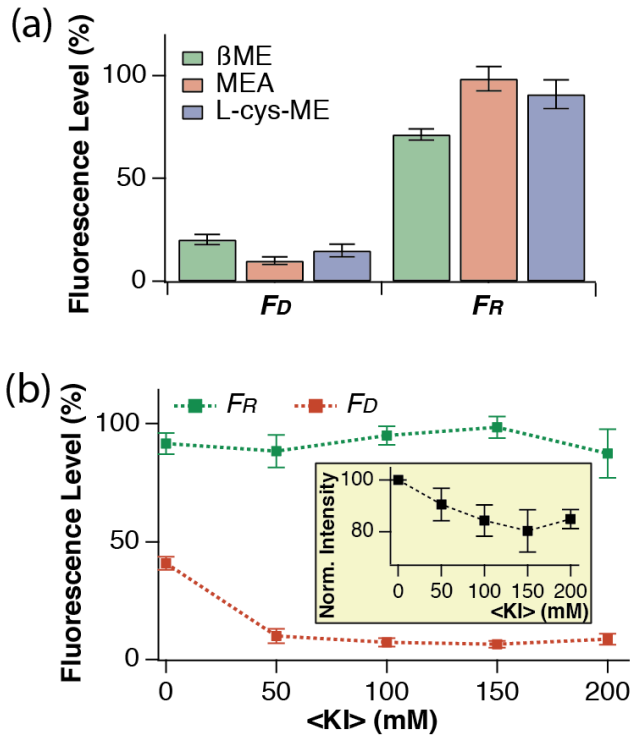

Fig. 2.10 (a) Effect of primary thiols (with 50 mM KI) on the switching characteristics of the Cy3-Alexa647 heterodimer. (b) The residual fluorescence intensity and activation rate against KI concentration in 143 mM MEA solution. Inset shows the increasingly decaying effect of KI on the fluorescence intensity. (Error bars: standard deviations.)

Potassium iodide (KI) is another crucial element to improve the transition cross section, as the iodide increases the inter-system crossing rate by the heavy atom induced spin-orbit coupling.[31] Previous research found that the photoinduced adduct formation can be accelerated upon increasing the iodide concentration,[25] suggesting that the reaction pathway involves the triplet state. The fact that KI decreases F_D substantially while keeping F_R at around 100 % (Fig. 2.10b) indicates that it increases the transition cross section of the heterodimer but little affects both the photoactivation cross section and the photobleaching quantum yield. Unfortunately, KI also decreases the fluorescence intensity of the 'bright' state molecules due to a high population in the triplet state (Fig. 2.10b, inset).

Considering all these effects on the fluorescence intensity and depletion rate, we chose a KI concentration of 100 mM for further experiments.

2.4.3. Determination of the Optical Imaging Conditions

Following the optimization of the imaging buffer conditions, we tried to optimize the photon flux by controlling the depletion and activation pulses. Since the pulse duration and peak intensity vary inversely for a constant photon flux, we fixed the pulse duration and changed the peak intensity to control the photon flux for experimental convenience. Because the pulse duration is the most critical factor for the total image acquisition time, it is desirable to minimize the pulse duration without causing significant photobleaching. Considering all these factors, we used depletion and activation pulses of 15 and 0.5 ms duration, respectively.

In order to investigate the effect of depletion power, P_{dep}, on photoswitching, we measured F_D as we varied P_{dep} while keeping the activation power, P_{act}, at a constant level (Fig. 2.11a). With only 5 μW of P_{dep}, F_D was depleted below 10%, which is a much lower depletion power than used in STED but comparable to that in GSD. Without photoactivation, the thermal lifetime of the dark state is of the order of hours,[25] which results in nearly complete depletion below 2% with higher P_{dep}. Exponential fitting of the depletion curve yielded a saturation power, P_{sat}, of 0.56 μW (Fig. 2.11a, red line), which amounts to 0.32 kW/cm^2 and is a typical value of laser power needed to turn off half of the fluorescence. P_{sat} also can be used to estimate the size of the effective focal point, $x \approx \lambda/[2NA\times\sqrt{1 + I_{max}/I_{sat}}$, where I_{max} and I_{sat} indicate the applied depletion intensity and the saturation intensity, respectively. This equation is generally expressed in terms of I_{max}/I_{sat}, but a scaling factor can be used to turn it in terms of P_{max}/P_{sat}. Based on the above equation, it is readily estimated that our proposed experimental scheme should easily achieve > 4-fold enhancement in lateral resolution with P_{dep} less than ~10 μW. In our tested range of P_{dep} (≤ 60 μW), FR stayed at a constant level with little fluctuations (Fig. 2.11a, dotted green line), which indicates that the depleting

photon flux does not affect the activation process and do not induce significant photobleaching in this power range.

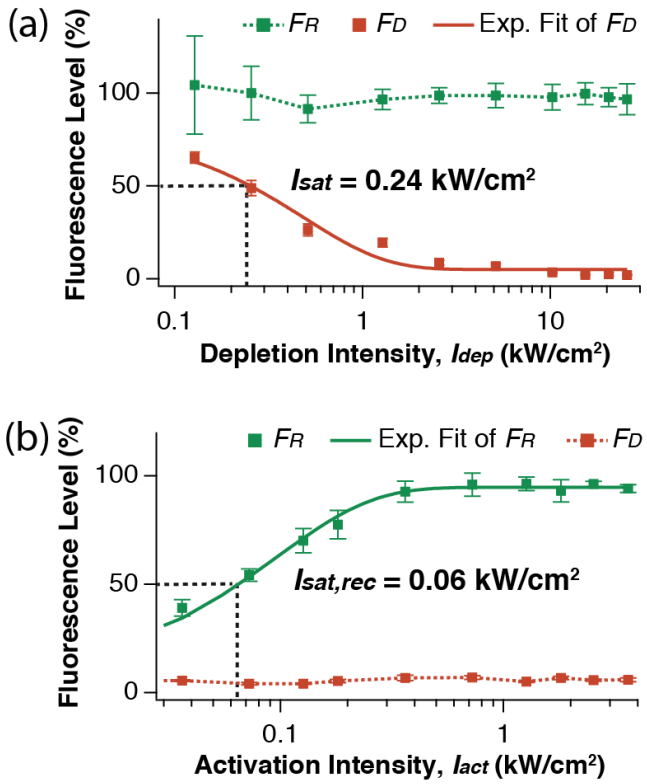

Fig. 2.11 Effect of photon power on the depletion (a, red markers) and the activation (b, green markers) of fluorescence. Exponential fitting (solid red curve for a and solid green curve for b) yields P_{sat} = 0.56 μW and $P_{sat,rec}$ = 0.10 μW, respectively. In contrast, the corresponding opposite process remains virtually constant (green markers and green dotted curve for (a) and red markers and red dotted curve for (b)). (Error bars: standard deviations.)

Optimization of P_{act} is also important to acquire high-resolution images because without perfect activation, a considerable amount of fluorescence signal would be lost due to the 'dark' fluorophores in the reduced focal volume. Moreover, excess activating photon flux tends to greatly facilitate photobleaching of the reporter through diverse pathways due to the fluorescence resonance energy transfer and the photons having relatively higher energy.[32] Figure 2.11b shows that at P_{dep} of 11.4 μW, F_R increases with Pact in the lower range of power (< 1 μW), suggesting that the activating photon flux was not saturated in this range. In the higher range

of power (up to 6 μW as tested), we see a nearly perfect photoactivation efficiency of greater than 95% without severe photobleaching. The result was well fitted by an exponential function that yielded a saturation power of 0.10 μW for the activation process (Fig. 2.11b, green line). Again, F_D stayed constant at the initial level in the tested Pact range, indicating that the activating photon flux is completely decoupled from the depletion process (Fig. 2.11b, dotted red line).

2.4.4. RESOLFT Imaging of Cy3-Alexa647 Labeled Microtubules in a Fixed HeLa Cell

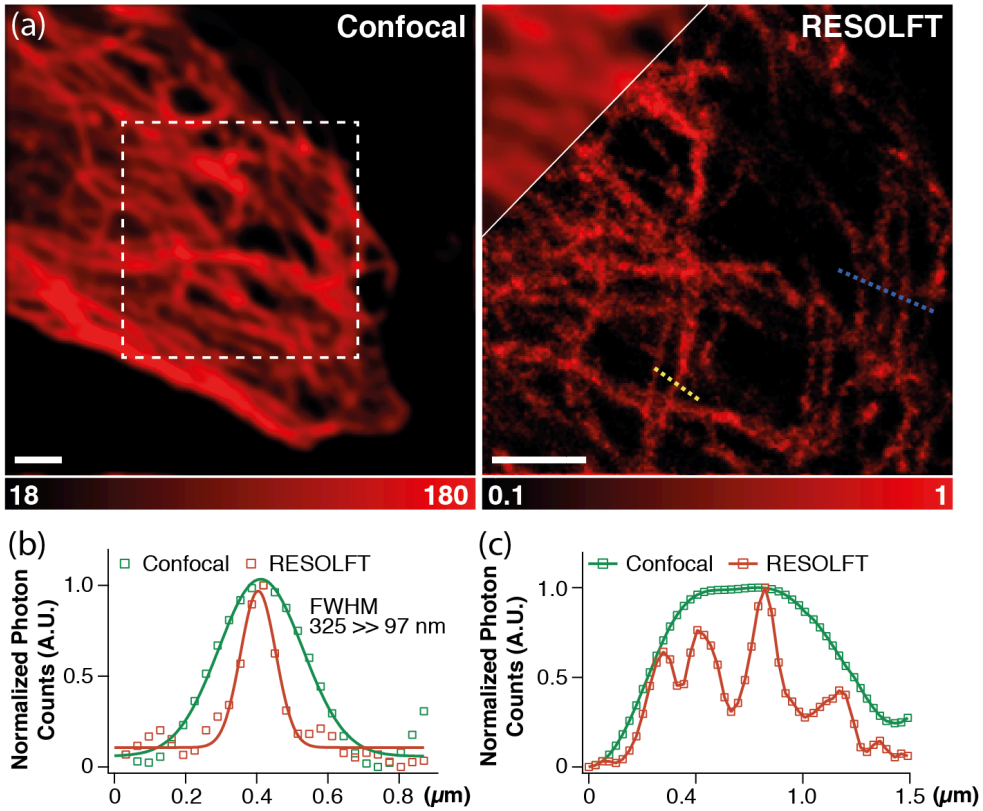

Fig. 2.12 (a) Wide-view confocal (left) and narrow-view RESOLFT (right) images of microtubules in a fixed HeLa cell stained with the Cy3-Alexa647 heterodimer. Scale bar: 2 μm. (b) Fluorescence line profiles of a microtubule by confocal (green) vs. RESOLFT (red) image along the white dotted line (a), showing a drastic improvement of spatial resolution by RESOLFT by a factor of 3. (c) Fluorescence line profiles of confocal (green) vs. RESOLFT (red) image along the blue dotted line in (a), showing that the single tubule-like structure observed by confocal imaging turns out to be several strands of nearby tubules by RESOLFT imaging.

Finally, we demonstrated the feasibility of RESOLFT imaging of microtubules labeled by the covalently-linked Cy3-Alexa647 heterodimer in a fixed HeLa cell. We applied three pulses that are comprised of activation (0.5 ms, 2.9 μW), depletion (15 ms, 13.1 μW), and probe (0.5 ms, 5.7 μW) pulses in a pump-probe manner with the probe pulse used to visualize the RESOLFT image. We used the imaging buffer containing 143 mM of MEA and 100 mM of KI to ensure the lowest FD of ~5% and FR greater than 95% without severe photobleaching.

Figure 2.12a compares the wide-view confocal (left) and narrow-view RESOLFT (right) images of the microtubules in a fixed cell (RESOLFT image was obtained for the marked region with the white dotted square). The experimental FWHM of our RESOLFT image was determined by fitting the line profile of single microtubule with a Gaussian function (Fig 2.12a, yellow dotted line). After considering some artifacts such as the size of the microtubule and the antibodies, we obtained a FWHM of 97 nm for our RESOLFT image, which is about one third of that obtained by confocal microscopy (325 nm) (Fig. 2.12b). When we averaged ten line profiles from random positions for better estimation, the FWHM of the microtubules was measured by 106 ± 14 nm for RESOLFT imaging (Fig. 2.13). Smaller FWHM also means a better resolving power that enables distinction of multiple objects in a volume smaller than the diffraction limit. We tested this effect by analyzing multiple spatially adjacent microtubules separated by ~250 nm (Fig 2.12a, blue dotted line). Confocal microscopy yielded only a blurred image of one thick fiber, but RESOLFT nanoscopy is seen to clearly resolve it into the image of several nearby fibers. Figure 2.12c also showed clearly distinguished line profiles for the RESOLFT nanoscopy, whereas the confocal microscopy can never give detail structures.

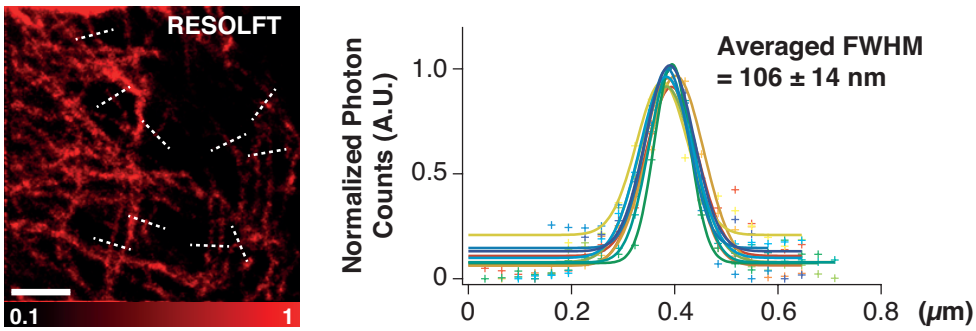

Fig. 2.13 Fluorescence line profiles of ten randomly selected positions (white dotted lines) from RESOLFT image (Scale bar: 2 μm). The raw profiles shown by '+' symbols and the corresponding Gaussian fits are color-coded.

We note, however, that our resolution is not as high as can be expected from our pump-probe measurements due to a high extent of photobleaching. It is well known that Alexa647 is photobleached after ~50 switching cycles in aqueous buffer,[33] and, even in our optimized imaging buffer, smaller pixel size (< 32 nm) may induce rather severe bleaching due to the excessively large number of switching cycles required for fulfilling Nyquist criterion. With more powerful reagents suppressing photobleaching, our method has a good prospect of offering even better spatial resolution with low operating power.

2.5. Conclusion

In conclusion, we successfully introduced the covalently-linked photoswitchable heterodimer Cy3-Alexa647 into RESOLFT nanoscopy in aqueous buffer. We optimized the buffer conditions by pump-probe fluorescence measurements and demonstrated the feasibility of our method by taking a super-resolution imaging of microtubules in the fixed HeLa cell immunostained by the Cy3-Alexa647 heterodimer. This method will open a new, efficient way to achieve sub-diffraction imaging with commonly used organic fluorophores and low power lasers, which will greatly extend its applicability in bioimaging.

2.6. References

1. S. W. Hell and J. Wichmann, *Opt. Lett.* **19**, 780 (1994).
2. S. W. Hell and M. Kroug, *Appl. Phys. B* **60**, 495 (1995).
3. E. Betzig, *Opt. Lett.* **20**, 237 (1995).
4. S. W. Hell, *Nat. Methods* **6**, 24 (2009).
5. M. J. Rust et al., *Nat. Methods* **3**, 793 (2006).
6. E. Betzig et al., *Science* **313**, 1642 (2006).
7. S. T. Hess et al., *Biophys. J.* **91**, 4258 (2006).
8. J. Fölling et al., *Nat. Methods* **5**, 943 (2008).
9. T. A. Klar and S. W. Hell, *Opt. Lett.* **24**, 954 (1998).
10. S. Bretschneider et al., *Phys. Rev. Lett.* **98**, 218103 (2007).
11. S. W. Hell et al., *Appl. Phys. A* **77**, 859 (2003).
12. S. W. Hell, *Phys. Lett. A* **326**, 2004).
13. M. Hofmann et al., *Proc. Natl. Acad. Sci.* **102**, 17565 (2005).
14. D. M. Shcherbakova et al., *Annu. Rev. Biophys.* **43**, 303 (2014).
15. T. Grotjohann et al., *Nature* **478**, 204 (2011).
16. T. Grotjohann et al., *eLife* **1**, e00248 (2012).
17. N. A. Jensen et al., *ChemPhysChem* **15**, 756 (2014).
18. I. Testa et al., *Neuron* **75**, 992 (2012).
19. I. Testa et al., *Nano Lett.* **105**, 103 (2015).
20. F. L.-Cardinal et al., *ChemPhysChem* **15**, 655 (2014).
21. T. Schmidt et al., *Single Mol.* **3**, 327 (2002).
22. M. F.-Suárez and A. Y. Ting, *Nat. Rev. Mol. Cell. Biol.* **9**, 929 (2008).
23. G. Patterson et al., *Annu. Rev. Phys. Chem.* **61**, 345 (2010).
24. M. L. Bossi et al., *New J. Phys.* **8**, 275 (2006).
25. M. Bates et al., *Phys. Rev. Lett.* **94**, 108101 (2005).

26. M. Heilemann et al., *J. Am. Chem. Soc.* **127**, 3801 (2005).

27. G. T. Dempsey et al, *J. Am. Chem. Soc.* **131**, 18192 (2009).

28. B. Huang et al., *Nat. Methods* **5**, 1047 (2008).

29. N. R. Conley et al., *J. Phys. Chem. B* **112**, 11878 (2008).

30. I. Rasnik et al., *Nat. Methods* **3**, 891 (2006).

31. J. Widengren and P. Schwille, *J. Phys. Chem.* **104**, 6416 (2000).

32. X. Kong et al., *J. Am. Chem. Soc.* **129**, 4643 (2007).

33. G. T. Dempsey et al., *Nat. Methods* **8**, 1027 (2011).

Chapter 3.

A New Sub-diffraction-limit Microscopy Technique: Dual-point Illumination AND-gate Microscopy on Nanodiamonds (DIAMOND)

3.1. Introduction

Far-field fluorescence microscopy is widely used in biology as a vital tool to image the interior of living cells, often with molecular specificity. However, the spatial resolution of an optical microscope is severely constrained by the diffraction limit of visible light[1], which makes it difficult to directly observe the structures of biomolecules and their interactions. In order to overcome the diffraction limit, sub-diffraction-limit optical microscopy techniques have been introduced in the last two decades and improved the spatial resolution at least by an order of magnitude.

Two distinct kinds of technique are employed to enhance the spatial resolution: one based on reducing the effective point spread function (PSF) and the other attempting localization of single fluorophores. The first method uses spatially defined population depletion of a bright state, a concept generally called reversible saturable optical fluorescence transition (RESOLFT)[2], which includes stimulated emission depletion microscopy[3], ground state depletion microscopy[4], and saturated structured illumination microscopy[5]. Since the spatial resolution of these techniques varies as the square root of the intensity of the depletion laser, RESOLFT microscopy can achieve super-resolution often at the expense of considerable damage to living cells and photobleaching of the fluorophores.

The second method uses stochastic localization of a single fluorophore to distinguish it from surrounding fluorophores and subsequent reconstruction of the final image using their locations. This method requires photoswitchable fluorophores such as Cy5 in stochastic optical reconstruction microscopy[6] or photoswitchable green fluorescent proteins in (fluorescence) photoactivation localization microscopy.[7,8] Since the accuracy of localization depends on the number of collected photons,[9] it often takes a long image acquisition time to achieve imaging in high spatial resolution. Both of these super-resolution microscopy techniques enable three dimensional,[10-12] multicolor[13-15] imaging of living cells[16-19], and thus have played a crucial role in elucidating biological problems that would have been otherwise impossible with diffraction-limited confocal microscopy. Despite these unique advantages, however, sub-diffraction-limit microscopy is still not widely used in investigating biological problems because of its technical complexity, pseudo-invasive nature of imaging conditions to living cells, and poor temporal resolution in comparison with typical cellular processes.

Here we introduce a new, easily implementable sub-diffraction-limit microscopy technique that utilizes the optical AND-gate property of fluorescent nanodiamond (FND). We propose a new method to overcome the diffraction limit of far-field fluorescence microscope by using the AND-gate property of FND. This method can be easily implemented for bioimaging and provide enhanced spatial resolution while keeping the advantages of confocal microscopy.

3.2. Concept

3.2.1. Fluorescent Nanodiamond (FND)

FND is a nanometer-size diamond grain containing color centers that consist of an impregnated nitrogen atom and a neighboring, negatively charged vacancy defect

(called nitrogen-vacancy center or NV^- center) (Fig. 3.1a).[20-22] FND has strong optical absorption centered at 560 nm due to its transition from the ground state (^3A) to an excited state (^3E), which has a broad emission band from 600 to 850 nm with a lifetime of 11.6 ns.

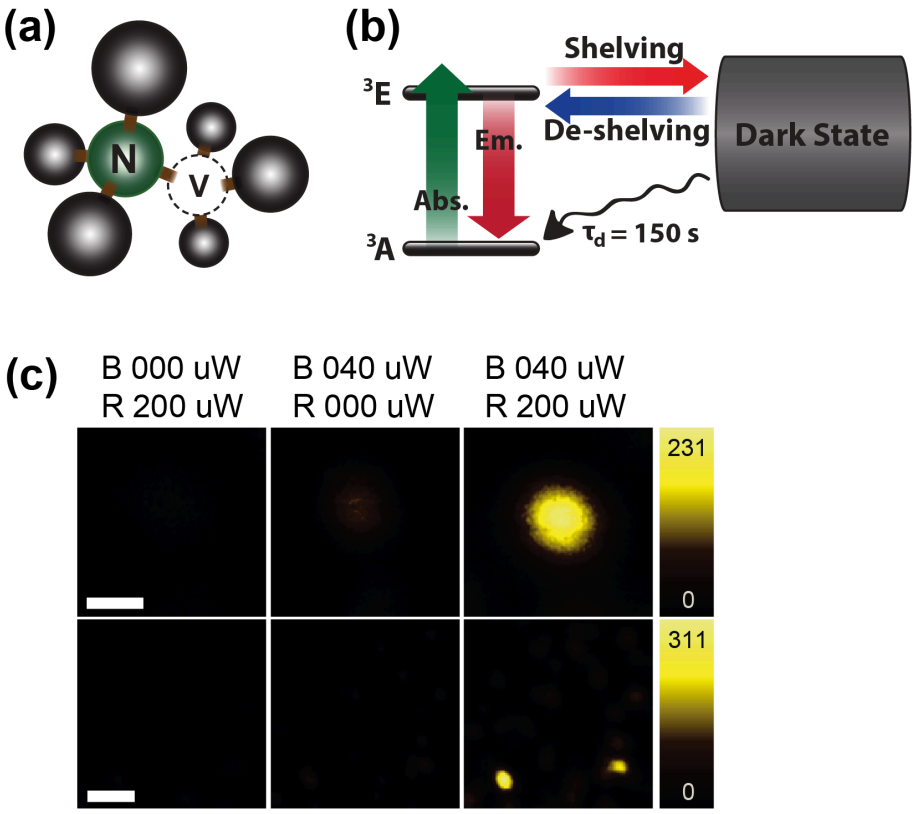

Fig. 3.1 (a) Crystal structure of NV^- center in FND. (b) Energy diagram of NV^- center with relevant electronic transitions. (c) All-optically controlled AND-gate property of NV- center under continuous illumination of 473-nm and 640-nm lasers. Scale bars: 300 nm (upper images), 1 μm (lower images).

A notable optical property of NV^- center is its photo-stability with no photobleaching and little or no photoblinking. Another important feature of FND, which is of particular value for our technique, is its all-optically controlled photo-switching behavior (Fig. 3.1b).[23] Illuminating the NV^- center with a red light at 638 nm excites it first to a bright, luminescent state then causes a transition (in a process called "shelving") from the bright state to a dark state that persists with a lifetime of τ_d = 150 s, whereas a blue light at 473 nm induces a reverse transition

("de-shelving"). Both shelving and de-shelving processes occur in the sub-microsecond time scale with no photobleaching and little or no photoblinking for over 800 seconds. Since the absorption cross section of FND is very small at 473 nm, the fluorescence intensity from NV^- center under continuous 473 nm illumination is maintained at low level. Modulating one of the two beams modulates the emission intensity and clearly demonstrates that FND functions as an optical AND-gate, yielding significant light emission only when illuminated by both the blue and red lights simultaneously (Fig. 3.1c).

3.2.1. Dual-point Illumination

Our strategy for achieving sub-diffraction-limit spatial resolution is to reduce the effective PSF by spatially confining the emission from FND by illuminating it with two spatially-offset lights of different wavelengths for shelving and de-shelving, which leads to light emission only from the region of their overlap because of the optical AND-gate property of FND. A similar approach has been proposed by Sakai and Fujii using transient time-resolved IR spectroscopy based on two-color IR-UV/Vis double resonance spectroscopy.[24,25] The resonant IR light induces a vibrational transition and only the vibrationally excited molecule can absorb the UV/Vis light, yielding a transient fluorescence signal. In this scheme, fluorescence comes only from the region of overlap between the IR and UV/Vis lights, which is smaller than the diffraction limit of the IR light, but not of the UV/Vis light.

Our new method, named "dual-point illumination AND-gate microscopy on fluorescent nanodiamond" (DIAMOND in acronym), can readily reduce the effective PSF below the diffraction limit of visible light. If we were to apply dual-point illumination to a typical fluorescent dye in the scheme of Figure 3.2a, fluorescence will result from all regions illuminated by either light, yielding a PSF in the shape of a dumbbell lying sideways. If, on the other hand, we adopt an optical AND-gate material such as FND, fluorescence will come only from the region of overlap between the two spatially-offset lights, resulting in an oval-

shaped PSF with a greatly reduced lateral dimension. With this concept, one can easily achieve sub-diffraction-limited spatial resolution based on scanning optical microscope, without using a complex optical arrangement.

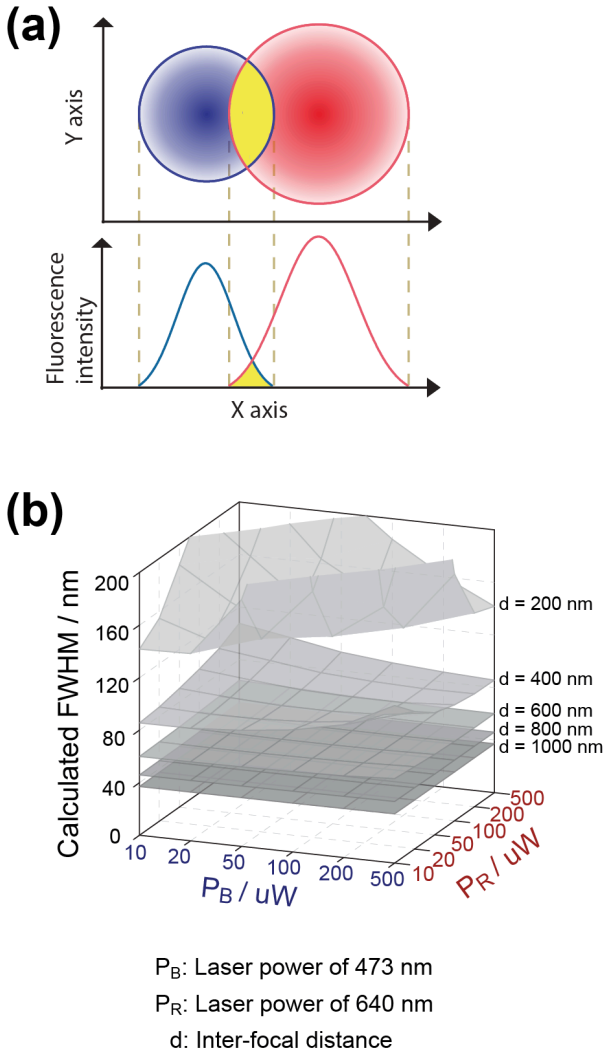

Fig. 3.2 (a) Schematic diagram for dual-point illumination scheme. When an optical AND-gate material is illuminated by two spatially-offset lights of different wavelengths, emission comes only from the region of their overlap. (b) Calculated size (FWHM) of the spatial overlap (yellow region in (a)) under various conditions of laser power and inter-focal distance, assuming a Gaussian-like profile for the PSF. Laser power does not significantly affect the FWHM, whereas the inter-focal distance exerts a much greater effect on the FWHM.

The full-width at half maximum (FWHM) of spatial overlap can be estimated by a simple calculation, assuming Gaussian-like profiles for each laser focal spot described as below.

$$PSF_b = \left(\frac{2P_b}{F_b}\right)\left(\frac{ln2}{\pi}\right)^{\frac{1}{2}} \exp\left\{-\frac{(4ln2)x^2}{F_b^2}\right\}$$

$$PSF_r = \left(\frac{2P_r}{F_r}\right)\left(\frac{ln2}{\pi}\right)^{\frac{1}{2}} \exp\left\{-\frac{(4ln2)(x-d)^2}{F_r^2}\right\}$$

Here, P and F are respectively the laser power and FWHM of each laser (b for blue and r for red) and d is the inter-focal distance. We used an FWHM of 240 nm for the blue laser (473 nm) and 320 nm for the red laser (633 nm). The position of overlapped intensity maximum, x_c, is a point of intersection and can be calculated as $x_c = -kd + \sqrt{\frac{kF_r^2}{4ln2}\ln\left(\frac{F_rP_b}{F_bP_r}\right) + kd^2 + (kd)^2}$, where k is $\frac{F_b^2}{F_r^2 - F_b^2}$. The exact numerical value of maximum intensity can be calculated by using $PSF_b(x_c)$ and $PSF_r(x_c)$, and they have to give the same result, PSF_{max}. The FWHM can be determined by using the inverse functions of PSF_b and PSF_r, PSF_b^{-1} and PSF_r^{-1}, and the half of its maximum intensity, $\frac{PSF_{max}}{2}$. Because we use the positive inter-focal distances for the calculations, the FWHM should be the difference between the rising edge of PSF_r^{-1} and falling edge of PSF_b^{-1}, which is described as below.

$$\text{FWHM} = PSF_r^{-1}\left(\frac{PSF_{max}}{2}\right) - PSF_b^{-1}\left(\frac{PSF_{max}}{2}\right)$$

In this case, the spatial offset, i.e., the distance between the two illumination focal points, governs the FWHM of the effective PSF, leading to higher spatial resolution at larger spatial offset for an ideal AND-gate fluorophore and a Gaussian-like PSF of microscope (Fig. 3.2b).

Since the increase in laser intensity has no apparent merit for spatial resolution in DIAMOND, this new method is well-suited for in vivo samples that require mild, non-invasive imaging conditions. The DIAMOND technique is entirely confocal-based and thus inherits all the advantages of confocal microscopy, not the least of which is its simplicity. Therefore, one can achieve sub-diffraction-limit spatial

resolution in a quick, easy, convenient, and inexpensive way with no technical complexities often encountered in other such methods.

3.3. Experimental Detail

3.3.1. Sample Preparation

FND samples of 30 and 140 nm diameters were obtained from the Huan-Cheng Chang group of the Institute of Atomic and Molecular Sciences, Taiwan, and placed on the surface of a cover glass. Immobilization of FND was performed using the electrostatic interaction between poly-L-lysine (P8920, *Sigma-Aldrich*) and the carboxyl group on the surface of FND. The cover glass (BB024024A1, *Menzel-Gläser*) was washed with methanol (A452-4, *Fisher Scientific*), acetone (A949-4, *Fisher Scientific*), and deionized (DI) water and dried with nitrogen gas. 10 μL of poly-L-lysine was incubated on the surface of the cover glass for 3 minutes and washed with DI water following nitrogen gas drying. 10 μL of FND sample went through the same incubation and washing processes. An immersion oil (10976, *Fluka*) was used as a mounting medium between cover glass and slide glass (12-544-2, *Fisher Scientific*) to match the refractive index with the microscope.

The PSF of each focused laser spot and the distance between the two spatially-offset lights were measured by using a sample of 80-nm gold beads (EM.GC80, *BB International*), which were immobilized on the surface of a cover glass using their electrostatic interaction with poly-L-lysine. The immersion oil was used as a mounting medium. An identical preparation method was employed for the gold beads with that for the FND sample.

3.3.2. DIAMOND Setup

A home-built fluorescence confocal microscopy system was used to demonstrate the DIAMOND concept (Fig. 3.3). Lights from three continuous-wave excitation lasers (473 nm: 35-LAP-321, *CVI Melles-Griot*; 532 nm: Samba^{TM} 532, *Cobolt*; 640 nm: TECRL-25G-635, *World Star Tech*) were transmitted through a single-mode fiber (Φ = 3 – 5 μm, P1-488-PM-FC and P1-630PM-FC, *Thorlabs*) coupling, and combined through dichroic mirrors (Z473rdc, Z532rdc and Z647rdc, *Chroma*). Lasers were circularly polarized using achromatic $\lambda/4$ and $\lambda/2$ retarders (RAC 3.4.15, RAC 3.2.15 and RAC 4.2.15, *Bernhard Halle Nachfl.*) to efficiently illuminate the sample through an oil-immersion objective (NA 1.45, 60x, f = 3 mm, *Olimpus*). The sample was placed on a piezo-electric scanning system (Nanomax Max311, *Thorlabs*) with its own controller (BPC203, *Thorlabs*) to scan the imaging area with 5 nm accuracy. The fluorescence signal from FND was filtered through an emission filter (HQ700/75m, *Chroma*) and detected by an avalanche photodiode (SPCM-AQR-14FC, *Perkin Elmer*) through a multi-mode fiber (Φ = 62.5 μm, M31L02, *Thorlabs*) to enhance the signal-to-background (S/B) ratio, as does a pinhole in a confocal microscope. The detection window was allowed to span a tightly confined region of the intersection by this multi-mode fiber and detection lens (f = 1000 mm) to reduce the background from out of the intersection region. We used a multi-channel analyzer (P7882 photon counter, *Fast ComTec*) to convert the analogue signal to photon counts, which were then visualized by an imaging program, Imspector. All measurements were performed on 128x128 pixels covering various imaging areas, which are shown in each figure by a scale bar.

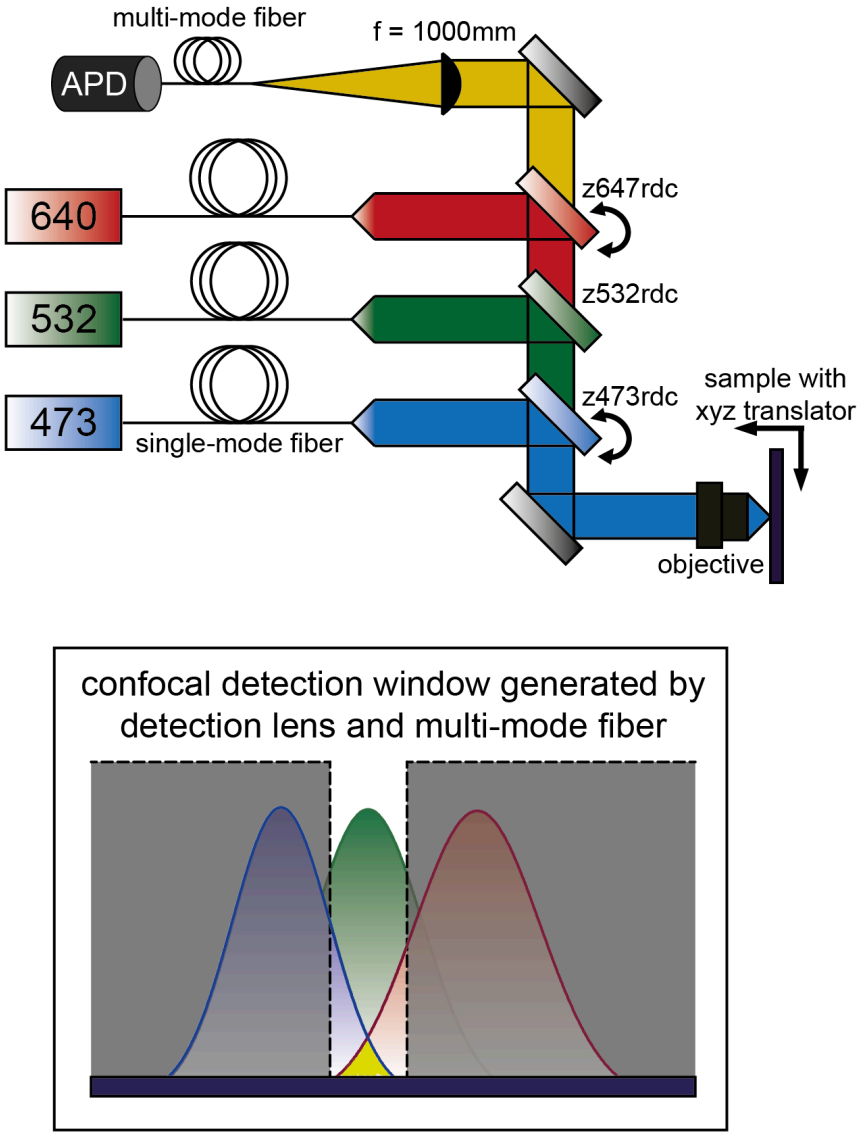

Fig. 3.3 Home-built sub-diffraction-limit microscopy system for DIAMOND. The position of focal points is controlled by adjusting the dichroic mirrors. (below) Schematic diagram of the detection window for the DIAMOND technique. The detection window is tightly defined by the overlap of the two spatially offset beams using a detection lens (f = 1000 mm) and a multi-mode fiber (Φ = 62.5 μm).

A key factor for DIAMOND in achieving the sub-diffraction-limit resolution is to enable precise spatial control of the illumination lasers. Two dichroic mirrors that reflect the 640-nm and 473-nm lasers were used to accomplish such a goal. By carefully adjusting the reflection angle of the dichroic mirrors, we were able to

control the focal positions of the lasers to result in a spatial overlap with an arbitrary distance between the two focal points. The spatial offset and the PSF were identified by observing the scattered light from an 80-nm gold bead sample, which was detected by photomultiplier tube without multi-mode fiber coupling to clearly display the PSF at various values of spatial offset. We then observed the FND samples by confocal microscopy (532 nm) and DIAMOND (473 nm and 640 nm) using a tightly defined detection window to enhance the S/B ratio by reducing the fluorescence from out of the intersection region.

3.4. Result and Discussion

3.4.1. DIAMOND with 140-nm FND Sample

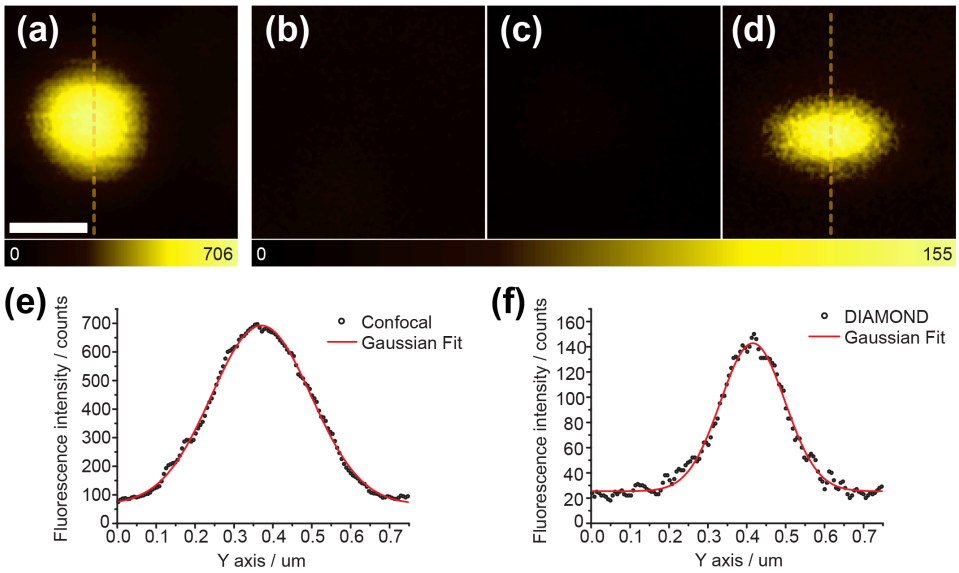

Fig. 3.4 (a) Fluorescence confocal microscopy image of a 140-nm FND particle (excitation wavelength = 532 nm). DIAMOND images of the same FND particle excited by (b) only the shelving light at 640 nm, (c) only the de-shelving light at 473 nm, and (d) the AND-gate lights at 640 nm and 473 nm. (e, f) The cross sectional line profiles (black circles) along the yellow dashed lines in (a) and (d) with their Gaussian fits (red lines). Scale bar: 250 nm.

In order to demonstrate the feasibility of DIAMOND, we investigated whether the effective PSF is actually reduced using FNDs of different sizes. Since the position

of the two focal points can be controlled in the imaging plane in both the x- and y-directions by adjusting dichroic mirrors, we can choose to have the spatial offset along one of the axes, in which case the effective PSF shrinks along that axis but not along the other axis (Fig. 3.4d). The resulting PSF is an oval shape, whose short axis can be further reduced by increasing the spatial offset. The DIAMOND images shown in Fig. 3.4 (and those in subsequent figures) were obtained by continuously illuminating the two spatially-offset focal points with blue (473 nm, 40 μW) and red (640 nm, 3 mW) lasers, while the confocal microscopy images were taken by continuous green (532 nm, 160 μW) illumination. Since the NV^- center is not an ideal AND-gate and thus emits weak fluorescence under blue or red illumination, these spurious signals contribute to the background and cause mild blurring of the image. We can readily subtract these spurious signals to improve the S/B ratio.

Figure 3.4 shows that the effective PSF measured from single 140-nm FND is clearly reduced along one axis as we go from regular confocal microscopy (Fig. 3.4a) to DIAMOND (Fig. 3.4d). At the wavelength of confocal microscopy (532 nm), shelving and de-shelving processes occur simultaneously to result in a strong fluorescence emission. When we employ the DIAMOND scheme but use only the 640-nm light, shelving of the excited population to the dark state greatly reduces the fluorescence intensity to the level of background signal (Fig. 3.4b). On the other hand, when we use only the 473-nm light, de-shelving from the dark state can keep a significant population in the bright state, but the absorption cross section at this wavelength is so small in the first place that we have little fluorescence intensity (Fig. 3.4c). Finally, using both the 640-nm and 473-nm lights induces optical AND-gate emission from the region of their spatial overlap, yielding a typical DIAMOND image with an oval-shaped PSF (Fig. 3.4d). The intensity profiles also show that the FWHM of confocal PSF (302 nm, measured along the yellow dashed line) is significantly reduced to a sub-diffraction-limit value (195 nm) with DIAMOND (Fig. 3.4e and 3.4f).

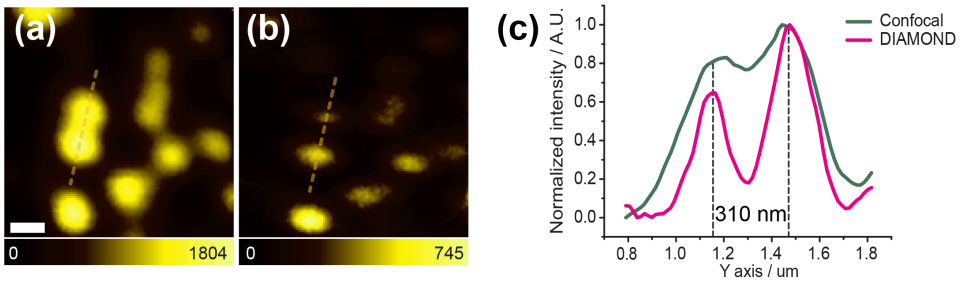

Fig. 3.5 (a,b) A wider view of the 140-nm FND sample. DIAMOND gives no missing or spurious additional image against confocal microscopy. All particles are shown to have a reduced effective PSF along the same axis. (c) The fluorescence intensity line profiles along the yellow dashed lines in (a) and (b). Scale bar: 300 nm.

The enhanced resolving power also allows unambiguous, discrete imaging of multiple particles in close proximity. For example, the particles along the yellow dashed lines of Figure 3.5a and 3.5b are not totally distinguishable by confocal microscopy, but we can readily verify that they consist of two particles at a clear separation by DIAMOND imaging (Fig. 3.5c). In addition, all particles detected by confocal microscopy are also faithfully observed in DIAMOND without any missing or spurious additional images.

3.4.2. DIAMOND with 30-nm FND Sample

The effective PSF can be further reduced if we employ smaller fluorescent particles. Figure 3.6a and 3.6b show the confocal and DIAMOND images of 30-nm FND single particle showing that the effective PSF of DIAMOND is 133 nm (FWHM), which is much smaller than that of confocal microscopy, 301 nm, and obviously under the diffraction limit (Fig. 3.6e and 3.6f). Such an enhanced PSF enables distinction of two adjacent FND particles (Fig. 3.6d and 3.6g, at a separation of 280 nm), even when the fluorescence signal of one particle is much smaller than that of the other. In contrast, confocal microscopy gives only a blurred image and we cannot even figure out how many particles exist in the area (Fig. 3.6c).

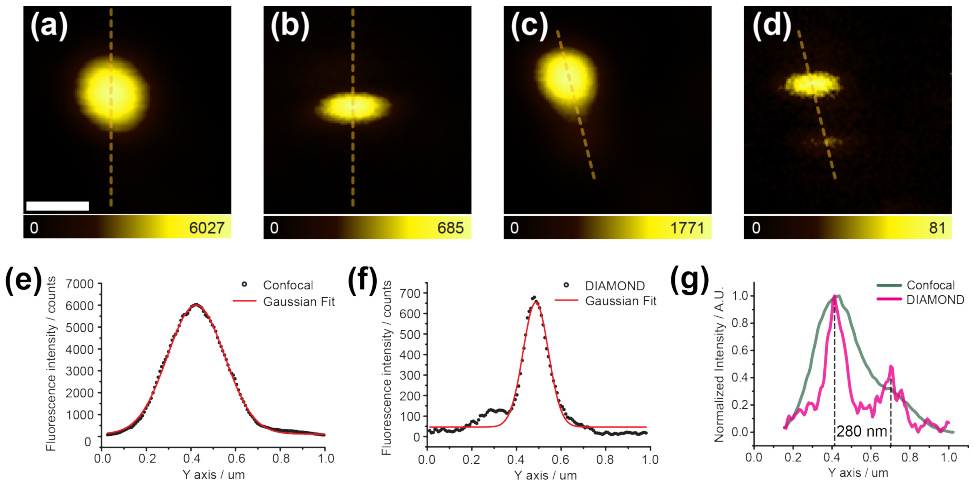

Fig. 3.6 Confocal vs. DIAMOND images of a 30-nm FND sample with their respective intensity profiles. (a,b) Effective PSF measured for a single 30-nm FND particle, which is shown to give much sharper imaging than with 140-nm FND. (c,d) Two adjacent FND particles separated by 280 nm appear as a single particle by confocal microscopy but are clearly resolved by DIAMOND imaging. (e, f) The fluorescence intensity line profiles (black circles) along the yellow dashed lines in (a) and (b) with their Gaussian fits (red lines). (g) The fluorescence intensity line profiles along the yellow dashed lines in (c) and (d). Scale bar: 300 nm.

3.4.3. 2D-DIAMOND for Symmetric Image

Although DIAMOND offers many advantages such as instrumental simplicity and low demand for laser power over other sub-diffraction-limit microscopy techniques, the drawback for DIAMOND so far is its oval-shaped effective PSF due to the one-dimensional resolution enhancement that causes image distortion of the sample. In order to overcome this problem, we introduce 2D-DIAMOND imaging that gives a symmetric effective PSF (Fig. 3.7a and 3.7b) by convoluting two independent DIAMOND images obtained along two perpendicular axes (Fig. 3.7c and 3.7d). It is straightforward to control the offset direction of the focal points by simply adjusting the mirror mounts. The emitted photon count at a pixel in one offset was saved and compared with that of the other offset in the perpendicular direction, and the smaller photon count was selected to generate a new image, which is now symmetric. Since the fluorescence signal from FND is sufficiently larger than the thermal noise, signals can be distinguished from the background when we select

the lower photon count, which means that this process does not allow missing any fluorescent particle, if we were to accept a lower S/B ratio. The experimentally measured effective PSF of 2D-DIAMOND with 30-nm FND has a FWHM of 154 nm in one direction and 159 nm in the other (Fig. 3.7e and 3.7f). As already mentioned, since our data processing protocol is optimized at not missing a fluorescent particle at the expense of a lower S/B ratio, these values are slightly larger than the FWHM of the effective PSF in 1D-DIAMOND images.

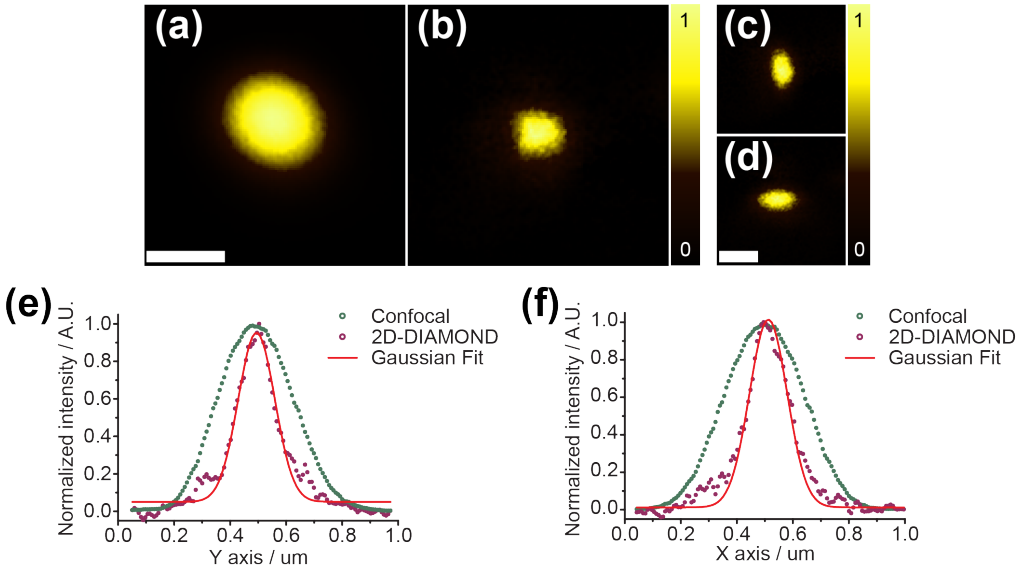

Fig. 3.7 Confocal (a) vs. 2D-DIAMOND (b) images of a 30-nm FND sample, the latter from comparative discrimination of two 1D-DIAMOND images obtained in perpendicular directions (c,d). (e,f) Intensity profiles of confocal microscopy vs. 2D-DIAMOND along y-axis (e) and x-axis (f). The measured FWHMs from Gauss fit are 314 nm (x axis) and 337 nm (y axis) for confocal microscopy, whereas they are much reduced to 154 nm (x axis) and 159 nm (y axis) for 2D-DIAMOND. Scale bars: 300 nm.

Figure 3.8a and 3.8b show that 2D-DIAMOND can also provide enhanced resolving power over confocal microscopy for a sample with multiple features, which in this case is a set of adjacent FND particles lying along the y axis. Using 1D-DIAMOND with a spatial offset along the x axis (Fig 3.8c), the resolution enhancement appears only along that axis and thus the two particles remain unresolved, whereas an orthogonal spatial offset along the y axis reveals a completely resolved image for the two particles (Fig. 3.8d). For particles of any

spatial arrangements, one can employ 2D-DIAMOND to enhance spatial resolution with a symmetric effective PSF, while keeping the resolving power in both dimensions. The fluorescence intensity profiles also clearly shows the reduced effective PSF and enhanced resolving power of 2D-DIAMOND (Fig. 3.8e).

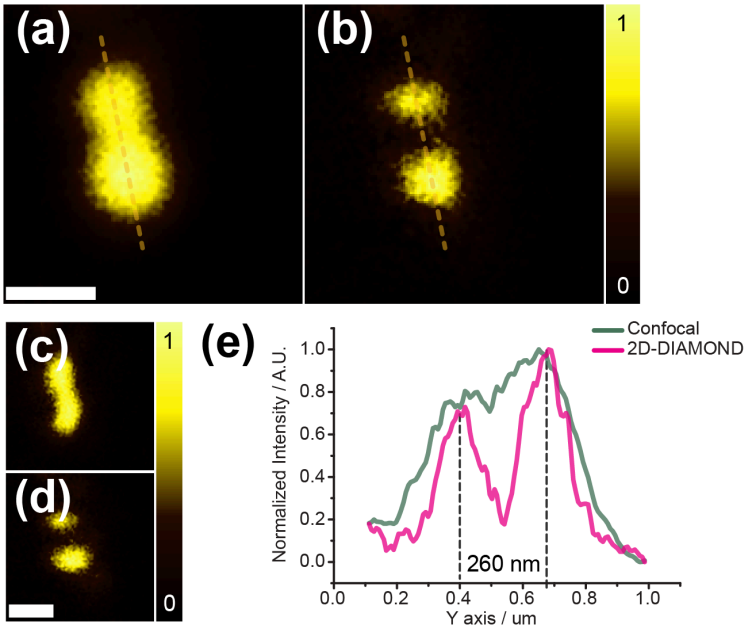

Fig. 3.8 Confocal (a) vs. 2D-DIAMOND (b) images of a 30-nm FND sample. The latter is clearly shown to differentiate two adjacent FND particles in contrast to the confocal image. (c,d) Two orthogonal 1D-DIAMOND images were used to reconstruct the symmetric 2D-DIAMOND image. (e) The fluorescence intensity profiles along the yellow dashed lines in (a) and (b). Scale bars: 300 nm.

Because we make a comparison of the fluorescence intensities at a given pixel of two 1D-DIAMOND images to generate a symmetric (i.e., circular, not oval-shaped) image, there is a possibility for a crosstalk from an off-center region during data processing. Although the fluorescence intensity due to the crosstalk should often be distinguishable because of its lower intensity than that of the fluorescent particles, the spurious signal from the crosstalk remains a challenging problem with the current 2-D scanning method.

3.5. Conclusion

In conclusion, we propose a new concept and experimental platform to overcome the diffraction limit in far-field optical microscopy by employing two laser beams with a spatial offset that illuminate an optical AND-gate material. We demonstrated its feasibility and sub-diffraction-limit nature by using different sizes of FND. With this technique, sub-diffraction-limit microscopy can be implemented in a quick, easy, convenient, and inexpensive way with no technical complexities often encountered in other methods. Furthermore, since FND is an ideal fluorescent material with high photostability, this new method may find its use in dynamic imaging over a long duration of time.

3.6. References

1. E. Abbe, *Arch. Mikrosk. Anat.* **9**, 413 (1873).
2. S. W. Hell, *Science* **316**, 1153 (2007).
3. S. W. Hell and J. Wichmann, *Opt. Lett.* **19**, 780 (1994).
4. S. W. Hell and M. Kroug, *Appl. Phys. B* **60**, 495 (1995).
5. M. G. L. Gustafsson, *Proc. Natl. Acad. Sci.* **102**, 13081 (2005).
6. M. J. Rust et al., *Nat. Methods* **3**, 793 (2006).
7. E. Betzig et al., *Science* **313**, 1642 (2006).
8. S. T. Hess et al., *Biophys. J.* **91**, 4258 (2006).
9. A. Yildiz et al., *Science* **300**, 2061 (2003).
10. R. Schmidt et al., *Nat. Methods* **5**, 539 (2008).
11. B. Huang et al., *Science* **319**, 810 (2008).
12. M. F. Juette et al., *Nat. Methods* **5**, 527 (2008).
13. G. Donnert et al., *Biophys. J.* **92**, L67 (2007).
14. M. Bates et al., *Science* **317**, 1749 (2007).

15. H. Shroff et al., *Proc. Natl. Acad. Sci.* **104**, 20308 (2007).
16. B. Hein et al., *Proc. Natl. Acad. Sci.* **105**, 14271 (2008).
17. L. M. Hirvonen et al., *Eur. Biophys. J.* **38**, 807 (2009).
18. H. Shroff et al., *Nat. Methods* **5**, 417 (2008).
19. S. A. Jones et al., *Nat. Methods* **8**, 499 (2011).
20. A. Gruber et al., *Sceicne* **276**, 2012 (1997).
21. F. Jelezko and J. Wrachtrup, *Phys. Stat. Sol. A* **203**, 32007 (2006).
22. C. C. Fu et al., *Proc. Natl. Acad. Sci.* **104**, 727 (2007).
23. K. Y. Han et al., *Nano Lett.* **10**, 3199 (2010).
24. M. Sakai et al., *Chem. Phys. Lett.* **439**, 171 (2007).
25. K. Inoue et al., *Opt. Express* **17**, 12013 (2009).

Chapter 4.

Single Molecule Detection in 100 Times Concentrated Solutions by ALEX-FRET and STED Nanoscopy

4.1. Introduction

The single molecule techniques widely used in biophysics and biochemistry to investigate the conformation change and interaction with other molecules of biomolecules.[1-4] Compared to ensemble measurements, which always have a possibility for averaging the information of individual molecules, the single molecule techniques provide the exact information of the target system.[5,6] The primary requirement of the single molecule detection is to reduce the background signals from non-target molecules such as solvent and impurities. Moreover, tiny observation volume also plays an important role to detect the single molecule in a reliable concentration range.

Technically, the confocal microscope is one of the best choices for the single molecule detection because it has diffraction limited observation volume, which is the smallest volume physically allowed, and the high signal-to-background (S/B) ratio due to the pinhole in the imaging plane. According to the Poisson distribution, it can observe the individual molecules in sub-100 pM concentration range. For the *in vitro* experiments, this limitation in concentration should be an advantage because the confocal-based single molecule technique can be applied to very small amount of samples with high sensitivity. However, for the *in vivo* measurements,

in which the biologists have much more interests, it cannot easily applied to the biological samples due to the concentration limit because many of biomolecules exist in the cell with > 1 nM concentration. Therefore, to directly observe the diffusing individual biomolecules and their interactions *in vivo*, we have to further reduce the observation volume. In this chapter, we will see the development of a new single molecule spectroscopy technique, which can observe the individual molecules in < 5 nM concentration range, 100 times higher than conventional concentration limit of single molecule technique. By utilizing the STED nanoscopy and ALEX-FRET, one of the single molecule techniques, we can successfully reduce the observation volume maintaining high S/B ratio.

4.2. Technical Backgrounds

4.2.1. ALEX-FRET

Alternating laser excitation FRET (ALEX-FRET) is one of the confocal-based single molecule techniques, which overcomes the limitation of conventional single molecule FRET experiments.[7] In order to measure the FRET efficiency, only the donor excitation is required where the both emissions from donor and acceptor have to be recorded (recall the equation for the FRET efficiency, E, in chapter 1.5.3). In this case, sometimes we can misunderstand the result due to the signals from the non-distinguishable and non-detectable molecules, which can be caused by the imperfect process of the fluorescence tagging (Fig. 4.1). In the statistic analysis for the kinetic information, which is frequently proceeded in diffusion-based FRET measurement, this misrepresented information should perturb the kinetics of molecular dynamics and interactions.

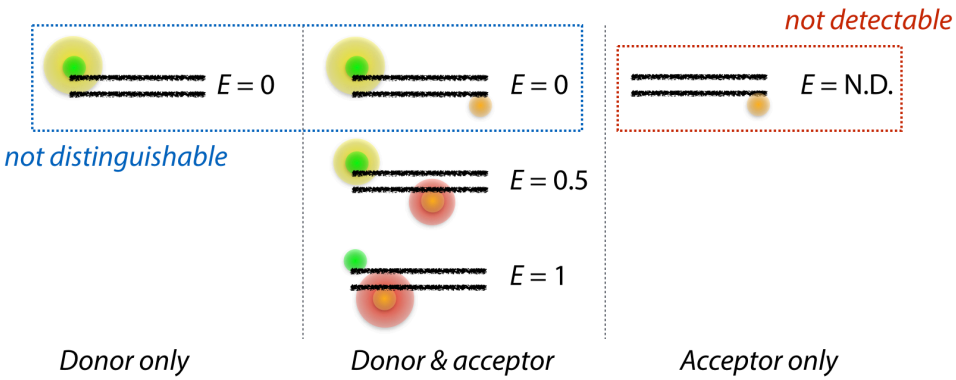

Fig. 4.1 Possible molecular compositions of a FRET pair on target structure. In conventional FRET measurement, which only excites the donor, there exist some non-distinguishable and non-detectable samples.

ALEX-FRET can efficiently prevent the measurement error by utilizing two laser sources in an alternating matter for the co-excitation of a donor and an acceptor. With alternative excitation scheme, we can introduce an additional calculated parameter, the stoichiometry value (S), to distinguish all the molecules by the chemical stoichiometry of labeled conditions. The S value is defined as $S = F_D/(F_D+F_A)$, where $F_D = F_D^D+F_D^A$ and $F_A = F_A^A$ thus F_X means the total fluorescence under X-absorbable illumination. Now we can virtually sorting the individual molecules with E and S values, and selectively analyze the molecules in interest. It is convenient to visualize the sorting result by using two-dimensional E-S histogram (Fig. 4.2). By the definition of S, the molecules labeled with only the donor appear in the area with $S = 1$, where the acceptor only labeled molecules are in the area with $S = 0$. Since the E value of latter molecules cannot be determined theoretically, they usually show a broad distribution. The molecules having both of two molecules have the S value at 0.5, and they can be also sorted by the E value that indicates their molecular structure.

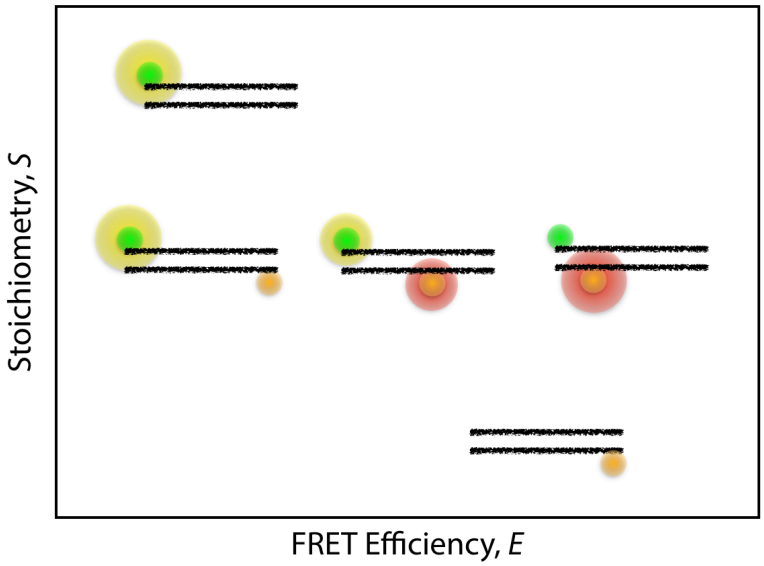

Fig. 4.2 Schematic representation of 2D E-S histogram in ALEX-FRET. All of the individual molecules having labeled conditions in Fig. 4.1 are virtually sorted by *S* and *E* values.

In the FRET measurement using two fluorophores, including ALEX-FRET, the *E* value can be perturbed by fluorescence crosstalk caused by the spectral overlap. There are two kinds of common crosstalks, the direct excitation and the fluorescence leakage. Generally the absorption spectrum of a fluorophore has a long tail in the shorter wavelength region, where the emission spectrum shows the opposite tendency. Hence the acceptor usually can absorb the donor excitation laser (direct excitation), and the emission of donor can be mixed with the emission of acceptor (fluorescence leakage). In order to accurately calculate the distance between two fluorophores by measuring FRET, these factors should be corrected by some additional experiments.[8]

Nowadays, the ALEX-FRET provides up to four inter-fluorophore distances maintaining its sorting ability.[9,10] A number of valuable researches are performed with the ALEX-FRET, such as the kinetic analysis of deoxyribozymes,[11,12] efficient detection assay for single nucleotide polymorphism[13] and the investigation on the flexibility of biomolecules.[14]

4.2.2. STED Nanoscopy

Stimulated emission deletion (STED) nanoscopy is a super-resolution technique based on the confocal microscope – thus one of the coordinate-targeted approaches.[15] Operating principle of STED nanoscopy is very similar to the RESOLFT nanoscopy, which is already described in previous chapter, but the singlet ground state act as the non-fluorescent state in STED nanoscopy. It reduces the effective excitation volume by applying additional, doughnut-shaped depletion laser that induces the stimulated emission process before the fluorophore spontaneously fluoresce.[16] Since the photophysical processes used in STED nanoscopy occur in the < ns timescale, it has a great merit on the imaging rate that can be achieved to the same rate of confocal microscope – more than video rate.[17] The wavelength of depletion laser is optimized to the edge of the emission spectrum for efficient collection of the fluorescence and for preventing the absorption by depletion laser. Unfortunately, the cross section for the stimulated emission at this wavelength is generally small, thus relatively higher power of depletion laser (> 50 mW) is required in STED nanoscopy to reach the sub-diffraction limit resolution. However, since the fluorophore does not absorb the depletion laser, the photoinduced damage to the fluorophore is not considered as too serious.

4.3. Experimental Detail

4.3.1. Sample Preparation

DNA oligomer (30mer) was purchased from *Integrated DNA Technologies* (*IDT*). We selected the random sequence without the possibility of forming secondary structure. Bases at the end of the oligo DNA were amino-modified for the fluorophore labeling. NHS ester form of DY510XL and ATTO647N were used to label DNA sample to match the following terms. First, they have to be excited by

different wavelengths of light. Second, the emission spectrum of a donor should have large overlap with the absorption spectrum of an acceptor. Third, the emission spectrum of a donor has to be extended to near 800 nm so that the fluorescence from two dyes could be depleted by one STED beam. Thus, we selected DY510XL as a donor dye that shows large Stokes shift when it is excited by 510 nm and ATTO647N as an acceptor. DNA and dye were mixed together with the ratio of 1:5:5 in 0.1 M sodium bicarbonate buffer at pH 8.3. After 2 hours of incubation, the mixture solution was purified by HPLC. Fractions were collected and the absorption spectrum was obtained to calculate the concentration of the sample. Finally, sample was stored at 4 °C.

4.3.2. ALFRED Setup

Our ALFRED system is schematically shown in Fig. 4.3. A super-continuum light was generated from the 780 nm output of a Ti:Sapphire laser (<100 fs, 80 MHz, Mai Tai HP, *Spectra-Physics*) by a photonic crystal fiber (FemtoWHITE 800, *NKT Photonics*). An acousto-optic tunable filter (AOTFnC-VIS, *AA Opto-Electronic*) was used to alternate the two excitation beams (635 nm and 510 nm) with the 50 μs alternating time. Possible temporal crosstalk of the two excitation beam was eliminated by adjusting on-time of the AOTF to 46 μs, and 4 μs remained as off-time. 780 nm output of a Ti: Sapphire laser passed through the two glass rods to be stretched to ~5 ps, and were further stretched (~280 ps) by 100 m-long polarization-maintaining single-mode fiber (PMJ-A3HPC, 3S-633-4/125-3-100-1-SP, *OZ Optics*). Gaussian beam-shaped STED beam underwent phase modulation after the phase mask (VPP-1a, *RPC Photonics*) and became doughnut-shaped beam at the focal plane. The three beams were circularly polarized by half- and quarter-wave plates to effectively deplete the fluorescence from randomly-oriented dyes. STED beam was adjusted to irradiate sample after 160 ps from the excitation to achieve the maximum depletion efficiency.

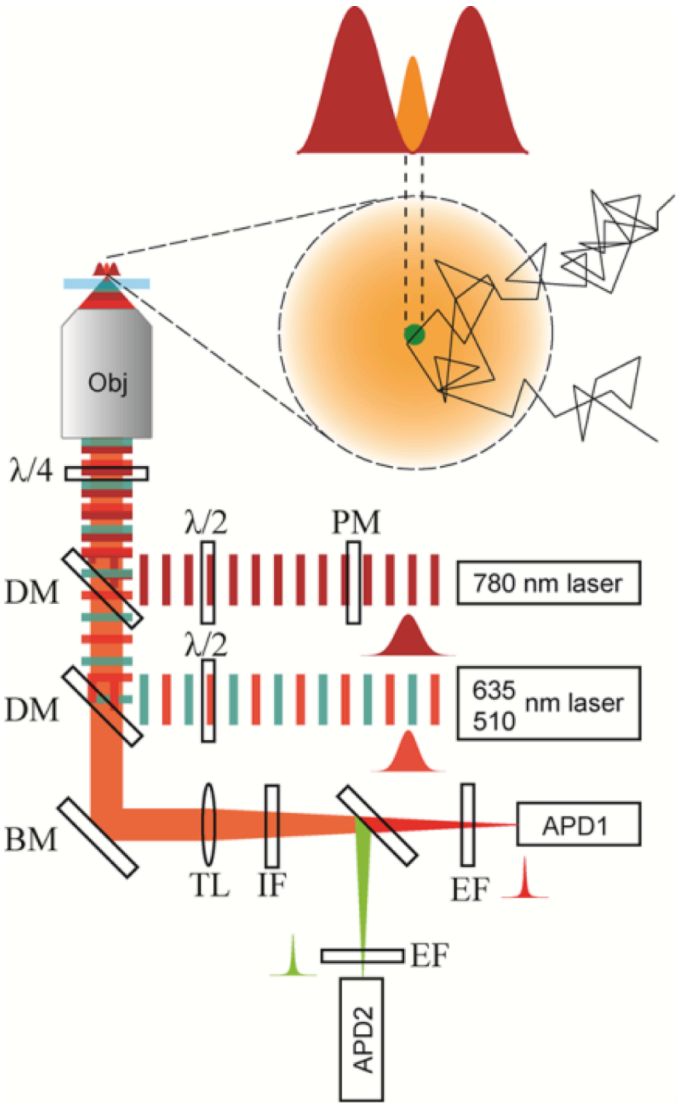

Fig. 4.3 Experimental setup of ALEX-FRET-STED (ALFRED). Two excitation beams (635 nm, 510 nm) irradiate sample alternatingly with 50 μs alternating time. 780 nm STED beam confines the focal volume 50 times smaller than the diffraction-limited confocal volume. Thus, a single-diffusing molecule can be observed in much higher concentration. PM: phase mask, DM: dichroic mirror, BM: broadband mirror, TL: tube lens, IF: IR blocking filter, EF: emission filter.

Co-localization between excitation and STED beam was monitored by collecting scattered light from an Au bead with 80 nm diameter. Fluorescence signal from the sample was collected by an oil immersion type objective (PL APO, 100X, 1.4 NA, *Leica*) through a home-built inverted confocal fluorescence microscope and detected by two perpendicularly lying avalanche photodiode

detectors (SPCM-AQR-14FC, *Perkin Elmer*). Fluorescence from ATTO647N and DY510XL were separated by a dichroic mirror (Z630dcxr, *Chroma*) and further picked out by emission filter (FF01-582-75-25, *Semrock* for DY510XL and ET655LP, *Chroma* for ATTO647N). The intense STED beam was blocked by a short-pass filter (FF01-720/SP-25). FCS data was obtained with the correlator (Flex02-01D, *Correlator.com*), and the raw data was analyzed with LabVIEW program (*National Instruments*).

4.3.3. Data Analysis

Every collected fluorescence signals was saved as the exact time when it arrived. They were modified to the arrays of photon counts per alternating time. With this process, we could classify the detected photons with the excitation wavelengths and emission detector (donor emission and acceptor emission from donor excitation, and those from acceptor excitation). Since we do not calculated the accurate distance between the FRET pair, the direct excitation and emission leakage to other channel were neglected. Background level also checked for the case of excitation only, STED-only and both beams without the sample. We made a histogram of photon counts versus number of event. As a result, background signal was appeared as a large peak at the low photon counts region, and the larger value than the edge was chosen as a background level. With the reconstructed emission arrays, we calculated E and S values for each set of photon bursts. 2D histogram for the distribution of E and S value gave us the information about the conformation and composition.

4.4. Result and Discussion

4.4.1. Reduced Observation Volume by STED Nanoscopy

In order to confirm the reducing effect by additional depletion laser, we measured the effective FWHM of imaged 20-nm fluorescent bead under various depletion powers (Fig. 4.4). Result clearly shows the reducing effect of STED nanoscopy, where the half of radius can be achieved with 25 mW of deletion power. In order to increase the concentration limit up to 100 times, the observation volume should be also reduced 100 times. Thus, we applied ~250 mW of depletion laser, which provides ~30 nm spatial resolution (10 times higher compared to confocal microscopy), to effectively increasing the concentration limit of ALEX-FRET.

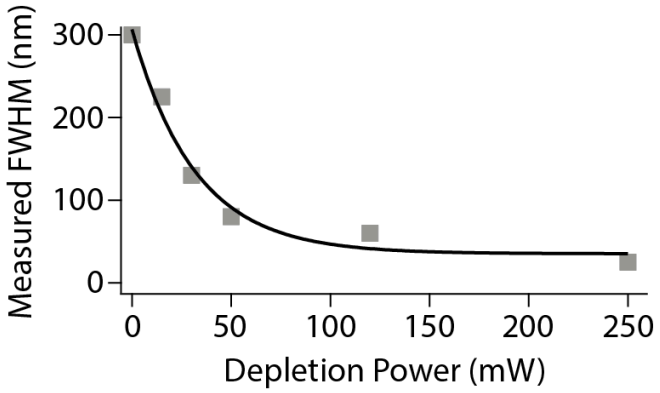

Fig. 4.4 Depletion efficiency in 97 % TED measured under various power condition of depletion laser. The spatial resolution was measured from the full-width at half maximum (FWHM) value of the STED image of 20 nm fluorescent Crimson beads (*Invitrogen*). By fitting the result with a exponential function (Black line), we can get 25 mW of saturation power (*Psat*) at focal plane.

4.4.2. Determination of the Alternating Period and Binning Time

To properly analyze the fluorescence signals at the single molecule level in ALEX-FRET, the alternating period of excitation lasers and the binning time for the individual molecules should be determined to the correct values. For this purpose, we measured the diffusion time of our tested sample, the DY510XL/Atto647N dual labeled single stranded DNA (ssDNA), by FCS in experimental condition (97 % thiodiethanol (TDE) solution, 250 mW of depletion laser) (Fig. 4.5). Since the triplet dynamics appeared the resulting autocorrelation curve, we fitted it with the

equation containing triplet analysis. With 97 % TDE, a viscose solvent having high refractive index, the diffusion time of ssDNA was reduced from 7.5 ms to 3.1 ms when we applied the depletion laser, indicating the reducing effect of observation volume. From this result, we fixed the alternating period and the data binning time as 50 μs and 3 ms, respectively.

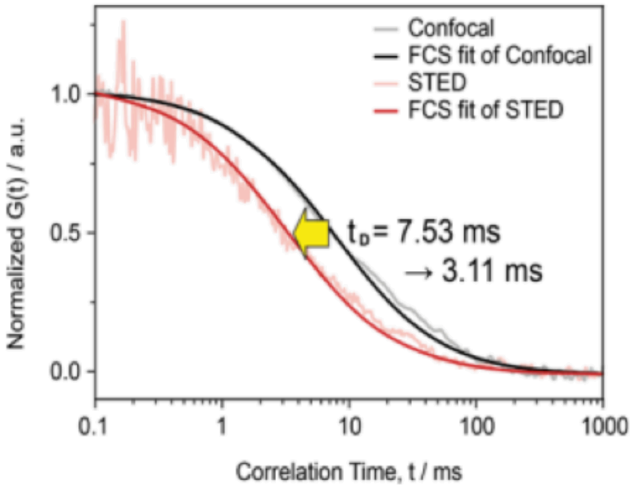

Fig. 4.5 Diffusion time of the dual labeled ssDNA in 97 % TDE under confocal and STED excitations. Raw data and their FCS fit results clearly show the reducing effect of STED nanoscopy.

4.4.3. Observation of Single Bursts from Individual Molecules

For the next step, we confirmed that whether we can observe the individual molecules in the reduced focal volume or not. A simple simulation for the Poisson distribution gives that the reduced observation volume (~0.1 fL) should be occupied by more than two molecules with < 4 % probability, in 5 nM concentration of fluorophore. Thus, we can assure that the observed signals almost came from the single molecules. For the comparison, there exist more than two molecules in the confocal volume (~1 fL) with > 80 % probability (Fig. 4.6).

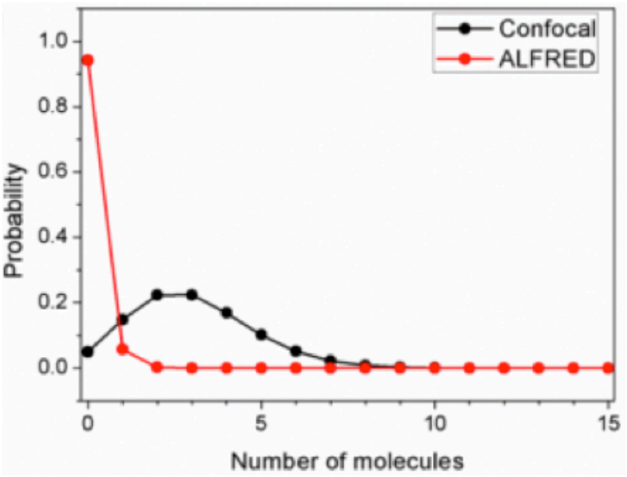

Fig. 4.6 Poisson distribution of the molecules in 5 nM concentration. By reducing the observation volume with depletion laser, we can see the individual molecules at this concentration.

This effect is also clearly represented in the fluorescence time trace with 3 ms binning time (Fig. 4.7). When the depletion laser is turned off, thus there are several molecules in the observation volume, the fluorescence intensity shows an average value with quite large level of fluctuations. On the other hand, when we turned on the depletion laser, the time trace does not show such tendency anymore, but it looks like a bundle of fluorescence 'burst' due to the individual molecules, which is also shown in the confocal ALEX-FRET experiment at low concentration (< 100 pM).

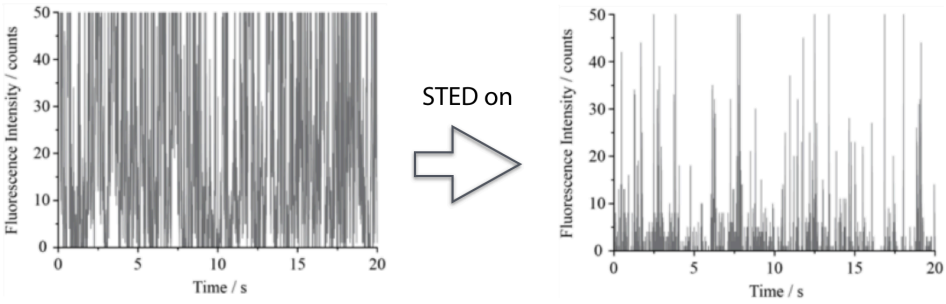

Fig. 4.7 Fluorescence time trace from the observation volume with/without depletion laser. With depletion laser, we can observe the fluorescence 'burst' in the time trace caused from the single molecule.

4.4.4. ALEX-FRET Combined with STED Nanoscopy (ALFRED)

Finally, we demonstrated our concept of ALEX-FRET combined with STED nanoscopy, ALFRED, using the dual labeled ssDNA in 97 % TDE solution. First, We tested the feasibility of our ALFRED system with donor-only and acceptor-only sample (Fig. 4.8). The concentrations were adjusted to 100 pM for confocal ALEX and 1 nM for ALFRED. They showed the coincident results for each other that proved the feasibility of our system.

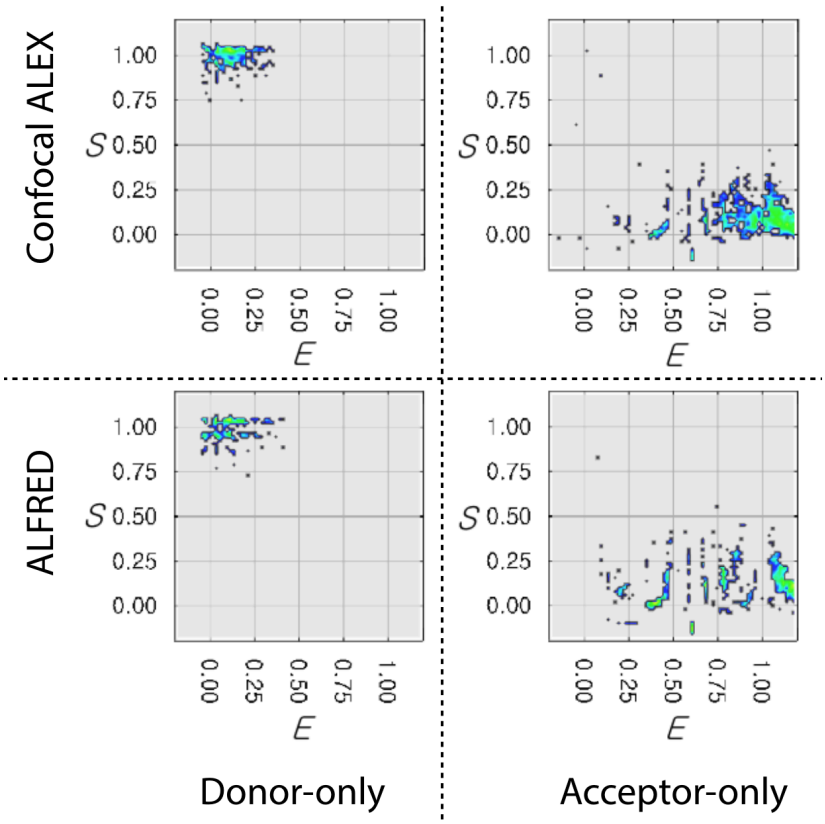

Fig. 4.8 E-S 2D histogram of donor-only and acceptor-only samples in confocal and ALFRED condition. (a,b): 100 pM sample in confocal condition, (c,d): 1 nM sample in ALFRED condition. Donor-only appears near S = 1 and E = 0 whereas acceptor-only appears in the bottom region of the histogram. They are coincident with each other that prove the feasibility of ALFRED experiment.

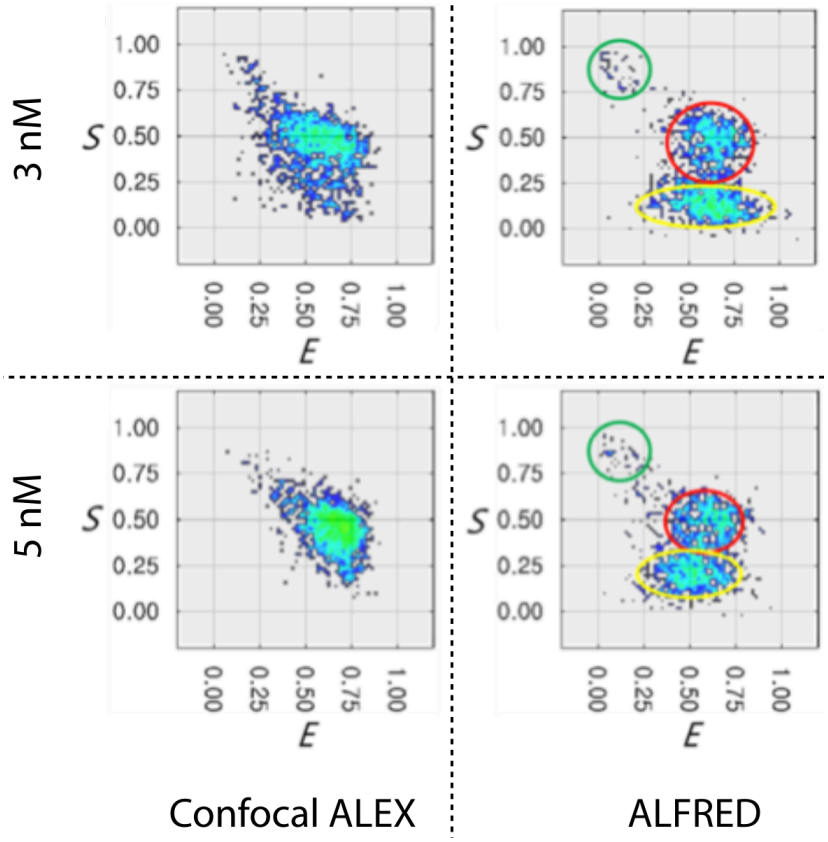

Fig. 4.9 *E-S* 2D histogram of dual labeled ssDNA (30mer). (a) 3 nM of ssDNA in 97 % TDE (left: confocal ALEX, right: ALFRED) and (b) 5 nM of ssDNA in 97 % TDE (left: confocal ALEX, right: ALFRED). In these concentrations, too many molecules exist in confocal volume to give broad, featureless ensemble distribution. However, there is only one diffusing molecule in ALFRED condition due to the confined focal volume. Donor-only (green circle) and accept-only (yellow circle) and dual labeled sample (red circle) can be resolved in ALFRED data.

2D histograms of *E-S* values for 3 nM and 5 nM samples in 97 % TDE were given in Figure 4.9. Binning times were chosen to be 7.5 ms for confocal ALEX and 3.0 ms for ALFRED on the basis of fore-mentioned FCS data. We corrected the background noise, effects of direct excitation and emission leakage to evaluate E and S value. There is notable difference between the distributions of confocal and ALFRED in both 3 nM and 5 nM. Donor-only sample (green circle), acceptor-only sample (yellow circle) and dual labeled sample (red circle) were resolved in ALFRED 2D histograms while there was only one broad, featureless distribution in confocal ALEX 2D histograms due to the ensemble average. As shown in Figure

4.6, there could be up to 10 molecules in confocal volume during observation time, which resulted in the feature like that. In contrast to this, there was no chance that two or more molecules were observed at the same time in ALFRED condition.

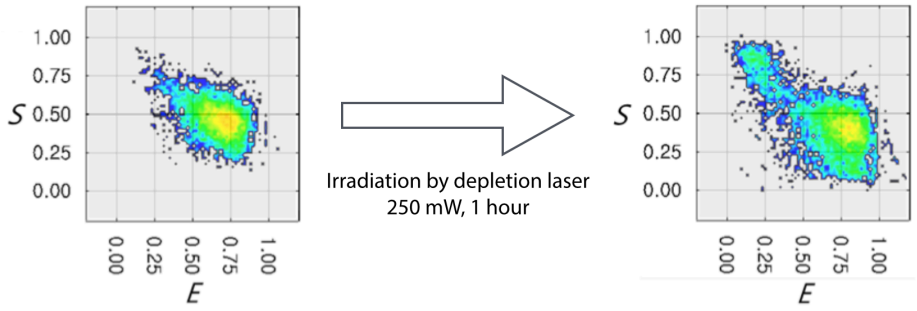

Fig. 4.10 *E-S* 2D histogram of the 5 nM sample in confocal condition. (a): before the irradiation of the STED beam and (b): after the irradiation of the STED beam for an hour. Due to the strong power of the STED beam, one of the dyes can be photobleached during diffusion. As a result, donor-only and acceptor-only distributions appear after 1 hour of the STED beam irradiation.

The appearance of donor-only and acceptor- only distribution is a remarkable point that we purified the mixture of DNA and two dyes by HPLC after the labeling procedure. This can be explained with the photobleaching by depletion laser (Fig. 4.10). In order to test the photobleaching problem by the depletion laser, we performed a series of experiment consisting of 1) acquisition of confocal ALEX (reference), 2) intensive illumination of the depletion laser on the sample for 1 hour and 3) re-acquisition of confocal ALEX (test). As a result, a significant change was observed between the initial reference and the tested sample. Due to the intensive depletion laser, one of the dyes should be easily bleached during diffusing the focused area, leading to the donor- and acceptor- only bursts in the 2D histogram.

The area near $S = 0.5$ and $E = 0.75$ became broad in ALFRED 2D histogram because of its reduced focal volume. This can be interpreted as a combination of two factors. First, STED beam used to reduce the focal volume was strong enough to induce the photobleaching of the fluorophores during diffusion. Some of them could emit fluorescence until they escaped from the focal volume while others could not. Those bleached fluorophores were not able to emit sufficient photons as

values we expected. Also, reduced focal volume limited the observation time resulted in reduction of photon number. In confocal ALEX, small number of variation in photon number did not show much effect on *E* and *S* values. However, that might significantly affect *E* and *S* values when photon counts were relatively small.

4.5. Conclusion

In conclusion, we successfully combined ALEX-FRET single molecule spectroscopy and super-resolution STED nanoscopy to confine the focal volume, much smaller than the diffraction limited confocal volume. With this new technique, we could observe a single diffusing molecule in up to 5 nM concentration, which is 100-times increased concentration than that in conventional confocal ALEX. This concentration is comparable with the dissociation constant of many enzymes. ALFRED in aqueous buffer is not easy in this step because of the fast diffusion of the sample and the low quantum yield of DY510XL in aqueous solution (0.025 in PBS). However, it would be possible if a dye that has high quantum yields in aqueous solution would be developed.

4.6. References

1. E. J. Ambrose, *Nature* **178**, 1194 (1956).
2. M. J. Levene et al., *Science* **299**, 682 (2003).
3. S. R. Leslie et al., *Anal. Chem.* **82**, 6224 (2010).
4. C. Eggeling et al., *Microsc. Res. Techniq.* **70**, 1003 (2007).
5. W. E. Moerner and L. Kador, *Phys. Rev. Lett.* **62**, 2535 (1989).
6. D Haarer and L. Kodir, *Angew. Chem. Int. Ed.* **30**, 540 (1991).

7. A. N. Kapanidis et al., *Proc. Natl. Acad. Sci.* **101**, 8936 (2004).
8. N. K. Lee et al., *Biophys. J.* **88**, 2939 (2005).
9. N. K. Lee et al., *Biophys. J.* **92**, 303 (2007).
10. J. Lee et al., *Angew. Chem. Int. Ed.* **49**, 9922 (2010).
11. N. K. Lee et al., *Chem. Commun.* **46**, 4683 (2010).
12. J. Jung et al., *J. Phys. Chem. B* **116**, 3007 (2012).
13. H. R. Koh et al., *Chem. Commun.* **47**, 10362 (2011).
14. J. Kang et al., *Biophys. Chem.* **195**, 49 (2014).
15. C. Eggeling et al., *Q. Rev. BIophys.* **48**, 178 (2015).
16. S. W. Hell et al., *Opt. Lett.* **19**, 222 (1994).
17. V. Westphal et al., *Science* **320**, 246 (2008).

Abstract in Korean (국문초록)

형광을 이용한 다양한 분석 기술들은 비파괴적 특성으로 인해 생명 현상에 대한 접근을 포함해 넓은 범위의 연구에 응용되고 있다. 특히 형광 현미경은 살아있는 세포의 내부에 존재하는 작은 대상을 분자 수준에서 구별해 관찰할 수 있다는 장점을 지니고 있다. 하지만 회절 한계로 불리는 빛의 특성으로 인해 광학 현미경의 공간 분해능은 관측에 이용하는 빛의 파장의 절반에 해당하는 수준으로 제한되는데 (가시광선의 경우 약 250 nm 로 제한), 이는 생체 내에 존재하는 대부분의 생분자들보다 큰 크기이기 때문에 결과적으로 광학 현미경을 통해 생분자들의 정확한 정보를 얻기는 어렵다. 공초점 현미경을 기반으로 하는 단분자 분광학 기술에서도 회절 한계가 적용되며, 이 경우 관측 영역을 특정 크기 이하로 감소시킬 수 없기 때문에 대상 물질의 농도가 약 100 pM 수준으로 제한된다. 생체 내에 존재하는 물질들은 보통 nM 이상의 농도로 존재하기 때문에 단분자 분광학을 생체 내 물질 연구에 적용하기 위해서는 회절 한계를 극복해야 한다.

최근 20 여년간 회절 한계를 극복하기 위해 초고분해능 현미경법 기술들이 개발되어 왔다. 현존하는 다양한 초고분해능 현미경법 기술들은 세부적으로 각각 독자적인 작용 메커니즘을 지니고 있지만, 넓은 범위에서 형광 분자의 광스위칭 현상을 이용한다는 공통점을 지닌다. 최근에는 기술적인 수준에서 상당한 완성도를 보이며, 그 결과 살아있는 세포 내에 존재하는 여러 종류의 물질들을 20 nm 수준의 3 차원 공간 분해능과 video-rate 이상의 시간 분해능으로 관찰할 수 있는 수준에 이르러 있다. 다만 기술적 복잡성과 이로 인한 높은 금전적 비용이 요구되기 때문에 아직까지는 기존 광학 현미경을 대체할 수 있는 수준까지 응용되지는 못하고 있다. 이에 형광 물질들의 광물리적 특성을 이용해 기존 기술들의 단점을 극복하고 보다 폭넓게 응용할 수 있는 기술을 개발하는 연구를 진행했다.

RESOLFT (reversible saturable optical fluorescence transition) 현미경법은 약한 세기의 빛을 이용해 효과적으로 공간분해능을 향상시킬 수 있는 기술이다. 현재까지 RESOLFT 기술은 형광 단백질에만 적용되어 왔는데, 이는 광스위칭에 의해 유발되는 광표백 현상이 유기 형광 물질에서 두드러지게 나타나기 때문이다. 하지만 유기 형광 물질은 형광 단백질에 비해 더 좋은 영상 대비를 제공하고 더 많은 대상에 표지할 수 있다는 장점을 지니고 있다. 이에 RESOLFT 에 사용되는 다양한 광학적, 화학적 요소들을 최적화 시킴으로써 유기 형광 물질을 도입하고자 했다. 유기 형광 물질인 Cy3 와 Alexa647 을 공유결합으로 연결한 heterodimer 를 연구에 도입했으며, 이를 생체 내에 존재하는 미세소관을 관찰하기 위한 목적으로 표지했다. RESOLFT 기술을 이용해 이를 관찰한 결과 약 100 nm 수준의 공간 분해능을 달성할 수 있었으며, 이를 통해 RESOLFT 기술의 응용 폭을 한층 더 넓힐 수 있는 기반을 마련했다.

또한 형광 물질 중 하나인 형광 나노다이아몬드(fluorescent nanodiamond, FND)의 AND-gate 특성을 이용해 쉽게 회절 한계를 극복할 수 있는 연구를 진행했다. FND 는 다른 파장의 두 빛을 동시에 이용할 경우에만 강한 형광을 방출하는 특징을 지니고 있으며, 이를 이용해 여기에 사용하는 두 빛을 공간적으로 분리시킴으로써 겹친 영역에서만 선택적으로 형광을 얻을 수 있는 기술을 개발했다. 이를 통해 공간 분해능을 약 130 nm 수준으로 향상시킬 수 있었으며, 특히 이는 기술적 복잡성 없이 기존의 공초점 현미경 수준의 기술에서 쉽게 달성할 수 있다는 장점을 지니고 있다. 또한 FND 는 광표백 현상이 없는 차세대 형광 물질로 각광받고 있기 때문에, 지속적인 연구 개발을 통해 대상을 높은 공간 분해능으로 장시간 영상화 할 수 있는 기술로 발전할 수 있다.

확산을 기반으로 하는 단분자 분광학의 농도 제한을 극복하기 위해 STED (stimulated emission depletion) 기술을 기존 단분자 분광학 기술 중 하나인 ALEX-FRET (alternating laser excitation - fluorescence resonance energy transfer) 기술과 결합했다. 도넛 모양의 소광 레이저를 여기 레이저와 결합시킴으로써 관측 영역을 회절 한계 이하로 감소시킬 수 있으며, 감소한 관측 영역에 비례해 측정 농도 한계가

증가한다. 단일 가닥 DNA 를 대상으로 최대 5 nM 농도의 시료를 대상으로 단분자 수준의 형광 측정 및 분석이 가능했으며 이는 기존 농도 한계치를 100 배 이상 증가시킨 결과다. 이를 이용해 살아있는 세포 내에서 생분자들의 구조적 변화 및 결합 반응 등을 단분자 수준에서 분석하는 것이 가능하다.

키워드 : 형광 / 광물리현상 / 형광 물질 / 회절 한계 / 초고분해능 현미경법 / 단분자 분광학

학번 : 2009 – 23842